

LEARNING RICH REPRESENTATIONS FOR STRUCTURED VISUAL PREDICTION TASKS

by

Mohammadreza Mostajabi

A thesis submitted
in partial fulfillment of the requirements for
the degree of

Doctor of Philosophy in Computer Science

at the

TOYOTA TECHNOLOGICAL INSTITUTE AT CHICAGO

June, 2019

Thesis Committee:

Dr. Gregory Shakhnarovich (Thesis advisor),

Dr. Karen Livescu,

Dr. Michael Maire

LEARNING RICH REPRESENTATIONS FOR STRUCTURED VISUAL PREDICTION TASKS

a thesis presented
by

Mohammadreza Mostajabi

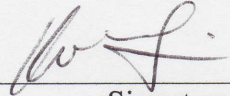
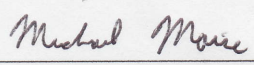
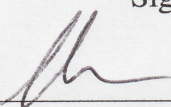
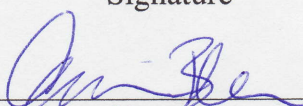
in partial fulfillment of the requirements for the degree of

Doctor of Philosophy in Computer Science.

Toyota Technological Institute at Chicago

June, 2019

– Thesis Committee –

| | | |
|--------------------------------------|--|-----------|
| Dr. Karen Livescu |  | 8/27/2019 |
| Committee member (print/type) | Signature | Date |
| Dr. Michael Maire |  | 8/27/2019 |
| Committee member (print/type) | Signature | Date |
| Dr. Gregory Shakhnarovich |  | 8/27/2019 |
| Thesis/Research Advisor (print/type) | Signature | Date |
| Dr. Avrim Blum |  | 8/27/19 |
| Chief Academic Officer (print/type) | Signature | Date |

LEARNING RICH REPRESENTATIONS FOR STRUCTURED VISUAL PREDICTION TASKS

by

Mohammadreza Mostajabi

Abstract

We describe an approach to learning rich representations for images, that enables simple and effective predictors in a range of vision tasks involving spatially structured maps. Examples of tasks where one can leverage our approach include semantic segmentation and depth estimation. Our key idea is to map small image elements (pixels or superpixels) to feature representations extracted from a sequence of nested regions of increasing spatial extent. These regions are obtained by "zooming out" from the pixel/superpixel all the way to scene-level resolution, and hence we call these zoom-out features. Applied to semantic segmentation and other structured prediction tasks, our approach exploits statistical structure in the image and in the label space without setting up explicit structured prediction mechanisms, and thus avoids complex and expensive inference. Instead image elements are classified by a feedforward multilayer network with skip-layer connections spanning the zoom-out levels.

We describe extensive experiments showing the effectiveness of our simple architecture design. When used in conjunction with modern neural architectures such as ResNet, DenseNet and NASNet (to which it is complementary) our approach achieves competitive accuracy on segmentation benchmarks. In addition, we propose an approach for learning category-level semantic segmentation purely from image-level classification tags indicating presence of categories. It exploits localization cues that emerge from training a modified zoom-out architecture tailored for classification tasks, to drive a weakly supervised process that automatically labels a sparse, diverse training set of points likely to belong to classes of interest. Finally, we introduce data-driven regularization functions for the supervised training of CNNs. Our innovation takes the form of a regularizer derived by learning an autoencoder over the set of annotations. This approach further complements our zoom-out representation, leveraging an improved representation of label space to inform our extraction of features from images.

Thesis Advisor: Gregory Shakhnarovich

Acknowledgments

I would like to thank my research advisor Greg Shakhnarovich. He has been a great supporter during my whole PhD. I had the opportunity to work on what I was interested in and I learned a lot from his deep insight in computer vision and machine learning. I would also like to thank Michael Maire for his research collaboration which was a new chapter in my PhD. I benefited from his novel perspective in the field and productive discussions with him. A big thanks to Karen Livescu for the insightful discussions that we had and her precise and constructive comments on my thesis.

I would also thank the faculty and staff at TTIC for making TTIC a remarkable research institute. I would like to especially thank David McAllester, Madhur Tulsiani, Matthew Walter, Julia Chuzhoy, Chrissy Novak, Adam Bohlander and Mary Marre.

My special thanks goes to my collaborators and fellow students at Toyota Technological Institute at Chicago and University of Chicago, for the fruitful discussions, their supports and all the enjoyable moments we had together. I'd like to especially thank Steven Basart, Igor Vasiljevic, Qingming Tang, Nicholas Kolkin, Lifu Tu, Hai Wang, Somaye Hashemifar, Sudarshan Babu, Ankita Pasad, Shane Settle, Andrea Daniele, Behnam Tavakoli, Shubhendu Trivedi, Haris Angelidakis, Mrinalkanti Ghosh, Takeshi Onishi, Payman Yadollahpour, Ruotian Luo, Falcon Dai and Mantas Mazeika.

My deepest gratitude goes to my family for their endless love and support during all these years. I'd like to thank my parents for supporting my decisions throughout all these years. I owe my success to them. I'd like to thank Elahe for her warm support. Words cannot express how grateful I am to have you by my side.

Contents

| | | |
|----------|---|-----------|
| 1 | Introduction | 13 |
| 1.1 | Contributions | 15 |
| 1.2 | Thesis outline | 16 |
| 2 | Preliminaries | 19 |
| 2.1 | Segmentation | 19 |
| 3 | Zoom-out Features | 28 |
| 3.1 | Introduction | 28 |
| 3.2 | Related work | 31 |
| 3.3 | Zoom-out feature fusion | 33 |
| 3.4 | Experiments | 39 |
| 3.5 | Zoom-out with modern deep CNNs | 50 |
| 3.6 | Summary | 57 |
| 4 | Diverse Sampling for Weakly Supervised Learning of Semantic Segmentation | 60 |
| 4.1 | Introduction | 60 |
| 4.2 | Background | 62 |
| 4.3 | Automatic point-wise supervision for segmentation | 64 |
| 4.4 | Experiments | 69 |

| | | |
|----------|---|------------|
| 4.5 | Summary | 74 |
| 5 | Label Embedding | 79 |
| 5.1 | Introduction | 79 |
| 5.2 | Related work | 82 |
| 5.3 | Method | 85 |
| 5.4 | Experiments | 90 |
| 5.5 | Monocular depth and semantic segmentation | 98 |
| 5.6 | Summary | 105 |
| 6 | Conclusion | 106 |

List of Figures

| | | |
|-----|--|----|
| 2.1 | An example image from BSDS dataset with its segmentation annotations provided by 3 different annotators. | 20 |
| 2.2 | SLIC segmentation results with different values for number of superpixels k and compactness factor m . Higher values of m produce superpixels that align less with image contours and more with spatial grid. | 23 |
| 3.1 | Schematic description of our approach. Features are extracted from a nested sequence of “zoom-out” regions around the superpixel at hand (red). Here we show four out of thirteen levels: 1 (cyan), 6 (olive), 10 (purple) and 13 (blue), as well as the window level (orange) and scene level (green). The features computed at all levels are concatenated and fed to a multi-layer perceptron that classifies the superpixel. | 29 |
| 3.2 | Examples of zoom-out regions. We show four out of fifteen levels: 1(cyan, nearly matching the superpixel boundaries), 6 (olive), 10 (purple) and 13 (blue). 33 | 33 |
| 3.3 | Showing three superpixels in each image (top), followed by corresponding zoom-out regions that are seen by the segmentation process, (left) superpixel, (center) proximal region, (right) distant. As we zoom in from image to the superpixel level, it becomes increasingly hard to tell what we are looking at; however, the higher zoom-out levels provide rich contextual information. . . | 34 |
| 3.4 | Illustration of zoom-out feature extraction procedure for a simple network with three convolutional and two pooling layers. | 38 |
| 3.5 | Color code for VOC categories. Background is black. | 46 |
| 3.6 | Examples illustrating the effect of zoom-out levels. From left: original image, ground truth, levels G1:3, G1:5, G1:5+S1, and the full set of zoom-out features G1:5+S1+S2. In all cases a linear model is used to label superpixels. See Figure 3.5 for category color code, and Table 3.1 for level notation. . . | 46 |

| | | |
|------|--|----|
| 3.7 | Example segmentations on VOC 2012 val with 3-layer neural network used to classify full zoom-out representation of superpixels (15 zoom-out levels). See Figure 3.5 for category color code. | 49 |
| 3.8 | Illustration of zoom-out DenseNet with three dense blocks. | 51 |
| 3.9 | Illustration of zoom-out ResNet with three ResNet blocks. Dashed lines denote spatial size reduction of feature maps by the factor of two. | 52 |
| 3.10 | Example segmentations on VOC 2012 test set with our zoom-out NASNet-A. | 55 |
| 3.11 | Visualization results of zoom-out dilated ResNet-101 on Cityscapes validation set. Left images are our semantic segmentation predicitions overlay on RGB images. Right images are ground truth segmenations. | 59 |
| 4.1 | Our diverse sampling procedure. Left: input image, labeled as containing class <code>dog</code> . Middle: first four steps of diverse sampling procedure for <code>dog</code> , starting with the map $S(\cdot, \text{dog})$. Right: sample of 20 diverse points. | 66 |
| 4.2 | Example segmentations on extra classes from MS-COCO dataset added to the segmentation model trained on VOC dataset. | 76 |
| 4.3 | Examples of diverse sampling outputs. For each foreground class, we show the localization score map from global softmax model, and the selected 20 points. For background, the map shows the max over dot products with any selected foreground points. | 77 |
| 4.4 | Examples of segmentations learned through our weakly supervised approach. From left: input image, ground truth, thresholded localization score maps, segmentation learned with diverse $k = 20$ sampling, CRF post-processing. | 78 |
| 5.1 | Exploiting label structure when training semantic segmentation. Top: An initial phase looks only at the ground-truth annotation of training examples, ignoring the actual images. We learn an autoencoder that approximates an identity function over segmentation label maps. It is constrained to compress and reconstitute labels by passing them through a bottleneck connecting an encoder (red) and decoder (blue). Bottom: The second phase trains a standard CNN for semantic segmentation using zoom-out features for per-pixel output. However, we attach an auxiliary branch (and loss) that also predicts segmentation by passing through the decoder learned in the first phase. After training, we discard this decoder branch, making the architecture appear standard. | 80 |

| | | |
|-----|--|-----|
| 5.2 | Informative structure in annotation. The shape of labeled semantic regions hints at unlabeled parts (black arrows). Object co-occurrence provides a prior on scene composition. | 84 |
| 5.3 | DenseNet architectural specifications. | 86 |
| 5.4 | Alternative regularization scheme. Instead of predicting a representation to pass through the decoder, as in Figure 5.1, we can train with an auxiliary regression problem. We place a loss on directly predicting activations produced by the hidden layers of the encoder. | 87 |
| 5.5 | Auxiliary loss weighting. We plot validation performance as a function of the relative weight of the losses on the auxiliary vs primary output branches when training with the setup in Figure 5.1. Performance is mIoU on PASCAL, without ImageNet pretraining or data augmentation. Note that any nonzero weight on the auxiliary loss (any regularization) improves over the baseline. | 92 |
| 5.6 | Semantic segmentation results on PASCAL. We show the output of a baseline 67-layer zoom-out DenseNet (rightmost column) compared to that of the same architecture trained with our auxiliary decoder branch as a regularizer (middle columns). All examples are from the validation set. While we can discard the auxiliary branch after training, we include its output here to display the decoder’s operation. Our network provides high-level signals to the decoder which, in turn, produces reasonable segmentations. To best illustrate the effect of regularization, all results shown are for networks trained from scratch, without ImageNet pretraining or data augmentation. This corresponds to the 40.5 to 45.2 jump in mIoU reported in Table 5.1, between the baseline and our primary output. | 93 |
| 5.7 | Finding regions with similar representations. For each query image (green border) and region (green rectangle), the next two images to the right are those in the validation set containing the nearest regions to the query region. All query images are from the training set. For examples on red background, search is conducted not by looking at images, but via matching features produced by the encoder run on ground-truth label maps. The bottom-right shows failure cases, such as matching a cat’s arm to the car rear door. For examples on gray background, our DenseNet-67 zoom-out CNN is used to predict the label space search representations from images. | 97 |
| 5.8 | Left image shows semantic segmentation map and the right image is its coressponding depth map. Chairs that are occluded by table are farther from camera than the table. Also relative size of the chairs hints at their distance from the camera. | 100 |

5.9 Depth predictions results on NYUv2. We show not only it is possible to predict depth maps from segmentation maps, but also these predicted depth maps are considerably sharper and more accurate than the predictions from RGB images. 101

List of Tables

| | | |
|------|--|----|
| 3.1 | Statistics of the zoom-out features induced by the 16 layer CNN. Dim: dimension of feature vector. Unit RF size is size of receptive field of a CNN unit in pixels of 256×256 input image. Region size: average size of receptive field of the zoom-out feature in pixels of original VOC images. The group designation is referred to by design of experiments in Section 3.4.3. | 44 |
| 3.2 | comparison of setting the number and scope of zoom-out levels manually versus CNN-based zoom-out. | 44 |
| 3.3 | Effect of replacing SLIC superpixels with an equal number of rectangular regions. Results on VOC 2012 val, mean class IoU. | 45 |
| 3.4 | Ablation study: importance of features from different levels under linear superpixel classification. Results on VOC 2012 val, mean class IoU. . . . | 46 |
| 3.5 | Results on VOC 2010, 2011 and 2012 test. Mean IoU is shown, see Table 3.6 for per-class accuracies of the zoom-out method. | 47 |
| 3.6 | Detailed results of our method on VOC 2012 test. | 48 |
| 3.7 | Results on Stanford Background Dataset | 50 |
| 3.8 | VOC12 validation mIoU of zoom-out with DenseNet and NASNet backbones. | 53 |
| 3.9 | VOC12 validation mIoU of zoom-out with dilated ResNet backbones. . . . | 54 |
| 3.10 | Semantic segmentation results on VOC 2012 test. See Table 3.11 for per-class accuracies of the zoom-out method. | 56 |
| 3.11 | Detailed results of our method on VOC 2012 test. | 56 |
| 3.12 | Semantic segmentation results on Cityscapes validation set. | 57 |
| 4.1 | Comparison of localization models on VOC 2012 validation set | 71 |

| | | |
|-----|--|-----|
| 4.2 | mIoU on VOC 2012 validations set as a function of k points in diverse sampling, with global softmax model | 72 |
| 4.3 | Comparison of point sampling strategies | 72 |
| 4.4 | Comparison of competitive segmentation methods, supervised with image-level tags. For reference, top of the table includes methods trained with stronger supervision on VOC 2012 data, or on additional data. | 73 |
| 5.1 | PASCAL mIoU without ImageNet pretraining. In each experimental setting (choice of architecture, and presence or absence of data augmentation), training with any of our regularizers improves performance over the baseline (shown in gray). | 91 |
| 5.2 | Ablation study. PASCAL mIoU deteriorates if the decoder parameters are not held fixed while training the main CNN. | 94 |
| 5.3 | PASCAL mIoU with ImageNet pretraining. | 94 |
| 5.4 | PASCAL mIoU with COCO pretraining. | 94 |
| 5.5 | Depth prediction results of models with different inputs on NYUv2 test set. | 100 |
| 5.6 | Depth and semantic segmentation results of baseline and our two-part models based on zoom-out DenseNet-121 on NYUv2 test set. | 105 |

Chapter 1

Introduction

Structured prediction in which ground-truth labels themselves exhibit complex internal structure encompasses many of the most important tasks in computer vision. Semantic image segmentation and depth estimation are excellent examples of such tasks. Semantic image segmentation is of particular interest because it requires modeling everything from low-level local patterns such as texture features to complex interactions between neighboring and distant image elements. It is important because it entails aspects of scene understanding such as image classification and object localization. Furthermore, it has important applications ranging from medical image diagnosis to guiding robots' interaction with the world.

Learning rich data representations is an essential block of modern computer vision. In this thesis, we focus on techniques for learning rich representations for structured prediction tasks. In the following it will be described what we mean by rich representations in the context of semantic segmentation and depth estimation. Consider semantic segmentation in which the goal is to label every pixel in the image with a category label. There are many types of information and clues that can be leveraged. Local features play important roles in segmenting and recognizing fine details and object parts. As an example, the texture of a wheel's spoke is

a rich local feature which can be used to segment and recognize a bicycle wheel. However, in many cases, objects are highly occluded and only small parts of the objects are visible. As such, exploiting only local features will not be sufficient to correctly identify partially visible objects. In these cases, one can exploit semantic relations and contextual information such as object co-occurrence as a prior on scene composition. A rich representation for this task is able to encode both local level features and high level contextual information.

Depth estimation is another challenging structured prediction task. The goal in monocular depth estimation is to predict the depth value of each pixel, given a single RGB image as input. Consider an image of an outdoor scene containing grass. The texture of grass becomes less and less apparent as we go farther into the distance. As in semantic segmentation, local texture features are informative. Object occlusion is another source of information. A table is closer to the camera than a chair if the table occludes the chair. Again, a rich representation for monocular depth estimation is a representation which is able to encode both local level features and high level scene information such as object occlusion.

In natural images, each image element has some connection to other image elements. As an example, consider a pixel that is part of an image of the human body. It is very likely that neighboring pixels are part of the same body due to the continuity of real world objects. Objects also have semantic co-occurrence relationships. Observing the ocean supports the existence of a boat rather than a car, while observing roads supports the opposite. Despite the attention semantic segmentation has received, it remains challenging, largely due to complex interactions between local, neighboring and distant image elements and the importance of global context. In order to capture existing structure and contextual information in natural scenes, a common approach has been to use a random field or structured support vector machine [1, 2, 3]. Such models incorporate local evidence in unary potentials, while interactions between label assignments are captured by pairwise and possibly higher-order potentials. This

includes various hierarchical CRFs [2, 4, 5, 6]. These approaches introduce their own severe challenges, among them the intractable nature of inference and learning in many “interesting” models [3].

Conventional models prior to this thesis used hand-crafted features as image descriptors and forced explicit constraints on label structure [7, 5, 8, 9]. In this dissertation our goal is to depart from conventional models and focus on modeling label structure and learning rich representations for structured prediction tasks in an end-to-end fashion.

1.1 Contributions

Our main contributions are summarized as:

- *Learning rich representations with a simple architecture.* Using our zoom-out architecture we learn rich representations at different scales, unlike previous state-of-the-art methods which were based on hand-crafted features. Zoom-out exploits statistical and contextual structure in the label space and dependencies between image elements at different scales, without explicitly encoding them in a complex model. This results in a much simpler and faster model at inference time. This is achieved by extracting and learning features at different levels and scales which gives zoom-out architecture an ability to encode local level features as well as high level contextual information. This is a necessity for most of the structured prediction tasks.
- *Powerful deep CNN-based architecture for semantic segmentation.* We are the first ones to show that segmentation, just like image classification, detection and other recognition tasks, can benefit from the advent of deep convolutional networks.
- *An end-to-end framework for structured visual prediction tasks.* In Chapter 3 we show the

application of the zoom-out architecture for image segmentation. In Section 3.6 we address some of the follow-up work that utilized zoom-out in different applications. In Chapter 5 we apply zoom-out to depth estimation.

- *Diverse sampling for weakly supervised segmentation.* Our diverse sampling method for providing point-wise semantic segmentation supervision from image-level classification tags has almost no hyperparameters and significantly improves results over picking random, dense or top k points with highest scores.
- *Constructing and learning custom regularization functions.* We propose a two-phase training procedure for regularizing deep networks by modeling and predicting label structure. Our experiments, in the context of semantic segmentation demonstrate that our regularization strategy leads to consistent accuracy boosts over baselines, both when training from scratch, or in combination with ImageNet pretraining.
- *Unified architecture for predicting segmentation and depth.* We show that it is possible to predict depth directly from semantic segmentation maps. Based on this observation we propose a two-part architecture for joint prediction of depth and semantic segmentation which uses semantic segmentation as an intermediate representation for depth estimation.

1.2 Thesis outline

In Chapter 3, we introduce a purely feed-forward architecture for semantic segmentation. We map pixels/superpixels to rich feature representations extracted from a sequence of nested regions of increasing extent. These regions are obtained by "zooming out" from the pixel/superpixel all the way to scene-level resolution. This approach exploits statistical

structure in the image and label space without requiring explicit structured prediction mechanisms, thus avoiding complex and expensive inference. Instead image elements are classified by a feedforward multilayer network. We show that our rich image representation with a simple linear classifier on top, significantly outperforms models based on state-of-the-art hand designed features processed by complex CRF models.

Most recent progress in semantic segmentation can be attributed to advances in deep learning and to availability of large, manually labeled datasets. However, the cost and complexity of annotating segmentation labels are significantly higher than that for classification. There is mounting evidence that this task, while difficult, is not hopeless. Units sensitive to object localization have been shown to emerge as part of the representations learned by convolutional neural networks (CNNs) trained for image classification. In Chapter 4 we propose an approach for learning category-level semantic segmentation purely from image-level classification tags indicating presence of categories. In the first chapter we proposed zoom-out architecture to extract rich pixel-level features for the task of semantic segmentation. We can tailor zoom-out architecture for the task of image classification by performing global pooling on top of zoom-out features. This allows us to exploit localization cues that emerge from training classification-task convolutional networks, to drive a weakly supervised process that automatically labels a sparse, diverse training set of points likely to belong to classes of interest. Our approach has almost no hyperparameters, is modular and obtains competitive results on the VOC 2012 segmentation benchmark [10].

In computer vision, annotation is a sufficiently precious resource that it is commonplace to pretrain systems on millions of labeled ImageNet [11] examples. These systems absorb a useful generic visual representation ability during pretraining, before being fine-tuned to perform more specific tasks using fewer labeled examples. Current state-of-the-art semantic segmentation methods [12, 13, 14] follow such a strategy. Its necessity is driven by the high

relative cost of annotating ground truth for spatially detailed segmentations [15, 16], and the accuracy gains achievable by combining different data sources and label modalities during training. A collection of many images, coarsely annotated with a single label per image (ImageNet [11]), is still quite informative in comparison to a smaller collection with detailed per-pixel label maps for each image (PASCAL [15] or COCO [16]). In Chapter 5 we show that detailed ground truth annotation of this latter form contains additional information that existing schemes for training deep convolutional neural networks (CNNs) fail to exploit. By designing a new training procedure, we are able to capture some of this information, and as a result increase accuracy at test time [17].

Chapter 2

Preliminaries

We present definitions and methods used in later chapters of this dissertation.

2.1 Segmentation

Segmentation refers to task of partitioning all or some part of the pixels in an image into coherent regions, where pixels in each region share similar attributes. A coherent region can be considered as a region in which pixels belong to it share similar feature statistics such as similar colors or texture patterns. Here we categorize segmentation methods into two main categories of semantic and class agnostic. There is also instance segmentation where the goal is to identify all instances of the segmented objects in an image. However, we are not going to address instance segmentation in this thesis.

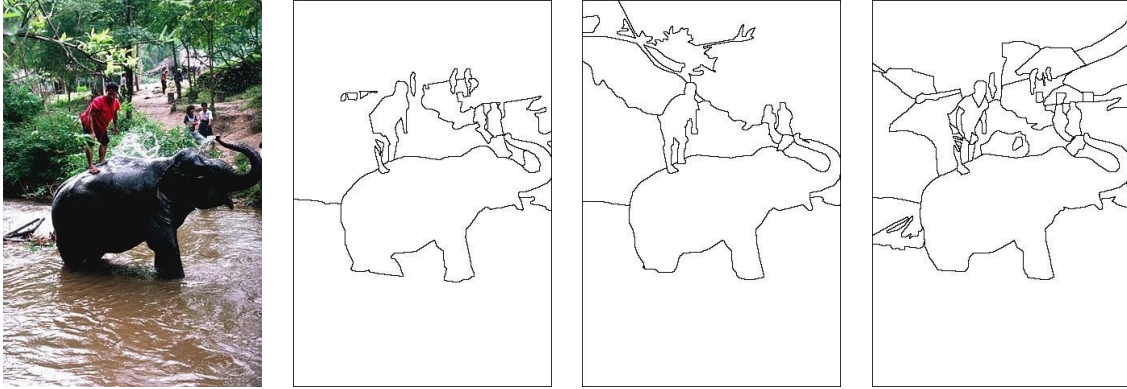


Figure 2.1: An example image from BSDS dataset with its segmentation annotations provided by 3 different annotators.

2.1.1 Class agnostic segmentation

In class agnostic segmentation, all or some of the pixels in the image will be partitioned into coherent regions, but unlike semantic segmentation we won't assign a class label to these regions. Class agnostic segmentation methods can be supervised or unsupervised. An example of rich dataset that can be used for supervised class agnostic segmentation is BSDS [18, 19]. It contains segmentation annotations by 3 different annotators for natural images. Figure 2.1 shows an example image with its segmentation annotations.

Large part of class agnostic segmentation literature addresses unsupervised learning of segmentation. Unsupervised segmentation methods can be applied to wide variety of images without requiring manually-labeled datasets and yet partition pixels to coherent regions. Since no ground truth annotations are provided, coherency is usually defined by distance between features of pixels within the same segment.

Regardless of being supervised or unsupervised, part of class agnostic segmentation literature is focused on oversegmentation. Oversegmentation of an image produces regions which is called superpixels. Superpixel methods can be based on low-level features such as color, intensity and texture statistics [20, 21, 22, 23] or complex learned features of deep CNNs [24,

25]. One of the benefit of using superpixel representation is reducing computational cost in many interesting segmentation methods. Semantic segmentation is viewed as structured prediction task and hence it is common to use a random field or structured support vector machine. Using superpixels will reduce the number of variables from order of millions (i.e. number of pixels) to order of hundreds which in turn significantly reduces computational cost of semantic segmentation methods.

One of the benefits of using a superpixel representation of an image over a pixel representation is that superpixels provide a rich spatial neighborhood around each pixel which respects contours. This neighborhood can be used to compute local features, rather than extracting local features from individual pixels or a random neighborhood around each pixel which may not respect image contours or objects boundaries. In Chapter 3 we show the effectiveness of implicitly encoding long and short range dependencies between image elements by extracting features from different spatial levels area around each superpixel. Hence, class agnostic segmentation can be viewed as a useful preprocessing step for downstream tasks such as semantic segmentation. In Chapter 3 we show that the segments that are produced by unsupervised segmentation methods can be subsumed by our semantic segmentation method to assign class labels to superpixels. In the following we explain how SLIC [20], an unsupervised segmentation method for producing superpixels works. We will use SLIC in Chapter 3.

2.1.1.1 SLIC

Simple linear iterative clustering (SLIC) is a class agnostic segmentation method that produces regular and compact superpixels. With a tuned set of parameters SLIC superpixels respect contours and objects' boundaries. If we consider N to be number of pixels in an image then the running time of SLIC is $\mathcal{O}(N)$. Having linear running time and producing high quality compact superpixels, makes SLIC one of the fastest superpixel algorithms to be used as a

preprocessing step in variety of downstream tasks, such as semantic segmentation and depth estimation.

SLIC clusters pixels based on color features and spatial proximity. The color spaced that is used in SLIC is CIELAB. In CIELAB color space, colors are defined by lab values which has a nice property that the amount of visually perceived changes in color and brightness corresponds to similar changes in lab values. SLIC performs clustering on five-dimensional $[labxy]$ space in which xy is the pixel coordinate. SLIC takes 2 parameters as input. The main parameter is k , the desired number of superpixels. Once k is defined approximate size of each superpixel in an image with N pixels will be $\frac{N}{K}$ pixels. This leads to a superpixel roughly centered at every grid interval $S = \sqrt{\frac{N}{K}}$.

The distance between each pixel to the center of a superpixel is based on two features: CIELAB color values and spatial coordinates. Spatial distance is normalized in SLIC, since directly using xy coordinates makes SLIC sensitive to the size of the image. In Equation 2.1.1 m is an input parameter to SLIC which controls relative weight of spatial distance with respect to color distance. Larger values of m leads to more compact superpixels.

$$\begin{aligned}
 d_{lab} &= \sqrt{(l_k - l_i)^2 + (a_k - a_i)^2 + (b_k - b_i)^2} \\
 d_{xy} &= \sqrt{(x_k - x_i)^2 + (y_k - y_i)^2} \\
 D_s &= d_{lab} + \frac{m}{S} d_{xy}
 \end{aligned} \tag{2.1.1}$$

Initially, superpixel centers are placed along a regular spatial grid at interval S . The superpixel centers are associated with 5-dimensional vectors of color and coordinate features. These superpixel centers are moved to a position that has the lowest image gradient within a 3×3 neighborhood. This step prevents initial seeds from being placed at an edge or a noisy pixel.



(a) $k = 75, m = 15$



(b) $k = 75, m = 75$



(c) $k = 500, m = 15$



(d) $k = 500, m = 75$

Figure 2.2: SLIC segmentation results with different values for number of superpixels k and compactness factor m . Higher values of m produce superpixels that align less with image contours and more with spatial grid.

Next, each pixel in the image will be assigned to a closest superpixel center whose search area overlaps this pixel. The search area for each superpixel is $2S \times 2S$ area around the superpixel center on the xy plane. Limiting the search space to $2S \times 2S$ area around each superpixel center makes SLIC one of the fastest superpixel algorithms. Once all pixels are associated with their nearest superpixel centers, then new superpixel centers will be computed as the average of 5-dimensional vectors of pixels belonging to them. This process will be iteratively repeated till convergence. Algorithm 1 summarizes SLIC. Figure 2.2 shows superpixels produced by SLIC with different values for number of superpixels k and compactness factor m .

Algorithm 1 SLIC

- 1: Initialize k cluster centers along a regular spatial grid with grid intervals S .
 - 2: Move cluster center's to a position that has the lowest gradient within a 3×3 neighborhood.
 - 3: Residual error $E \leftarrow \infty$.
 - 4: Pixel distance $d(p) \leftarrow \infty$ for each pixel p .
 - 5: **while** $E \geq threshold$ **do**
 - 6: **for** each cluster center c_i **do**
 - 7: **for** each pixel p within $2S \times 2S$ square neighborhood of c_i **do**
 - 8: compute the distance D (Eq. 2.1.1) between cluster center c_i and p .
 - 9: **if** distance $D < d(p)$ **then**
 - 10: Assign p to c_i .
 - 11: $d(p) \leftarrow D$.
 - 12: Compute new cluster centers based on pixel assignments
 - 13: Compute residual error E between recomputed cluster centers and previous ones
-

2.1.2 Semantic segmentation

Semantic segmentation is a supervised segmentation in which the goal is to assign a label, from a predefined set of class labels, to each pixel of a given image. In semantic segmentation, ground truth annotations are provided. These annotations serve as a reference of what the segmentation method should produce. In semantic segmentation, the set of object classes

that we want to segment is well defined. Semantic segmentation does not differentiate between multiple instances of the same object class. In instance segmentation the goal is to identify all instances of the segmented objects in an image. However, instance segmentation does not address non-object or stuff classes such as sky. We can be more ambitious and consider panoptic segmentation [26] which unifies semantic segmentation and instance segmentation. In Panoptic segmentation the goal is to assign category level label to every pixel in the given image and also identify object instances as well. This makes it a more difficult task than semantic segmentation or instance segmentation. In this thesis, we focus on semantic segmentation. Conditional random fields (CRFs) have been widely used in semantic segmentation [1, 2, 4, 5, 8, 3]. In the following we give an overview of CRFs and discuss about pairwise CRFs for semantic segmentation.

2.1.2.1 Conditional random fields

Consider each pixel as a random discrete variable X_i . Then $\mathbf{X} = \{X_1, X_2, X_3, \dots, X_N\}$ is a set of random variables corresponding to image pixels in an image I with N pixels. Each variable X_i can take a label $\mathbf{x} \in \{l_1, l_2, l_3, \dots, l_C\}$. $P(X = \mathbf{x})$ is the probability of random variables X taking any labeling \mathbf{x} . Then the posterior distribution $P(X = \mathbf{x}|I)$ over the labellings of the CRF is a Gibbs distribution:

$$P(X = \mathbf{x}|I) = \frac{1}{Z} \exp \left(- \sum_{c \in \mathcal{C}_G} \phi_c(\mathbf{x}_c|I) \right), \quad (2.1.2)$$

where Z is a normalization constant called partition function and $\mathcal{G} = (\mathcal{V}, \mathcal{E})$ is a graph over set of variables X . $\phi_c(\mathbf{x}_c|I)$ is the potential function over the variables in the clique c . The corresponding Gibbs energy will be

$$E(\mathbf{x}) = -\log P(X = \mathbf{x}|I) - \log Z = \sum_{c \in \mathcal{C}_{\mathcal{G}}} \phi_c(\mathbf{x}_c|I). \quad (2.1.3)$$

2.1.2.2 Pairwise CRFs for semantic segmentation

Semantic segmentation is widely treated as a structured prediction task in which labels themselves exhibit internal structure. A common approach is to utilize conditional random fields and frame semantic segmentation as an energy minimization problem over pixel or superpixel labelings. Energy minimization will be done over unary, pairwise and possibly higher-order terms.

In our notations we use $\psi_c(\mathbf{x}_c)$ to denote $\phi_c(\mathbf{x}_c|I)$. The corresponding energy for CRF model with unary and pairwise potentials is

$$E(\mathbf{x}) = \sum_{i \in \mathcal{V}} \psi_i(x_i) + \sum_{(i,j) \in \mathcal{E}} \psi_{ij}(x_i, x_j). \quad (2.1.4)$$

The unary term is usually based on estimated probability of a pixel or superpixel to take on a particular label produced by a classifier. Pairwise terms capture labeling dependencies between pair of variables corresponding to pixels or superpixels. Pairwise terms are often called smoothness terms, because they advocates neighboring pixels receive same labels. Depending on the CRF model, pairwise connections can be limited to neighboring pixels, which results in capturing only short-range dependencies. In dense and fully connected CRFs, pairwise term can capture both short-range and long-range dependencies between pairs of variables. Local evidence is often incorporated in unary terms, while interactions between label assignments are captured by pairwise terms. Krähenbühl et al. [3] introduce one of the most successful and widely-used inference methods for fully connected CRFs. When the graph $\mathcal{G} = (\mathcal{V}, \mathcal{E})$ in Equation 2.1.4 is a complete graph on \mathbf{X} , then the corresponding CRF

model is a fully connected pairwise CRF. The pairwise potential in [3] has the form

$$\psi_{ij}(x_i, x_j) = \mu(x_i, x_j) \sum_{m=1}^K w^{(m)} k^{(m)}(\mathbf{f}_i, \mathbf{f}_j). \quad (2.1.5)$$

In Equation 2.1.5, μ is a smoothness term which encourages nearby similar pixels to have the same label. $w^{(m)}$ are linear combination weights and each $k^{(m)}$ is a Gaussian kernel

$$k^{(m)}(\mathbf{f}_i, \mathbf{f}_j) = \exp\left(-\frac{1}{2}(\mathbf{f}_i - \mathbf{f}_j)^T \Lambda^{(m)}(\mathbf{f}_i - \mathbf{f}_j)\right), \quad (2.1.6)$$

where $\mathbf{f}_i, \mathbf{f}_j$ are feature vectors of pixels i and j . In Chapter 4 we apply fully connected pairwise CRFs to the output of our weakly supervised semantic segmentation model.

Chapter 3

Zoom-out Features

We introduce the zoom-out architecture, a purely feed-forward architecture for semantic segmentation. We map small image elements to rich feature representations extracted from a sequence of nested regions of increasing extent. These regions are obtained by "zooming out" from the pixel/superpixel all the way to scene-level resolution. This approach exploits statistical structure in the image and in the label space without setting up explicit structured prediction mechanisms, and thus avoids complex and expensive inference. In Chapter 4 we will use zoom-out representations to learn category-level semantic segmentation purely from image-level classification tags.

3.1 Introduction

Learning rich representations of data is an essential block of recognition in modern computer vision. Consider one of the central vision tasks, *semantic segmentation*: assigning to each pixel in an image a category-level label. Despite the attention it has received, it remains

challenging, largely due to complex interactions between neighboring as well as distant image elements, the importance of global context, and the interplay between semantic labeling and instance-level detection. A widely accepted conventional wisdom, followed in much of the segmentation literature, is that segmentation should be treated as a structured prediction task, which most often means using a random field or structured support vector machine model of considerable complexity. Refer to Section 2.1.2 for further details.

This in turn brings up severe challenges, among them the intractable nature of inference and learning in many “interesting” models. To alleviate this, many previously proposed methods rely on a pre-processing stage, or a few stages, to produce a manageable number of hypothesized regions, or even complete segmentations, for an image. These are then scored, ranked or combined in a variety of ways.

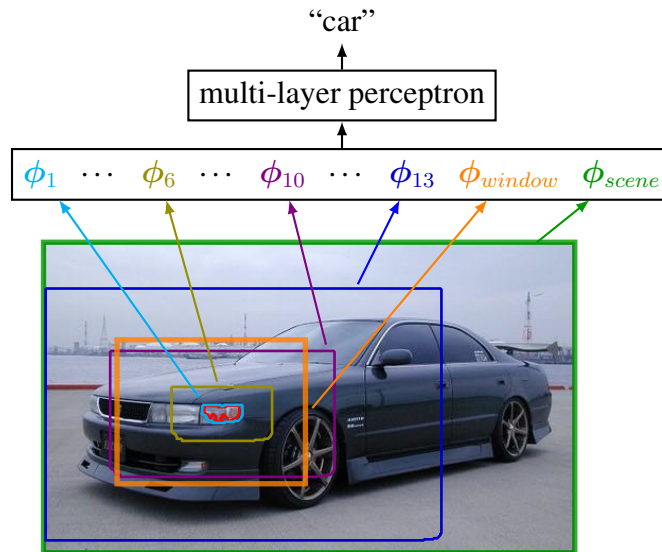


Figure 3.1: Schematic description of our approach. Features are extracted from a nested sequence of “zoom-out” regions around the superpixel at hand (red). Here we show four out of thirteen levels: 1 (cyan), 6 (olive), 10 (purple) and 13 (blue), as well as the window level (orange) and scene level (green). The features computed at all levels are concatenated and fed to a multi-layer perceptron that classifies the superpixel.

Here we consider a departure from these conventions, and approach semantic segmentation as a single-stage classification task, in which each image element (pixel or superpixel) is

labeled by a feedforward model, based on the evidence computed from the image. Surprisingly, in experiments on PASCAL VOC 2012 segmentation benchmark, we show that this simple sounding approach leads to results significantly surpassing previously published ones.

The “secret” behind our method is that the evidence used in the feedforward classification is not computed from a small local region in isolation, but collected from a sequence of levels, obtained by “zooming out” from the close-up view of the superpixel. Starting from the superpixel itself, to a small region surrounding it, to a larger region around it and all the way to the entire image, we compute a rich feature representation at each level and combine all the features before feeding them to a classifier. This allows us to exploit statistical structure in the label space and dependencies between image elements at different resolutions without explicitly encoding these in a complex model.

We do not mean to dismiss structured prediction or inference, and as we discuss in Section 3.6, these tools are complementary to our architecture. In this chapter we explore how far we can go without resorting to explicitly structured models.

We use convolutional neural networks (CNNs) to extract features from larger zoom-out regions. CNNs, (re)introduced to vision in 2012, have facilitated a dramatic advance in classification, detection, fine-grained recognition and other vision tasks. Segmentation has remained conspicuously left out from this wave of progress; while image classification and detection accuracies on VOC has improved by nearly 50% (relative), segmentation numbers has improved only modestly. A big reason for this was that neural networks were inherently geared for “non-structured” classification and regression. In this work we propose a way to leverage the power of representations learned by CNNs, by framing segmentation as classification and making the structured aspect of it implicit. Finally, we show that use of a multi-layer neural network trained with asymmetric loss to classify pixels/superpixels represented by zoom-out features, leads to significant improvement in segmentation accuracy

over simpler models and conventional (symmetric) loss.

Below we give a high-level description of our method, then discuss related work and position our work in its context. Most of the technical details are deferred to Section 3.4, in which we describe implementation and report on results, before concluding in Section 3.6.

3.2 Related work

The literature on segmentation is vast, and here we only mention work that is either significant as having achieved state-of-the-art performance in recent times, or is closely related to ours in some way. In Sections 3.4 and 3.5 we compare our performance to that of most of the methods mentioned here.

Many prominent segmentation methods rely on conditional random fields (CRFs) over nodes corresponding to pixels or superpixels. Such models incorporate local evidence in unary potentials, while interactions between label assignments are captured by pairwise and possibly higher-order potentials. This includes various hierarchical CRFs [2, 4, 5, 8]. In contrast, we let the zoom-out features (in CRF terminology, the unary potentials) capture higher-order structure.

Another recent trend has been to follow a multi-stage approach: First a set of proposal regions is generated, by a category-independent [27, 28] or category-aware [29] mechanism. Then the regions are scored or ranked based on their compatibility with the target classes. Work in this vein includes [30, 31, 29, 32, 33]. A similar approach is taken in [6], where multiple segmentations obtained from [30] are re-ranked using a discriminatively trained model. Recent advances along these lines include [34], which uses CNNs, and [35], which improves upon the re-ranking in [6], also using CNN-based features. In contrast to most of

the work in this group, we do not rely on region generators, and directly operate on pixels or limit preprocessing to over-segmentation of the image into a large number of superpixels.

The idea of using non-local evidence in segmentation, and specifically of computing features over a neighborhood of superpixels, was introduced in [36] and [37]; other early work on using forms of context for segmentation includes [2]. A study in [38] concluded that non-unary terms may be unnecessary when neighborhood and global information is captured by unary terms, but the results were significantly inferior to state of the art at the time.

Recent work closest to ours includes [39, 40, 41, 9, 42]. In [39], the same CNN is applied on different resolutions of the image and combined with a tree-structured graph over superpixels to impose smoothness. In [9] the features applied to multiple levels are also homogeneous, and hand-crafted rather than learned. In [40] there is also a single CNN, but it is applied in a recurrent fashion, i.e., input to the network includes, in addition to the scaled image, the feature maps computed by the network at a previous level. A similar idea is pursued in [42], where it is applied to boundary detection in 3D biological data. In contrast with all of these, we use different feature extractors across levels, some of them with a much smaller receptive field than any of the networks in the literature. We show in Section 4.4 that our approach obtains better performance (on Stanford Background Dataset) than that reported for [39, 40, 41, 9]; no comparison to [42] is available.

Finally, our work shares some ideas with other concurrent efforts. In Fully Convolutional Networks (FCN) [43] the fully connected layers are converted to convolutional layers. Segmentation predictions are produced at different layers in the network and then upsampled and summed to produce final segmentation output. The main difference with Fully Convolutional Networks (FCN) [43] is that we concatenate features, rather than summing predictions up across levels. This allows a multi-layer network on top of zoom-out features to combine them with a learned non-linear function. Hpercolumns [44] is closest to our method where they

concatenate features across different layers of network. However we incorporate a much wider range of zoom-out levels, including scene level features for each superpixel. As a result we achieve a significantly better performance on VOC 2012 test set than either of these methods.

3.3 Zoom-out feature fusion

We cast category-level segmentation of an image as classifying a set of pixels/superpixels. In the case of superpixels, since we expect to apply the same classification machine to every superpixel, we would like the nature of the superpixels to be similar, in particular their size. In our experiments we use SLIC [45], but other methods that produce nearly-uniform grid of superpixels might work similarly well. Figures 3.2 and 3.3 provides a few illustrative examples for this discussion. As it is shown in 3.3 local patches are ambiguous in a sense that it is difficult to tell which objects they belong to. As we zoom out and look at larger regions we can access rich contextual information. In the following we describe different levels of zoom-out features. For the following sections we focus on superpixels. In Section 3.5 we discuss zoom-out descriptors for pixels.

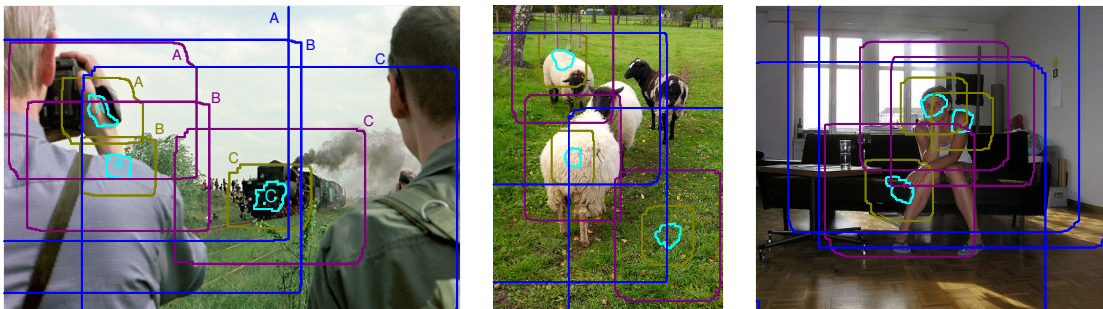


Figure 3.2: Examples of zoom-out regions. We show four out of fifteen levels: 1 (cyan, nearly matching the superpixel boundaries), 6 (olive), 10 (purple) and 13 (blue).

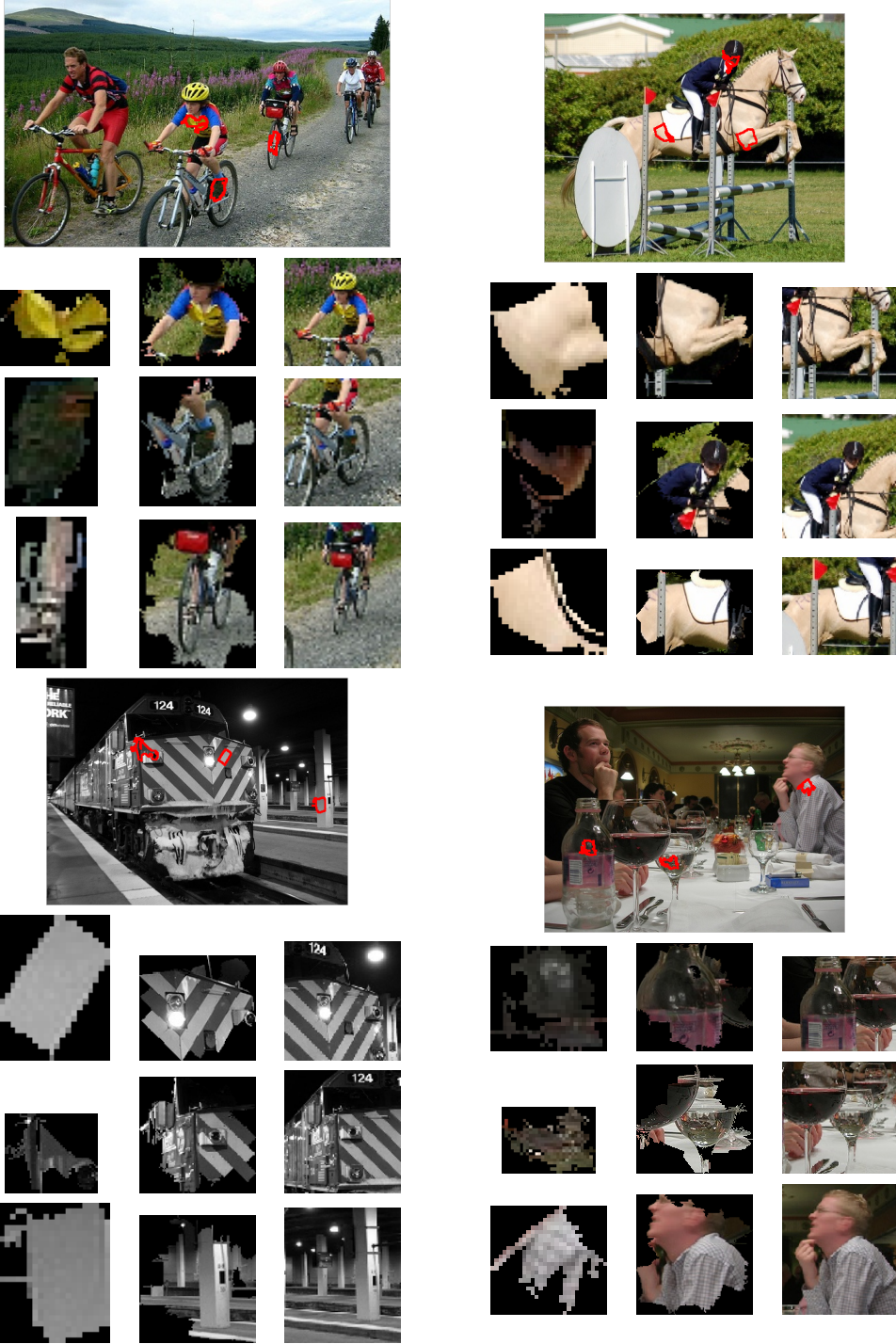


Figure 3.3: Showing three superpixels in each image (top), followed by corresponding zoom-out regions that are seen by the segmentation process, (left) superpixel, (center) proximal region, (right) distant. As we zoom in from image to the superpixel level, it becomes increasingly hard to tell what we are looking at; however, the higher zoom-out levels provide rich contextual information.

3.3.1 Scoping the zoom-out features

The main idea of our zoom-out architecture is to allow features extracted from different levels of spatial context around the superpixel to contribute to the labeling decision at that superpixel. Before going into specifics of how we define the zoom-out levels, we discuss the role we expect different levels to play.

Local The narrowest scope is the superpixel itself. We expect the features extracted here to capture local evidence: color, texture, small intensity/gradient patterns, and other properties computed over a relatively small contiguous set of pixels. The local features may be quite different even for neighboring superpixels, especially if these straddle category or object boundaries.

Proximal As we zoom out and include larger spatial area around the superpixel, we can capture visual cues from surrounding superpixels. Features computed from these levels may capture information not available in the local scope; e.g., for locations at the boundaries of objects they will represent the appearance of both categories. For classes with non-uniform appearance they may better capture characteristic distributions for that class. We can expect somewhat more complex features to be useful at this level, but it is usually still too myopic for confident reasoning about presence of objects.

Two neighboring superpixels could still have quite different features at this level, however some degree of smoothness is likely to arise from the significant overlap between neighbors' proximal regions, e.g., A and B in Fig. 3.2. As another example, consider color features over the body of a leopard; superpixels for individual dark brown spots might appear quite different from their neighbors (yellow fur) but their proximal regions will have pretty similar distributions (mix of yellow and brown). Superpixels that are sufficiently far from each other

could still, of course, have drastically different proximal features, e.g., A and C in Fig. 3.2.

Distant Zooming out further, we move to the distant levels : regions large enough to include sizeable fractions of objects, and sometimes entire objects. At this level our scope is wide enough to allow reasoning about shape, presence of more complex patterns in color and gradient, and the spatial layout of such patterns. Therefore we can expect more complex features that represent these properties to be useful here. Distant regions are more likely to straddle true boundaries in the image, and so this higher-level feature extraction may include a significant area in both the category of the superpixel at hand and nearby categories. For example, consider a person sitting on a chair; bottle on a dining table; pasture animals on the background of grass, etc. Naturally we expect this to provide useful information on both the appearance of a class and its context.

For nearby superpixels and far enough zoom-out level, distant regions will have a very large overlap, which will gradually diminish with distance between superpixels. This is likely to lead to somewhat gradual changes in features, and to impose a system of implicit smoothness “terms”, which depend both on the distance in the image and on the similarity in appearance in and around superpixels. Imposing such smoothness in a CRF usually leads to a very complex, intractable model.

Scene The final zoom-out scope is the entire scene. Features computed at this level capture “what kind of an image” we are looking at. One aspect of this global context is image-level classification: since state of the art in image classification seems to be dramatically higher than that of detection or segmentation [46, 47]. We can expect image-level features to help determine presence of categories in the scene and thus guide the segmentation.

More subtly, features that are useful for classification can be directly useful for global

support of local labeling decisions; e.g., lots of green in an image supports labeling a (non-green) superpixel as cow or sheep more than it supports labeling that superpixel as chair or bottle, other things being equal. Or, lots of straight vertical lines in an image would perhaps suggest man-made environment, thus supporting categories relevant to indoors or urban scenes more than, say, wildlife.

At this global level, all superpixels in an image will of course have the same features, imposing (implicit, soft) global constraints. This is yet another form of high-order interaction that is hard to capture in a CRF framework, despite numerous attempts [8].

3.3.1.1 CNN-based zoom-out

A feature map computed by a convolutional layer with k filters assigns a k -dimensional feature vector to each receptive field of that layer. For most layers, this feature map is of lower resolution than the original image, due to sub-sampling induced by pooling and possibly stride in filtering at previous layers. We upsample the feature map to the original image resolution, if necessary. This produces a k -dimensional feature vector for every *pixel* in the image. Pooling these vectors over a superpixel gives us a k -dimensional feature vector describing that superpixel. Figure 3.4 illustrated this feature computation for a superpixel with a toy network with three convolutional layers, interleaved with two pooling layers (2×2 non-overlapping pooling receptive fields). We can also directly classify pixels rather than superpixels, once we have computed k -dimensional feature vector for every *pixel* in the image. In Section 3.5 we will discuss the results of directly classifying pixels with zoom-out features.

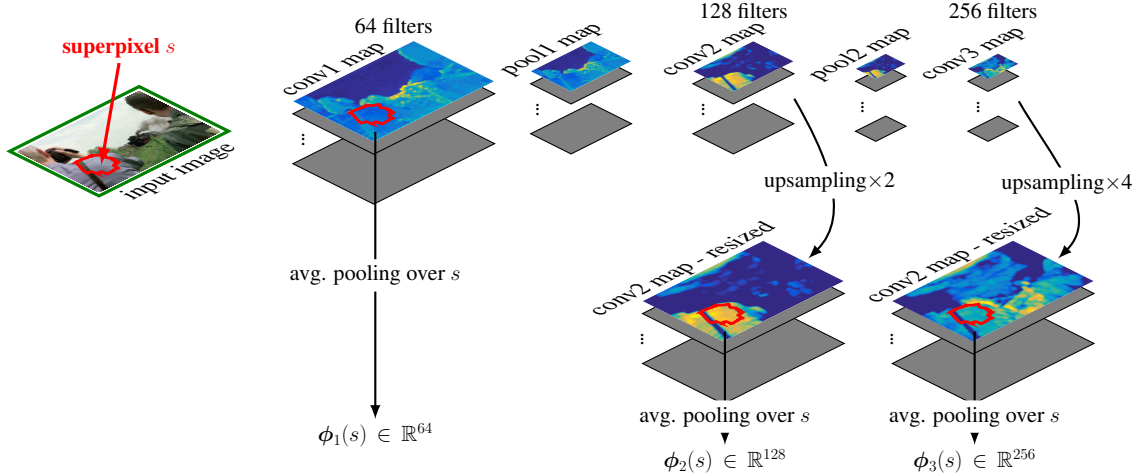


Figure 3.4: Illustration of zoom-out feature extraction procedure for a simple network with three convolutional and two pooling layers.

3.3.2 Learning to label with asymmetric loss

Once we have computed the zoom-out features we simply concatenate them into a feature vector representing a superpixel. For superpixel s in image \mathcal{I} , we will denote this feature vector as

$$\phi_{\text{zoom-out}}(s, \mathcal{I}) = [\phi_1(s, \mathcal{I}) \dots, \phi_L(s, \mathcal{I})]$$

where L is the number of levels in the zoom-out architecture. For the training data, we will associate a single category label y_s with each superpixel s . This decision carries some risk, since in any non-trivial over-segmentation some of the superpixels will not be perfectly aligned with ground truth boundaries. In Section 3.4 we evaluate this risk empirically for our choice of superpixel settings and confirm that it is indeed minimal.

Now we are ready to train a classifier that maps s in image \mathcal{I} to y_s based on $\phi_{\text{zoom-out}}$; this requires choosing the empirical loss function to be minimized, subject to regularization. In semantic segmentation settings, a factor that must impact this choice is the highly imbalanced nature of the labels. Some categories are much more common than others, but our goal (encouraged by the way benchmarks like VOC evaluate segmentations) is to predict them

equally well. It is well known that training on imbalanced data without taking precautions can lead to poor results [39, 40, 5]. A common way to deal with this is to stratify the training data; in practice this means that we throw away a large fraction of the data corresponding to the more common classes. We follow an alternative which we find less wasteful, and which in our experience often produces dramatically better results: use all the data, but change the loss. There has been some work on loss design for learning segmentation [48], but the simple weighted loss we describe below has to our knowledge been missed in segmentation literature, with the exception of [49] and [5], where it was used for binary segmentation.

Let the frequency of class c in the training data be f_c , with $\sum_c f_c = 1$. Our choice of loss is log-loss. We scale it by the inverse frequency of each class, effectively giving each pixel of less frequent classes more importance:

$$-\frac{1}{N} \sum_{i=1}^N \frac{1}{f_{y_i}} \log \hat{p}(y_i | \phi(s_i, \mathcal{I}_i)), \quad (3.3.1)$$

where $\hat{p}(y_i | \phi(s_i, \mathcal{I}_i))$ is the estimated probability of the correct label for segment s_i in image \mathcal{I}_i , according to our model. The loss in (3.4.1) is still convex, and only requires minor changes in implementation.

3.4 Experiments

Our main set of experiments focuses on the PASCAL VOC category-level segmentation benchmark with 21 categories, including the catch-all background category. VOC is widely considered to be one of the main semantic segmentation benchmarks. The original data set labeled with segmentation ground truth consists of `train` and `val` portions (about 1,500 images in each). Ground truth labels for additional 9,118 images have been provided by

authors of [50], and are commonly used in training segmentation models. In all experiments below, we used the combination of these additional images with the original `train` set for training, and `val` was used only as held out validation set, to tune parameters and to perform ablation studies.

The main measure of success is accuracy on the test, which for VOC 2012 consists of 1,456 images. No ground truth is available for test, and accuracy on it can only be obtained by uploading predicted segmentations to the evaluation server. The standard evaluation measure for category-level segmentation in VOC benchmarks is per-pixel accuracy, defined as Jaccard index or intersection of the predicted and true sets of pixels for a given class c , divided by their union (IoU in short).

$$IoU_c(\hat{y}, y) = \frac{|\{\hat{y} = c\} \cap \{y = c\}|}{|\{\hat{y} = c\} \cup \{y = c\}|} \quad (3.4.1)$$

in which y is provided ground truth labels and \hat{y} is predicted labels. This is averaged across the 21 classes to provide a single accuracy number, mean IoU, usually used to measure overall performance of a method.

3.4.1 Zoom-out feature extraction

We obtained roughly 500 SLIC superpixels [45] per image (the exact number varies per image), with the parameter m that controls the tradeoff between spatial and color proximity set to 15, producing superpixels which tend to be of uniform size and regular shape, but adhere to local boundaries when color evidence compels it. This results in average superpixel region of 450 pixels.

One way to compute zoom-out features is to set the number and scope of zoom-out levels manually, and use hand-crafted features to describe these levels. However, as we described in Section 3.3.1.1, we can utilize CNNs to provide both the feature values and the zoom-out levels. As it is shown in Table 3.2 the latter leads to a simpler implementation and superior performance comparing to zoom-out manual.

3.4.1.1 Manual zoom-out

To represent a superpixel we use a number of well known features as well as a small set of learned features.

Color We compute histograms separately for each of the three L^*a^*b color channels, using 32 as well as 8 bins, using equally spaced binning; this yields 120 feature dimensions. We also compute the entropy of each 32-bin histogram as an additional scalar feature (+3 dimensions). Finally, we also re-compute histograms using adaptive binning, based on observed quantiles in each image (+120 dimensions).

Texture Texture is represented by histogram of texton assignments, with 64-texton [2, 51] dictionary computed over a sampling of images from the training set. This histogram is augmented with the value of its entropy. In total there are 65 texture-related channels.

SIFT A richer set of features capturing appearance is based on “bag of words” representations computed over SIFT [52] descriptors. The descriptors are computed over a regular grid (every 8 pixels), on 8- and 18-pixel patches, separately for each L^*a^*b channel. All the descriptors are assigned to a dictionary of 500 visual words. Resulting assignment histograms are averaged for two patch sizes in each channel, yielding a total of 1500 values, plus 6 values for the entropies of the histograms.

Location Finally, we encode superpixel’s location, by computing its image-normalized coordinates relative to the center as well as its shift from the center (the absolute value of the coordinates); this produces four feature values.

Local CNN Instead of using hand-crafted features we could learn a representation for the superpixel using a CNN. We trained a network with 3 convolutional (conv) + pooling + RELU layers, with 32, 32 and 64 filters respectively, followed by two fully connected layers (1152 units each) and finally a softmax layer. The input to this network is the bounding box of the superpixel, resized to 25×25 pixels and padded to 35×35 , in L^*a*b color space. The filter sizes in all layers are 5×5 ; the pooling layers all have 3×3 receptive fields, with stride of 2. We trained the network using back-propagation, with the objective of minimizing log-loss for superpixel classification. The output of the softmax layer of this network is used as a 21-dimensional feature vector. Another network with the same architecture was trained on binary classification of foreground vs. background classes; that gives us two more features.

3.4.1.2 Proximal features

We use the same set of hand-crafted features as for local regions, but average them over superpixels in proximal region around each superpixel. This results in 1818 feature dimensions.

3.4.1.3 Distant and scene features

For distant and scene features we use deep CNNs originally trained to classify images. In our initial experiments we used the CNN-S network in [53]. It has 5 convolution layers (three of them followed by pooling) and two fully connected layers. To extract the relevant features, we resize either the distant region or the entire image to 224×224 pixels, feed it to

the network, and record the activation values of the last fully-connected layer with 4096 units. In a subsequent set of experiments we switched from CNN-S to a 16 layer network introduced in [54]. This network, which we refer to as VGG-16, contains more layers that apply non-linear transformations, but with smaller filters, and thus may learn richer representation with fewer parameters. It has produced excellent results on image classification and recently has been reported to lead to a much better performance when used in detection [55]. As reported below, we also observe a significant improvement when using VGG-16 to extract distant and global features, compared to performance with CNN-S. Note that both networks we used were originally trained for 1000-category ImageNet classification task, and we did not fine-tune it in any way on VOC data.

3.4.1.4 CNN-based zoom-out

Given a CNN, we associate a zoom-out level with every convolutional layer in the network. For the following experiments, we use the 16-layer network from [54], with the final classification layer removed. This network, which we refer to as VGG-16, has 13 convolutional layers, yielding 13 zoom-out levels (see Fig. 3.4). In Section 3.5 we apply zoom-out to modern backbones such as ResNet [56], DenseNet [57] and NASNet [58].

To compute sub-scene level features, we take the bounding box of superpixels within radius three from the superpixel at hand (i.e., neighbors, their neighbors and their neighbors' neighbors). This bounding box is warped to canonical resolution of 256×256 pixels, and fed to the CNN; the activations of the last fully connected layer are the window level features. Finally, the scene level features are computed by feeding the entire image, again resized to canonical resolution of 256×256 pixels, to the CNN, and extracting the activations of the last fully connected layer.

| Group | Level | Dim | Unit RF size | Region size |
|-------|----------|------|--------------|-------------|
| G1 | 1 | 64 | 3 | 32 |
| G1 | 2 | 64 | 5 | 36 |
| G2 | 3 | 128 | 10 | 45 |
| G2 | 4 | 128 | 14 | 52 |
| G3 | 5 | 256 | 24 | 70 |
| G3 | 6 | 256 | 32 | 84 |
| G3 | 7 | 256 | 40 | 98 |
| G4 | 8 | 512 | 60 | 133 |
| G4 | 9 | 512 | 76 | 161 |
| G4 | 10 | 512 | 92 | 190 |
| G5 | 11 | 512 | 132 | 250 |
| G5 | 12 | 512 | 164 | 314 |
| G5 | 13 | 512 | 196 | 365 |
| S1 | subscene | 4096 | – | 130 |
| S2 | scene | 4096 | – | varies |

Table 3.1: Statistics of the zoom-out features induced by the 16 layer CNN. Dim: dimension of feature vector. Unit RF size is size of receptive field of a CNN unit in pixels of 256×256 input image. Region size: average size of receptive field of the zoom-out feature in pixels of original VOC images. The group designation is referred to by design of experiments in Section 3.4.3.

Feature parameters are summarized in Table 3.1. Concatenating all the features yields a 12,416-dimensional representation for a superpixel. Following common practice, we also extract the features at all levels from the mirror image (left-right reflection, with the superpixels mirrored as well), and take element-wise max over the resulting two feature vectors.

| Method | mean IoU |
|---------------------------|----------|
| manual zoom-out CNN-S | 57.1 |
| manual zoom-out VGG-16 | 63.5 |
| CNN-based zoom-out VGG-16 | 69.9 |

Table 3.2: comparison of setting the number and scope of zoom-out levels manually versus CNN-based zoom-out.

3.4.2 Learning setup

To rule out significant loss of accuracy due to reduction of image labeling to superpixel labeling, we evaluated the achievable accuracy under “oracle” labeling. Assigning each superpixel a category label based on the majority vote by pixels in it produces mean IoU of 94.4% on VOC 2012 `val`. Thus, we can assume that loss of accuracy due to our commitment to superpixel boundaries is going to play a minimal role in our results.

With more than 10,000 images and roughly 500 superpixels per image, we have more than 5 million training examples. We trained various classifiers on this data, with asymmetric log-loss (3.4.1), using Caffe [59] on a single machine equipped with a Tesla K40 GPU. During training we used fixed learning rate of 0.0001, and weight decay factor of 0.001.

| Region type | oracle mIoU | zoom-out mIoU |
|----------------|-------------|---------------|
| SLIC-500 | 94.4 | 69.9 |
| rectangles-500 | 87.2 | 64.3 |

Table 3.3: Effect of replacing SLIC superpixels with an equal number of rectangular regions. Results on VOC 2012 `val`, mean class IoU.

3.4.3 Analysis of contribution of zoom-out levels

To assess the importance of features extracted at different zoom-out levels, we experimented with various feature subsets, as shown in Table 3.4. For each subset, we train a linear (softmax) classifier on VOC 2012 `train` and evaluate performance on VOC 2012 `val`. The feature set designations refer to the groups listed in Table 3.1.

It is evident that each of the zoom-out levels contributes to the eventual accuracy. Qualitatively, we observe that complex features computed at sub-scene and scene levels play a role in establishing the right set of labels for an image, while features derived from convolutional layers of the CNN are important in localization of object boundaries; a few examples in

Figure 3.6 illustrate this. We also confirmed empirically that learning with asymmetric loss leads to dramatically better performance compared to standard, symmetric loss (and no data balancing).



Figure 3.5: Color code for VOC categories. Background is black.

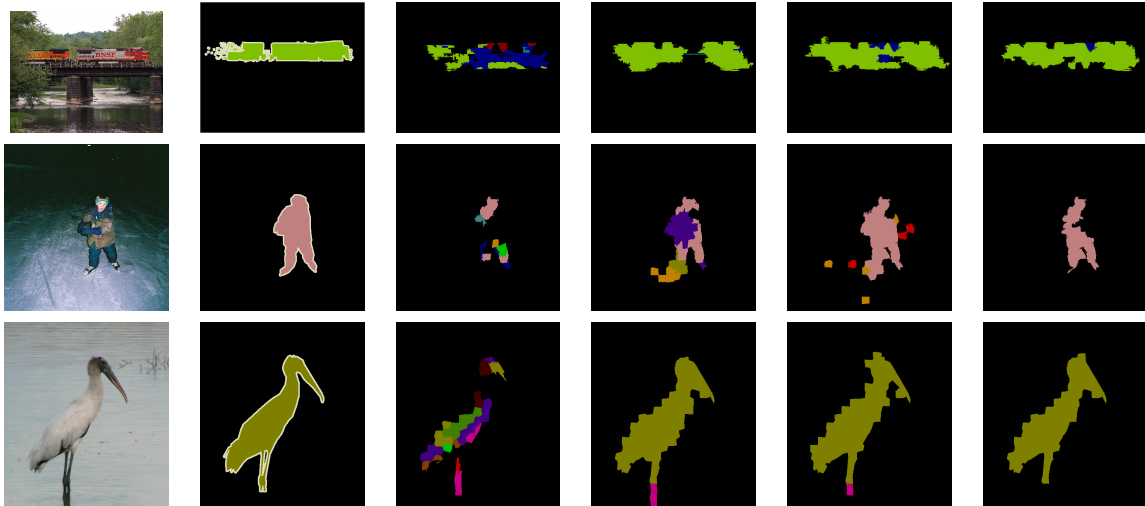


Figure 3.6: Examples illustrating the effect of zoom-out levels. From left: original image, ground truth, levels G1:3, G1:5, G1:5+S1, and the full set of zoom-out features G1:5+S1+S2. In all cases a linear model is used to label superpixels. See Figure 3.5 for category color code, and Table 3.1 for level notation.

| Feature set | mean IoU |
|---------------------------|-------------|
| G1 | 6.0 |
| G1-2 | 10.1 |
| G1-3 | 16.3 |
| G1-4 | 26.3 |
| G1-5 | 41.8 |
| G1-5+S1 | 51.2 |
| G1-5+S2 | 57.3 |
| G4-5+S1+S2 | 58.0 |
| full zoom-out: G1-5+S1+S2 | 58.6 |

Table 3.4: Ablation study: importance of features from different levels under linear superpixel classification. Results on VOC 2012 val, mean class IoU.

Next we explored the impact of switching from linear softmax models to multilayer neural networks, evaluating a sequence of models on VOC 2012 `val`. Introducing a single layer of 1024 hidden units, with RELU nonlinearity, increased IoU from 58.6 to 68.4; additional hidden units (1500 or 2048) didn't increase it further. Adding another layer with 1024 units, and introducing dropout [60] improved IoU to 69.9, and this is the model we adopt for final evaluation on the test set. The test results are shown in Table 3.5.

| Method | VOC2010 | VOC2011 | VOC2012 |
|--------------------------------|-------------|-------------|-------------|
| zoom-out (ours), CVPR15 | 69.9 | 69.4 | 69.6 |
| FCN-8s, CVPR15 [61] | – | 62.7 | 62.2 |
| Hypercolumns, CVPR15 [62] | – | – | 59.2 |
| DivMbest+CNN, arXiv14 [35] | – | – | 52.2 |
| SDS, ECCV14 [34] | – | 52.6 | 51.6 |
| DivMbest+rerank, CVPR13 [6] | – | – | 48.1 |
| Codemaps, ICCV13 [33] | – | – | 48.3 |
| <i>O2P</i> , ECCV12 [30] | – | 47.6 | 47.8 |
| Regions & parts, CVPR12 [29] | – | 40.8 | – |
| Harmony potentials, IJCV12 [8] | 40.1 | – | – |
| D-sampling, ICCV11 [38] | 33.5 | – | – |

Table 3.5: Results on VOC 2010, 2011 and 2012 test. Mean IoU is shown, see Table 3.6 for per-class accuracies of the zoom-out method.

To evaluate importance of our reliance on superpixels we also evaluated an architecture in which SLIC superpixels are replaced by an equal number of rectangular regions. The achievable accuracy on VOC 2012 `val` with this over-segmentation is 87.2, compared to 94.4 with superpixels. The difference is due to failure of the rectangular grid to adhere to boundaries around thin structures or fine shape elements. Similar gap persists when we apply the full zoom-our architecture to the rectangular regions instead of superpixels: we get mean IoU of 64.3, more than 5 points below the result with superpixels. These results are summarized in Table 3.3. In Section 3.5 we run set of experiments in which individual pixels are being classified rather than superpixels.

Finally, we investigated the effect of replacing VGG-16 from [54] with a previously widely

used 7-layer CNN referred to as CNN-S in [53]. This net almost identical to the celebrated AlexNet [63]. Our experience is consistent with previously reported results where the two networks were compared as feature extractors on a variety of tasks [55, 54, 61]: there is a significant drop in performance when we use the full zoom-out architecture using CNN-S compared to the zoom-out with VGG-16 (mean IoU 45.4 vs. 58.6).

| class | mean | bg |  |  |  |  |  |  |  |  |  |  |  |  |  |  |  |  |  |  |  | |
|-------|------|------|---|---|---|---|---|---|---|---|---|---|---|---|---|---|---|---|---|---|---|------|
| acc | 69.6 | 91.9 | 85.6 | 37.3 | 83.2 | 62.5 | 66 | 85.1 | 80.7 | 84.9 | 27.2 | 73.3 | 57.5 | 78.1 | 79.2 | 81.1 | 77.1 | 53.6 | 74 | 49.2 | 71.7 | 63.3 |

Table 3.6: Detailed results of our method on VOC 2012 test.

Figure 3.7 displays example segmentations. Many of the segmentations have moderate to high accuracy, capturing correct classes, in correct layout, and sometimes including level of detail that is usually missing from over-smoothed segmentations obtained by CRFs or generated by region proposals. On the other hand, despite the smoothness imposed by higher zoom-out levels, the segmentations we get do tend to be *under*-smoothed, and in particular include little “islands” of often irrelevant categories. To some extent this might be alleviated by post-processing; we found that we could learn a classifier for isolated regions that with reasonable accuracy decides when these must be “flipped” to the surrounding label, and this improves results on `val` by about 0.5%, while making the segmentations more visually pleasing. However, We do not pursue this ad-hoc approach, and instead discuss in Chapter 5 more principled remedies.

3.4.4 Results on Stanford Background Dataset

For some of the closely related recent work results on VOC are not available, so to allow for empirical comparison, we also ran an experiment on Stanford Background Dataset (SBD). It has 715 images of outdoor scenes, with dense labels for eight categories. We applied the

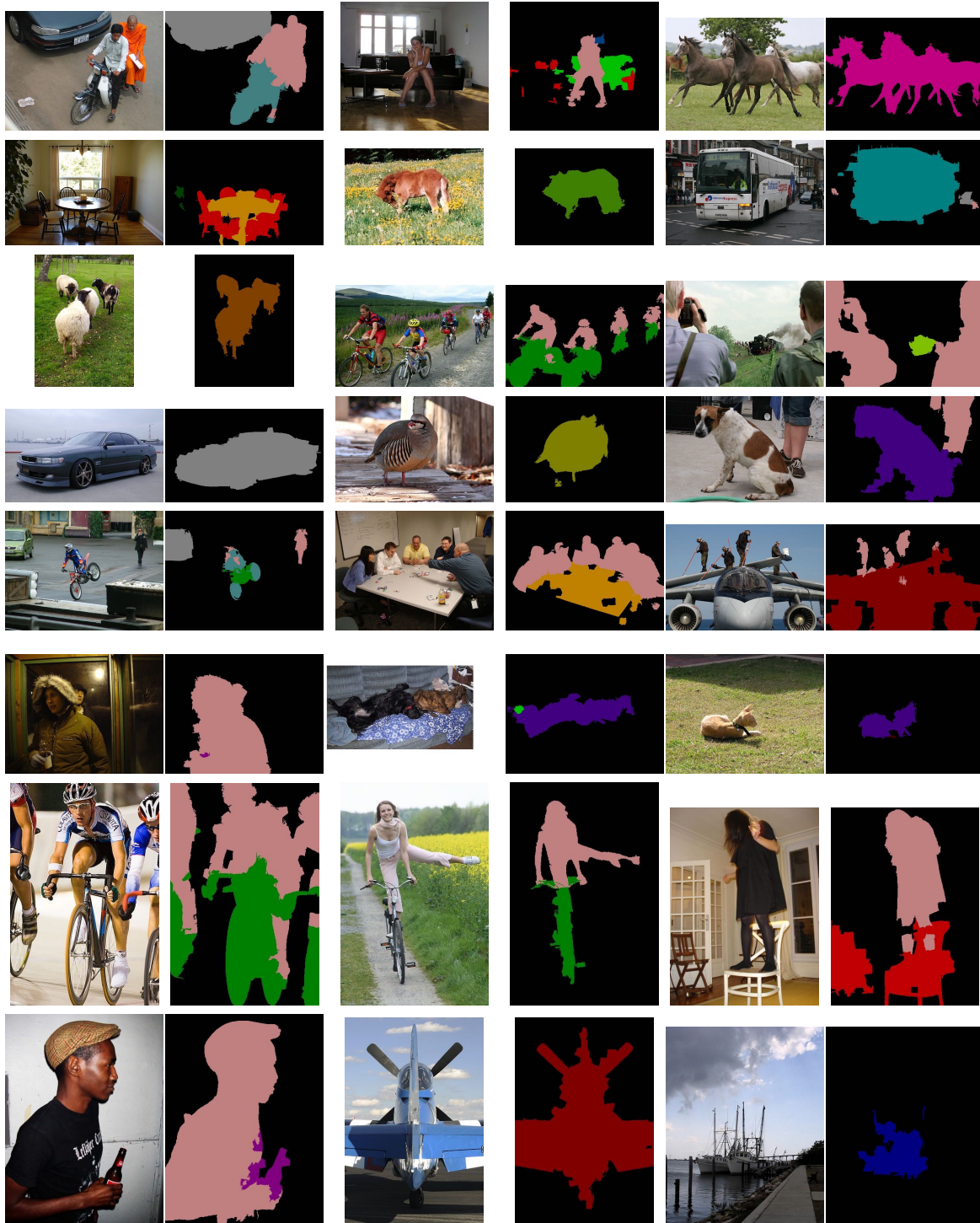


Figure 3.7: Example segmentations on VOC 2012 val with 3-layer neural network used to classify full zoom-out representation of superpixels (15 zoom-out levels). See Figure 3.5 for category color code.

same zoom-out architecture to this dataset as to VOC, except that the classifier had only 128 hidden units (due to much smaller size of the data set).

There is no standard train/test partition of SBD; the established protocol calls for reporting 5-fold cross validation results. There is also no single performance measure; two commonly reported measures are per-pixel accuracy and average class accuracy (the latter is different from the VOC measure in that it does not directly penalize false positives). The results in Table 3.7 show that the zoom-out architecture obtains results better than those in [40] and [39], both in class accuracy and in pixel accuracy.

| Method | pixel accuracy | class accuracy |
|---------------------|----------------|----------------|
| zoom-out (ours) | 86.1 | 80.9 |
| Multiscale CNN [39] | 81.4 | 76.0 |
| Recurrent CNN [40] | 80.2 | 69.9 |
| Pylon [5] | 81.9 | 72.4 |
| Recursive NN [41] | 78.1 | – |
| Multilevel [9] | 78.4 | – |

Table 3.7: Results on Stanford Background Dataset

3.5 Zoom-out with modern deep CNNs

In this section we explore the performance of zoom-out architecture by end-to-end training of zoom-out descriptors. We utilize modern deep CNNs such as ResNet [56], DenseNet [57] and NASNet [58] as a backbone of zoom-out architecture.

Huang *et al.* [57] introduced Dense Convolutional Network "DenseNet". DenseNet represents the latest high-performance evolution of ResNet-like designs. A DenseNet contains multiple dense blocks. A dense block consists of multiple convolutional layers where each layer is connected to every other layer. All layers within the same dense block operate on the feature maps of the same spatial size. Each convolutional layer within a dense block

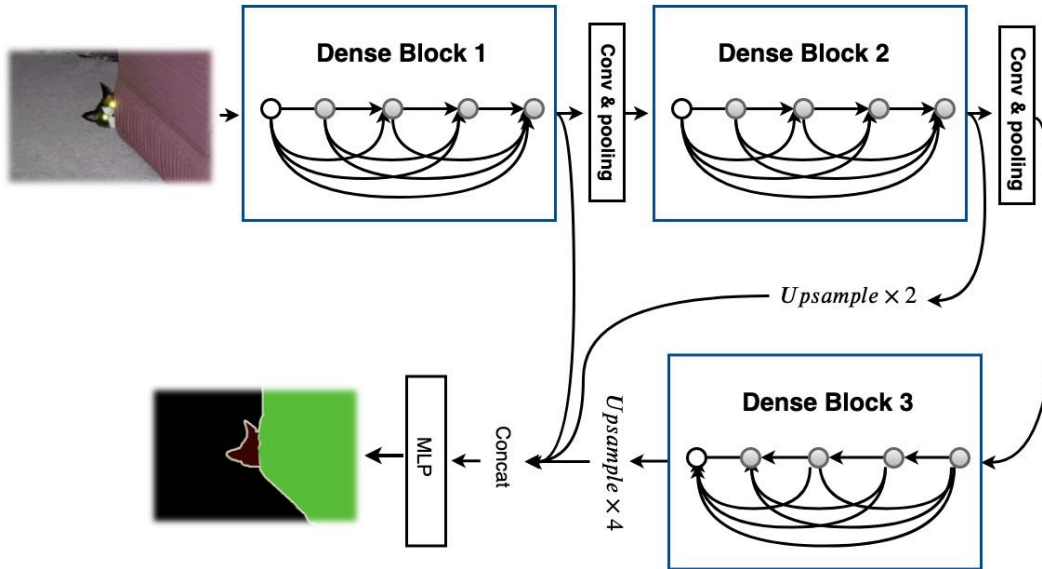


Figure 3.8: Illustration of zoom-out DenseNet with three dense blocks.

produces k feature maps at its output. The hyperparameter k is called the growth rate of DenseNet. After each dense block a down sampling operation is applied which increases the receptive field of the subsequent dense blocks. By using DenseNet as a backbone of the zoom-out architecture, we create direct connections from dense blocks at different scales to the prediction layer. The pixel classifier on top of zoom-out features consists of 3-layer CNN with 1×1 convolutions with 1000 hidden units in each layer. Figure 3.8 illustrates zoom-out DenseNet with three dense blocks. We use ImageNet pretrained 121-layer and 201-layer DenseNets. The growth rate for both DenseNets is 32.

We have also used ResNet as backbone of zoom-out architecture. For the case of ResNet, we extract zoom-out features at the end of each ResNet block before downsampling. Figure 3.9 shows zoom-out ResNet with three ResNet blocks. We also apply pyramid pooling module [14] to zoom-out features.

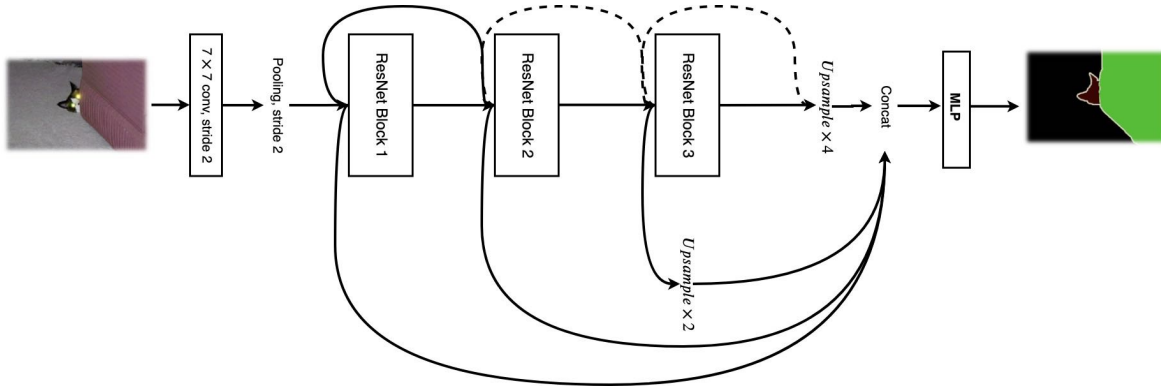


Figure 3.9: Illustration of zoom-out ResNet with three ResNet blocks. Dashed lines denote spatial size reduction of feature maps by the factor of two.

3.5.1 Experiments

Similar to previous settings, zoom-out spatial feature size is set to 1/4 of input image size. For the following experiments, we directly classify pixels rather than superpixels. Experiments are done in PyTorch [64], using the Adam [65] update rule when training networks. We keep the batch norm parameters of ImageNet pretrained backbones frozen. We train the classifier and fine-tune the backbone for 60 epochs with learning rates of 10^{-4} and 10^{-5} respectively. Then we decrease the learning rate to 10^{-5} for the classifier and to 10^{-6} for the backbone and train end-to-end for additional 40 epochs. We use a batch size of 12 when the models are trained on input of size 256×256 and batch size of 8 when the input size is 384×384 .

Data augmentation includes: a random horizontal flip and a crop of random size in the 0.5 to 2.0 range of the original size and a random aspect ratio of 3/4 to 4/3 of the original aspect ratio, which is finally resized to create a 256×256 or 384×384 image. Pretrained models are based on the PyTorch torchvision library [66].

When COCO [16] pretraining is used, we only train on images that contain one or more object classes that are in PASCAL. We consider COCO object classes that are not in PASCAL as background. This leaves us with around 80000 training images. Once the model is

converged, we fine tune it on PASCAL with initial learning rate of 10^{-5} for the pixel classifier and 10^{-6} for the COCO pretrained model.

Multi-scale inference refers to running inference on the validation images at multiple scales. We resize validation images such that the smaller side has lengths of 256, 384 and original length. The larger side of the image is resized such that resized image keeps the original aspect ratio. We also perform inference on the horizontally flipped images as well. For each of these inputs, we compute segmentation predictions and resize it to the original input size. At the end we average these predictions.

Table 3.8 summarizes zoom-out performance with DenseNet, ResNet and NASNet backbones on PASCAL VOC 2012 validation set. Using DenseNet, ResNet, or NASNet significantly improves results over zoom-out with VGG-16. This is consistent with the observation that we had earlier in section 3.4 when we replaced CNN-S with VGG-16. These results also demonstrate that zoom-out can easily be integrated with modern architectures and achieve comparable accuracy with recently proposed methods for semantic segmentation [67, 68]. Applying fully connected CRFs (2.1.2.1) to our best performing model, zoom-out NASNet-A adds 0.1% to mIoU. This minor improvement in mIoU suggests our zoom-out architecture has captured short-range and long-range dependencies between image elements.

| Method | Crop size | MS inference | COCO | Mean IoU |
|-----------------------|------------------|--------------|------|----------|
| zoom-out DenseNet-121 | 256×256 | - | - | 73.7 |
| zoom-out DenseNet-201 | 256×256 | - | - | 77.4 |
| zoom-out DenseNet-201 | 256×256 | - | - | 78.6 |
| zoom-out DenseNet-201 | 384×384 | ✓ | - | 79.6 |
| zoom-out NASNet-A | 384×384 | ✓ | - | 81.4 |
| zoom-out NASNet-A | 384×384 | ✓ | ✓ | 84.7 |
| zoom-out NASNet-A CRF | 384×384 | ✓ | ✓ | 84.8 |

Table 3.8: VOC12 validation mIoU of zoom-out with DenseNet and NASNet backbones.

Comparison with recent methods based on dilated/atrous convolution We compare zoom-out with recent approaches for semantic segmentation. The key idea behind atrous/dilated convolution was originally developed by Holschneider *et al.* [69] for wavelet decomposition. Dilated convolutions for semantic segmentation were introduced after zoom-out by Yu *et al.* [67]. Dilated convolution is designed to exponentially increase the receptive field of convolutional layers without sacrificing spatial resolution of feature maps by applying convolution to input with defined gaps. For the dilated ResNet experiments we use the model released by Zhou *et al.* [70]. A similar approach, called atrous convolution, has been also deployed in DeepLab architecture [68]. As it is shown in table 3.9, zoom-out achieves similar accuracy to the methods that use dilated/atrous convolution approach. However, it achieves similar accuracy with lower processing and memory consumption costs. In dilated convolution based architectures, mid to late stage DenseNet/ResNet blocks operate on feature responses with spatial resolution of size 1/8 of input, while in a normal ResNet/DenseNet these layers operate on gradually decreasing resolutions of 1/8, 1/16 and 1/32. Mid/late stage ResNet/DenseNet blocks contain convolutional layers with an increased number of channels, compared to early stage convolutional layers. Operating on large spatial resolution significantly reduces network speed. Table 3.8 shows further improvement in accuracy can be achieved by using zoom-out in conjunction with dilated ResNet.

| Method | Crop size | Mean IoU |
|-----------------------------|------------------|----------|
| dilated ResNet-101 | 256×256 | 77.4 |
| zoom-out ResNet-101 | 256×256 | 77.6 |
| zoom-out dilated ResNet-101 | 256×256 | 78.4 |
| zoom-out dilated ResNet-101 | 384×384 | 79.8 |

Table 3.9: VOC12 validation mIoU of zoom-out with dilated ResNet backbones.

We pick our best performing model, zoom-out NASNet-A and evaluate it on the test set of PASCAL dataset. Table 3.10 shows zoom-out results on VOC 2012 test set compared to state-of-the-art architectures. Figure 3.10 visualizes our results on the test set of VOC 2012.

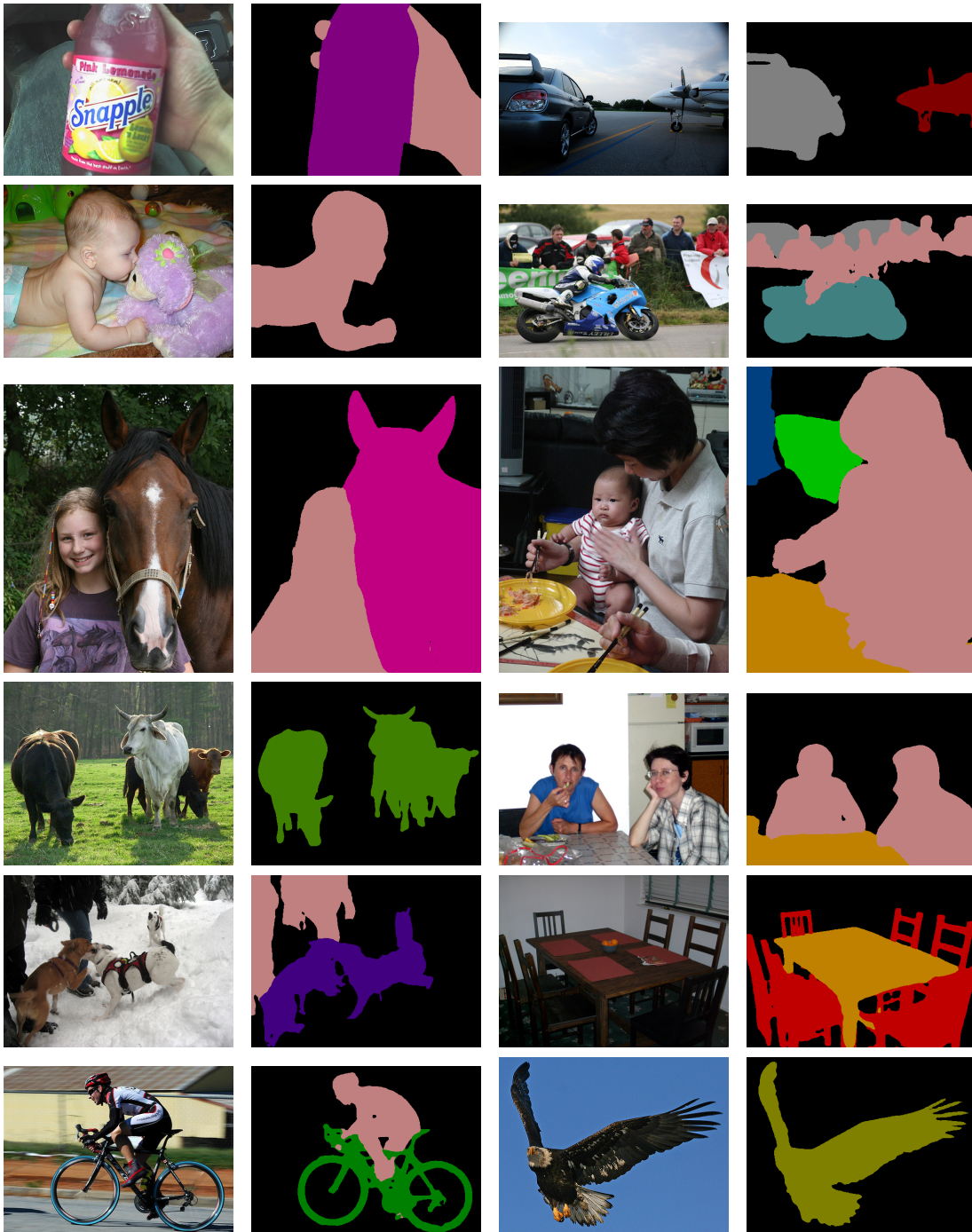


Figure 3.10: Example segmentations on VOC 2012 test set with our zoom-out NASNet-A.

| Method | mIoU |
|----------------------------|------|
| PSPNet [14] | 85.4 |
| DeepLabv3 [71] | 85.7 |
| DeepLabv3+ (Xception) [72] | 87.8 |
| MSCI [73] | 88 |
| zoom-out NASNet-A | 86.6 |

Table 3.10: Semantic segmentation results on VOC 2012 test. See Table 3.11 for per-class accuracies of the zoom-out method.

| class | mean | bb |  |  |  |  |  |  |  |  |  |  |  |  |  |  |  |  |  |  | | |
|-------|------|------|---|---|---|---|---|---|---|---|---|---|---|---|---|---|--|---|---|---|------|------|
| acc | 86.6 | 96.7 | 96.4 | 78.3 | 96.3 | 79.6 | 85.4 | 97.6 | 85.7 | 95.4 | 52.9 | 91.8 | 81.4 | 92.5 | 96.4 | 93.3 | 90.8 | 76.9 | 90 | 69.3 | 89.9 | 81.9 |

Table 3.11: Detailed results of our method on VOC 2012 test.

3.5.1.1 Results on Cityscapes dataset

Cityscapes is a rich urban scene understanding dataset [74]. It contains 5000 high quality pixel-level segmentation annotations of complex urban scene images. These 5000 annotated images are split to 2975, 500, 1525 training, validation and test sets respectively. In addition to 5000 finely annotated images, 20000 images are provided with coarse annotations. Segmentation annotations include 30 object classes. However, some of these classes are too rare and are excluded from standard benchmark. Following the standard benchmark, we evaluate our zoom-out model on semantic segmentation of 19 object categories. For the following experiments we train our models for 160 epochs on the 2975 finely annotated training images. For the zoom-out models we set the zoom-out features spatial size to be 1/8 of the input image size. We follow the training procedure and parameters of [75]. Table 3.12 shows the results of various architectures based on ResNet-101 backbone with pyramid pooling module [14]. In Table 3.12 similar to the results on PASCAL, zoom-out achieves similar accuracy to dilated convolution based model and once it is used in conjunction with dilated convolution it significantly improves the results. Figure 3.11 visualizes our results on on Cityscapes validation set.

| Method | Crop size | Mean IoU |
|-----------------------------|------------------|----------|
| dilated ResNet-101 | 512×512 | 76.5 |
| zoom-out ResNet-101 | 512×512 | 76.6 |
| zoom-out dilated ResNet-101 | 512×512 | 78.3 |

Table 3.12: Semantic segmentation results on Cityscapes validation set.

3.6 Summary

We presented zoom-out for learning and extracting rich representations. This chapter focused on the application of zoom-out architecture in semantic image segmentation. Despite apparent simplicity of our method and lack of explicit representation of the structured nature of the segmentation task, we showed that we can far surpass previous state of the art which was based on hand-crafted features with a random field or structured support vector machine model of considerable complexity. We were the first ones to show that segmentation, just like image classification, detection and other recognition tasks, can benefit from the advent of deep convolutional networks. Our further experiments with modern architectures such as DenseNet and ResNet in Section 3.5 revealed that zoom-out can achieve similar accuracy to recently proposed methods for semantic segmentation like dilated/atrous convolution while being faster and having less memory consumption. Furthermore, we showed that zoom-out can be applied to networks with dilated convolution as well and increase the accuracy. Having a powerful backbone network will significantly improve results as we observed a significant boost in accuracy by replacing CNN-S with VGG-16 and replacing VGG-16 with ResNet or DenseNet. In that regard, zoom-out can be easily applied to different choices of backbone CNN architectures. In the following we briefly mention some of the work/applications that have utilized zoom-out.

Abdominal lymph node detection Shin *et al.* [76] incorporate zoom-out multi-scale feature extraction strategy for thoraco-abdominal lymph node (LN) detection. Zoom-out multi-

scale feature extraction strategy led to their best performance model.

Pancreas segmentation Roth *et al.* [77] utilized zoom-out features for pancreas segmentation in abdominal computed tomography (CT) scans. They computed zoom-out features for each superpixel and then assigned each superpixel a probability of being pancreas. Farag *et al* [78] also used similar approach for pancreas segmentation.

Foreground extraction Kolkin *et al.* [79] utilized zoom-out features to compute a rich feature representation for each pixel. They proposed “squeezed zoom-out” architecture by adding squeeze module to zoom-out features, resulting in state-of-the-art performance in range of binary segmentation tasks.

Weakly-supervised segmentation Shimoda *et al* [80] used zoom-out features for the task of weakly-supervised segmentation.

Colorization Larsson *et al.* [81] utilized zoom-out representations for the task of automatic colorization of grayscale images.

Aerial urban scene classification Santana *et al* [82] used zoom-out features for aerial urban scene classification.

Optical remote sensing change detection. Amin *et al* [83] utilized zoom-out architecture to extract rich superpixel descriptors for optical remote sensing change detection.

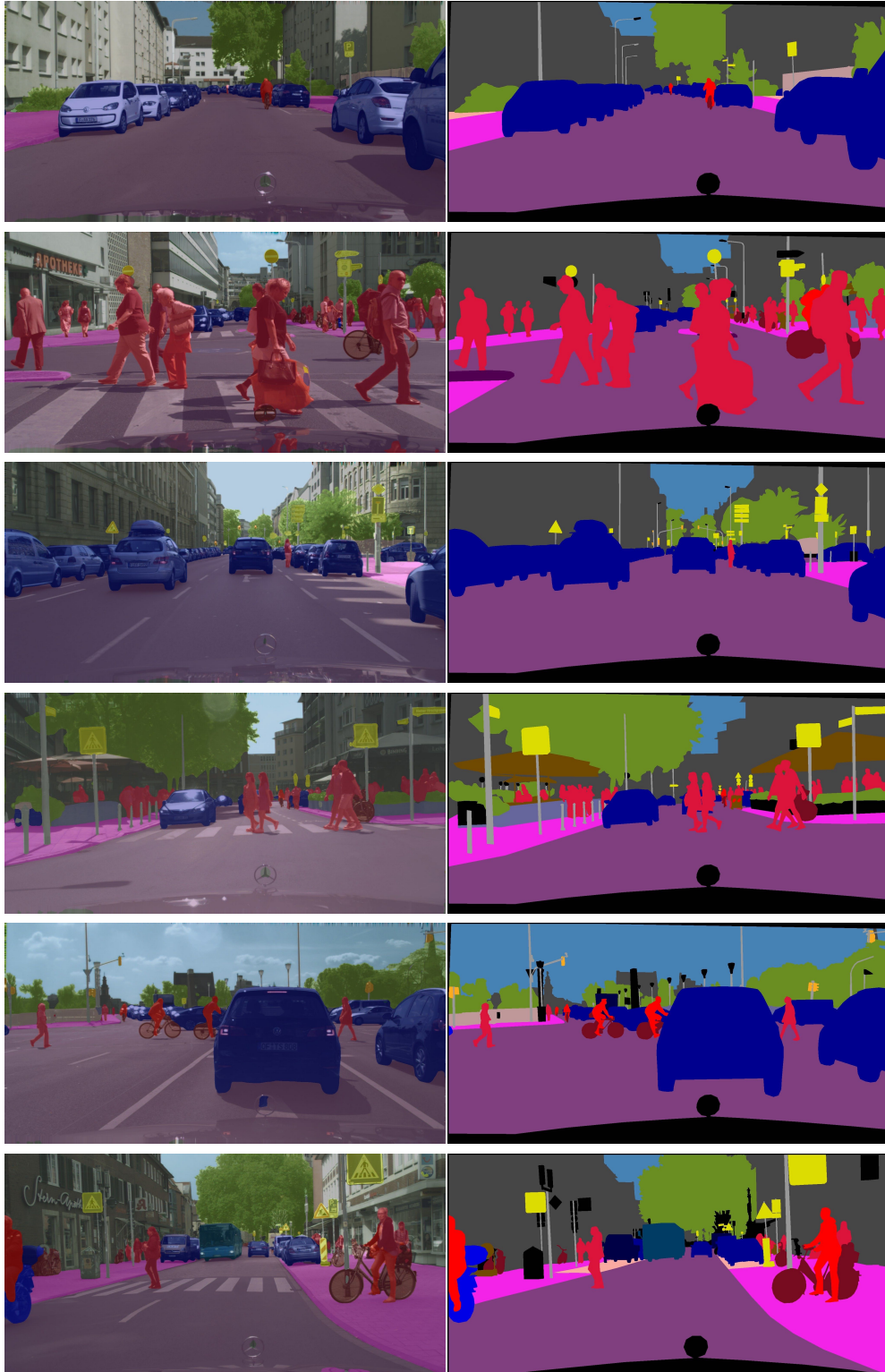


Figure 3.11: Visualization results of zoom-out dilated ResNet-101 on Cityscapes validation set. Left images are our semantic segmentation predictions overlay on RGB images. Right images are ground truth segmentations.

Chapter 4

Diverse Sampling for Weakly Supervised Learning of Semantic Segmentation

In this chapter we propose an approach for learning category-level semantic segmentation purely from image-level classification tags indicating presence of categories. It exploits localization cues that emerge from training a modified zoom-out architecture tailored for classification tasks, to drive a weakly supervised process that automatically labels a sparse, diverse training set of points likely to belong to classes of interest. Our approach has almost no hyperparameters, and allows for very fast training of segmentation models. It obtains competitive results on the VOC 2012 segmentation benchmark.

4.1 Introduction

Most recent progress can be attributed to advances in deep learning and to availability of large, manually labeled data sets. However, the cost and complexity of annotating segmentation are

significantly higher than that for classification; consequently, we have orders of magnitude more images and categories in classification data sets such as ImageNet [47] or Places2 [84], than in segmentation data sets, such as VOC [85] or MS-COCO [86].

Given this gap, and the objective difficulty in rapidly closing it, many researchers have considered weakly supervised segmentation, where the goal is still pixel-level labeling at test time, but only spatially coarse annotations are available at training time. Common examples of such annotations include partial annotations, in which only a subset of pixels is labeled; bounding boxes, where a square with an associated label is drawn around objects of interest; and image tags, where labels provide no spatial information and simply indicate whether or not a particular class is present *somewhere* in the image. We focus on this last, arguably weakest, level of per-image supervision.

There is mounting evidence that this task, while difficult, is not hopeless. Units sensitive to object localization have been shown to emerge as part of the representations learned by CNNs trained for image classification [87]. Furthermore, some localization methods demonstrate the utility of features learned by classification CNNs by using them to achieve competitive results [88, 87].

Our method is inspired by recent work [89] demonstrating that reasonable segmentation accuracy could be achieved with very few point-wise labels provided by human annotators. In this Chapter we propose an automatic version of this idea, replacing human annotators with an automatic labeling procedure. Our approach starts by learning noisy localization networks separately for each foreground class, trained solely with image-level classification tags, and using a novel multiple instance learning loss (global softmax, Section 5.3) adapted for the segmentation task. By combining the localization evidence provided by these networks with a novel diversity sampling procedure, we obtain a sparse, informative, and accurate set of labeled pixels. We can use these samples to rapidly train a fully convolutional multi-

class pixel-wise label predictor operating on hypercolumn/zoomout representation of image features [90, 91] in less than 3 minutes.

In contrast to much previous work, our approach is simple and modular. It almost entirely lacks hyper-parameters like thresholds and weighting coefficients. It also allows for easy addition of new foreground classes or incorporation of more image examples for some classes, without the need to retrain the entire system. We also avoid complex integration with externally trained components, other than the basic ImageNet-pretrained neural network we use to extract pixel features. Despite this simplicity we obtain results on the VOC 2012 data set that improve upon most of previous work on image-level weak supervision of segmentation.

4.2 Background

The availability of training data with manually annotated segmentation masks, in particular VOC [85] and recently MS-COCO [86], has been instrumental in these developments. However, recent work has shown that training on weaker annotations, such as partial labeling [89], object bounding boxes [92, 93, 94] or other cues such as object sizes [95], can produce results very close to those using strongly supervised training. However, closing this gap with strongly-supervised methods trained exclusively on image-level tags, which is the regime we consider in this Chapter, remains more challenging.

Our work was in part inspired by the experiments in [89] showing that very sparse point-wise supervision allows training reasonable CNN-based segmentation models. Our approach aims to replace manual annotation with a point-wise supervision obtained automatically from image-level tags. Similarly to other recent work, we obtain this supervision by leveraging the recently established observation: CNNs trained for image classification tasks appear to contain internal representations tuned to object localization [96, 87, 88, 97]. These representations

have been combined with a pooling strategy to obtain objects’ heat maps, which can be used to train a segmentation model, often with a variant of the Expectation-Maximization algorithm [92, 98] or with multiple instance learning (MIL) [99, 100, 101, 102].

There is a body of work related to exploring and exploiting diversity in learning and vision. Most relevant to our work is the DivMBest algorithm [103, 6] which somewhat resembles our procedure for greedy diverse sampling of points described in Section 4.3.2. The form of the diversity-infused objective and the context are quite different, however: DivMBest is used to sample assignments in a structured prediction settings for a single input example, whereas we aim to sample examples (image points); in applications of DivMBest the diverse samples are typically fed to a post-processing stage like reranking whereas in our case, the diverse sample is directly used as a training set for a segmentation algorithm.

Some recent methods combine image-level supervision with additional components, such as object proposals [100], saliency [104] or objectness measures [89]. Most of these components require localization annotations, such as bounding boxes and/or segmentation masks, which introduces a dependency on additional, often expensive annotations beyond image-level tags.

In contrast, our approach is simple and modular. The modularity of our method comes from the way that we compute objects’ heat maps. We train a separate classifier for each object class. This means for adding a new object class we simply train a classifier for that class without the need to retrain the entire model. Our approach does not require any external systems, other than the initial CNN [54] pretrained on the ImageNet classification task [47], making the entire pipeline independent of any requirements beyond image-level annotations.

The most established benchmark for this task is VOC 2012 dataset, with the standard performance measure being intersection over union averaged over 21 classes (mIoU). In Section 4.4 we show that despite its simplicity and efficiency, our approach outperforms most

competing methods on this benchmark.

4.3 Automatic point-wise supervision for segmentation

The basis of our bootstrapping method is the localization maps obtained for each of the foreground classes. These maps are sampled for each class, and the resulting sparse set of point-wise labels on the training images is used to train the final segmentation network. We describe these steps in detail below.

4.3.1 Learning localization with image-level tags

We start by extracting an image feature map using a pretrained fully convolutional network. Then for each foreground class c , we construct a per-location localization network on top of these features, which outputs two scores per-location i : $S(c, i)$ for foreground, and $\bar{S}(c, i)$ for background (which in this case means anything other than the foreground class at hand).

An obvious next step now is to convert these pixel-wise scores into image-level foreground/background probability score, using some sort of pooling scheme; this can then be used to compute image-level classification log-loss and backpropagate it to the localization network. We consider two such schemes.

The per-pixel softmax model We can convert the scores into per-location posterior probabilities using the standard softmax model, and apply max pooling over the resulting probability map:

$$p(c) = \max_i \frac{\exp S(c, i)}{\exp S(c, i) + \exp \bar{S}(c, i)}. \quad (4.3.1)$$

This can be interpreted as requiring that for images containing foreground class, the network assign at least one location high probability while for images without the foreground, all locations must have low probability. The background scores \bar{S} do not have a direct meaning other than to normalize the probabilities.

The global softmax model An alternative is to apply max-pooling *separately* for the two score maps, and convert the maxima to the image-level probability:

$$p(c) = \frac{\max_i \exp S(c, i)}{\max_j \exp S(c, j) + \max_l \exp \bar{S}(c, l)}. \quad (4.3.2)$$

This model no longer is equivalent to the per-location softmax, and in fact does not provide per-location probability map. It specifically encourages the background scores to be high for images without the foreground. It also routes the gradient of the loss via two locations in each image, instead of one with (4.3.1), and therefore may facilitate faster training.

It is worth noting that this approach does not include an explicit “background localization” model. Background is defined separately for each foreground class as its complement, and jointly as the complement of all foreground classes. Adding another foreground class would require only training one new localization model for that class; the definition of segmentation background would then automatically be updated, and reflected in the sampling process described below.

4.3.2 Sampling strategies

We now consider the goal of translating class-specific score maps to supervisory signal for semantic segmentation.

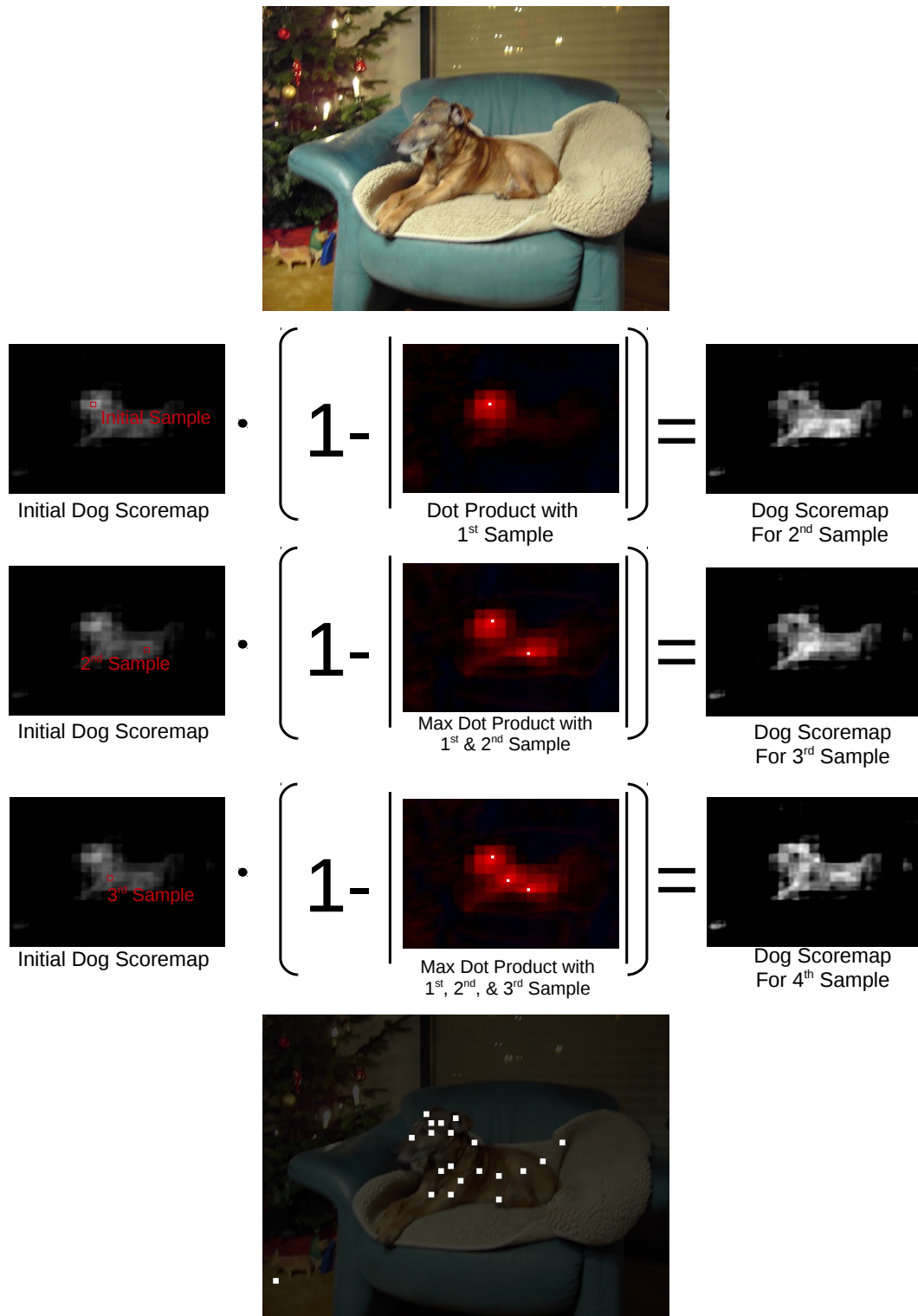


Figure 4.1: Our diverse sampling procedure. Left: input image, labeled as containing class dog. Middle: first four steps of diverse sampling procedure for dog, starting with the map $S(\cdot, \text{dog})$. Right: sample of 20 diverse points.

Our general framework for this will be to select a sparse set of locations from the training images, for which we will assign class labels. The segmentation predictor is then trained by learning to map the image features for these locations to the assigned class labels.

Let $S(i, c)$ be the score at spatial index i for a class c produced by our image-level classification model. One approach would be to densely label $y_i = \operatorname{argmax}_c S(i, c)$. Background requires a separate treatment: it is not a “real” class, rather it’s defined by not being one of the foreground classes. Hence, we do not have a separate model for it, and instead can assign background labels to pixels in which no foreground class attains a sufficient score: $y_i = bg$ if $\max_c S(i, c) < \tau$. This simplistic strategy has two problems: (1) some classes may have systemically lower scores than others, and (2) it is unclear how to optimally set the value of τ .

However, our hypothesis is that while the scoremaps provide only coarse localization, and an inconsistent level of confidence across images and classes, the maximum activations of a class scoremap when that class is present appear to reliably correspond with pixels containing the correct class. (We verified this qualitatively, on a few classes and a number of training images). So, an alternative approach is to label as c the k locations corresponding with highest scores for class c . However the size of objects varies widely across images, and it isn’t clear what k should be. If k is too high, the labels will be very noisy. If k is too low, most of the pixels will be tightly clustered portions of each class, e.g., wheels of cars, or faces of people; training on such examples is much less effective because many of the samples will highly correlated.

The method we propose here alleviates these problems by relying on *diversity sampling*. Let \mathbf{z}_i be the image feature vector at spatial index i , normalized to unit norm, and let F be the set of foreground classes present in the image. For each class $c \in F$ we define the k th

sampled location x_k^c from that image by induction:

$$x_1^c = \operatorname{argmax}_i S(i, c), \quad (4.3.3)$$

$$x_k^c = \operatorname{argmax}_i \left\{ S(i, c) \left[1 - \max_{k' < k} \left| \mathbf{z}_i \cdot \mathbf{z}_{x_{k'}^c} \right| \right] \right\}. \quad (4.3.4)$$

where \cdot denotes the dot product. In other words, we aim to select points with the highest scores for class c , but penalize them for similarity to previously selected points for that class. This encourages selection of a set of examples that jointly provides more information (due to diversity), and is likely to be accurate (due to high scores).

The definition of similarity as dot product in feature space, rather than as spatial proximity, is important. If features at two points are similar, they will appear as similar to the eventual pixel classifier (since it operates on those features), regardless of how close they are in the image; labeling only one of them is sufficient. On the other hand, two points nearby may have very different feature representations and thus it is beneficial to label both to give the pixel classifier more information.

This approach also naturally leads to a threshold-free method for selecting background points. We let the k^{th} sample, x_k^{bg} for be defined as:

$$x_k^{bg} = \operatorname{argmin}_i \max \left\{ \max_{c \in F, k'} \left| \mathbf{z}_i \cdot \mathbf{z}_{x_{k'}^c} \right|, \max_{k'' < k} \left| \mathbf{z}_i \cdot \mathbf{z}_{x_{k''}^{bg}} \right| \right\} \quad (4.3.5)$$

where k' ranges over indices of selected points for each foreground class, and k'' ranges over points selected so far for the background. This simply searches at each step for the image location most dissimilar to any foreground points to maximize the chance of correctly identifying background points, and to any other background points selected so far to maximize diversity. Our diversity sampling strategy is illustrated in Figures 4.1, 4.3.

4.3.3 Training semantic segmentation using point-wise supervision

Once the automatically point-wise labels are obtained, we are ready to train the segmentation as a per-pixel fully convolutional multi-class (including background) classifier network, with receptive field of 1×1 . This can be done by using the standard convnet training machinery, with zero-masking applied to the loss in locations where no labels are available; whether to fine-tune the underlying network that extracts the visual features per location is a choice.

4.4 Experiments

In order to compare our method to other work on segmentation, we conduct all of our experiments on the VOC 2012 data set. For training images (10,582 images in the train-aug set) we discard all annotations except for image-level labels indicating which of the 20 foreground classes is present in each image. We evaluate various versions of our method, as well as its components individually, on the validation set, and finally use the models chosen based on these experiments to obtain results on the test set from the VOC evaluation server. All experiments were done in Torch7, using Adam [105] update rule when training networks.

4.4.1 Experimental setup

Pixel features As the base CNN we use the VGG-16 network trained on ImageNet and publicly available from the authors of [54], from which we remove all layers above pool. This network is run in the fully convolutional mode on input images resized to 256×336 pixels. Then each of the 13 feature maps (outputs of all convolutional layers, with pooling applied when available) is resized to 1/4 of the input resolution, and concatenated along feature dimensions. This produces a tensor in which each location on the coarse 64×84 grid

has a 4,224-dimensional feature vector. This closely follows the zoom-out extraction protocol in [91], but without superpixel pooling.

When computing dot products in diversity sampling (4.3.3),(4.3.5) we normalize zoom-out feature vectors to unit norm in two stages: each feature dimension is normalized to be zero-mean, unit variance over the entire training set, then each feature vector is scaled to be unit Euclidean norm.

Localization models For each class, the fully convolutional localization network consists of a 1×1 convolutional layer with 1024 units, followed by ReLU and the 1×1 convolutional layer with 2 units, which outputs the score maps S for the foreground and \bar{S} for background. At training time, for the global softmax model (4.3.2) this is followed by global max pooling layer and the softmax layer, while for the per-pixel softmax (4.3.1) the order of softmax and max pooling is reversed.

For each class, we train the network on all positive examples for that class (images that contain it) and a randomly sampled equal number of negative examples, with batch size of 1 image, learning rate 10^{-4} which after 2 epochs is decreased to 10^{-5} for one additional epoch and momentum 0.9.

We experimented with adding higher layer features (fc7 from VGG-16) to the input to localization networks, but found that it makes localization worse: it is too easy for the network to determine presence of objects from these complex, translation invariant features. We do however bring these features back when training the final segmentation model, described next.

Segmentation model To provide image-level priors, which have been reported to improve segmentation results in both fully supervised [91] and weakly supervised [100] settings, we augment the zoom-out feature map with the global features (layer fc7 of VGG-16, pooled over

the entire image and replicated for all locations). The combined feature map (8320 features per location) is fed to a 1×1 convolutional layer with 512 units, followed by ReLU, and the 21-channel prediction layer, followed by the softmax loss layer. We train this network on the selected set of points pooled over all training images, using batch size 100 (note: this means 100 sample points, not 100 images!), fixed learning rate 10^{-6} , and momentum 0.9, for two epochs. With these settings, typical time to train the final segmentation model is less than 3 minutes on a single Titan X GPU.

4.4.2 Evaluation of model components

We start by evaluating components of our approach on the validation set.

Localization model As shown in Table 4.1, the global softmax model (4.3.2) obtains significantly better results than the per-pixel softmax (4.3.1). Therefore we choose it for all the subsequent experiments.

| Model | mIoU |
|----------------|------|
| Pixel softmax | 38.0 |
| Global softmax | 40.6 |

Table 4.1: Comparison of localization models on VOC 2012 validation set

Bootstrapping by localization maps We could attempt using the score maps obtained by localization network directly as the predicted segmentation maps. Specifically, we considered assigning each pixel to the highest scoring class (after normalizing the scores so that for each class on average images with the foreground present have the highest score of 1), or to the background if the highest foreground score is below threshold. This results in poor segmentation accuracy: the highest validation mIoU after sweeping the threshold values was

25.66, for threshold of 0.2.

We also made an attempt to use these score-based segmentation maps as the source of bootstrapping directly, without sampling. That is, we can train the segmentation network in the usual fully-supervised way, giving it the score map-based dense segmentation labels as if it were ground truth. The results were very poor; in large fraction of the pixels the localization models are uncertain, and densely localized labels will force the segmentation model to make a decision in those uncertain points as well, leading to a very noisy labeling.

Effect of sampling strategy For our diverse sampling method, we need to set the value of k . Table 4.2 shows the effect this value has on VOC 2012 validation mean IoU. The optimal k among those tested is 20, but the behavior is stable across a large range of values.

We also compared alternative sampling strategies, namely selecting the top k scoring points for each class, or using diversity but in spatial domain instead of in feature domain. Table 4.3 shows that the diversity sampling using feature similarity is indeed superior to those. Figure 4.3 shows a few qualitative examples of diverse sampling outputs. Notably, sampling for background is usually quite accurate, even though it is oblivious to the actual class scores and is entirely driven by diversity with respect to the foreground and within background.

| | | | | | |
|------|------|------|------|------|------|
| k | 1 | 5 | 10 | 20 | 50 |
| mIoU | 35.1 | 37.2 | 39.3 | 40.6 | 40.4 |

Table 4.2: mIoU on VOC 2012 validations set as a function of k points in diverse sampling, with global softmax model

| | |
|-------------------|------|
| Sampling | mIoU |
| Dense | 15.0 |
| Spatial | 33.4 |
| Top $k = 20$ | 30.7 |
| Diverse, $k = 20$ | 40.6 |

Table 4.3: Comparison of point sampling strategies

4.4.3 Final segmentation results

Based on the preliminary experiments on the validation above, we identify the optimal setting for our approach: global softmax localization model, with diverse sampling, $k = 20$. We report the results of this method in Table 4.4. We also report the results of applying fully connected CRF [3] with author’s default parameters on top of our predictions.

| Method | VOC2012 validation | VOC2012 test | comments |
|------------------|--------------------|--------------|-----------------------------------|
| DeepLab-CRF[106] | 68.7 | 71.6 | fully supervised |
| FCRN[107] | 74.8 | 77.3 | fully supervised |
| BoxSup[93] | 62.0 | 64.6 | bounding box-supervised |
| Bbox-Seg[92] | 60.6 | 62.2 | bounding box-supervised |
| 1 point [89] | 35.1 | | manual annotation, 1 pt/class |
| 1 point+Obj [89] | 42.7 | | + objectness prior |
| STC[104] | 49.8 | 51.2 | externally trained saliency model |
| MIL-sppx [100] | 36.6 | 35.8 | superpixel smoothing |
| CCCN [95] | 35.3 | 35.6 | |
| EM-Adapt [92] | 38.2 | 39.6 | |
| SEC[102] | 50.7 | 51.5 | |
| Ours | 40.6 | 41.2 | no post-processing |
| Ours | 45.2 | 46.0 | CRF post-processing |

Table 4.4: Comparison of competitive segmentation methods, supervised with image-level tags. For reference, top of the table includes methods trained with stronger supervision on VOC 2012 data, or on additional data.

The top portion of the table contains representative results for stronger supervision scenarios, for reference; these are not directly comparable to our results. Among the methods trained on the same data and in the same regime as ours, our results are the highest. It is interesting that we obtain similar results to those with *manual* annotation of a single point per class per image [89] (better than their results without objectness prior), although our point selection is fully automatic.

STC [104], achieves test mIoU of 51.2. It is trained on 40,000 additional images, collected in a carefully designed procedure to make them easy to learn from. STC also uses an externally trained saliency mechanism, which requires mask annotations to train.

SEC [102] is trained solely on VOC data which has higher accuracy, achieving 51.5 mIoU on the test set. However, their approach is considerably more complex than ours, employing hyperparameters that determine various thresholds, and the time to train the final segmentation system with SEC is almost two orders of magnitude higher than ours. SEC also uses significantly larger field of view for the underlying segmentation network than in our experiments (378 vs. 224 for us), and results reported in [102] suggest that this may be very important.

Adding new object classes on the fly One of the key characteristics of our model is modularity. Consider that we want to add new classes like Giraffe and Elephant which are not part of VOC dataset. We train localization model for new classes with only image level tags from MS-COCO dataset for Giraffe and Elephant. Since we have trained the localization model for each class separately, there is no need to re-train the other classes localization models. The segmentation training data for new classes is the sparse set of diverse points extracted from localization model output. Sparsity significantly speeds the segmentation training and diversity leads to high quality segmentation output. It takes less than 3 minutes to re-train the segmentation model with additional classes, without hurting its accuracy on VOC segmentation benchmark. Hence, it is practical to add new classes on the fly. Qualitative examples of segmentation results for the new classes are shown in Figure 4.2.

4.5 Summary

We have proposed an approach to learning category-level semantic segmentation when the only annotation available is tags indicating the presence (or absence) of each foreground class in each image. Our approach is based on a form of bootstrapping, in which a sparse, visually

diverse set of points in training images is labeled based on class-specific localization maps, predicted from the image tags.

Among the appealing properties of our method are its simplicity, near absence of hyperparameters (and insensitivity to the only hyperparameter, the sample size), modularity (easy to update the model with new classes and/or examples), lack of reliance on complex external components requiring strong supervision, and last but not least, competitive empirical performance and speed.

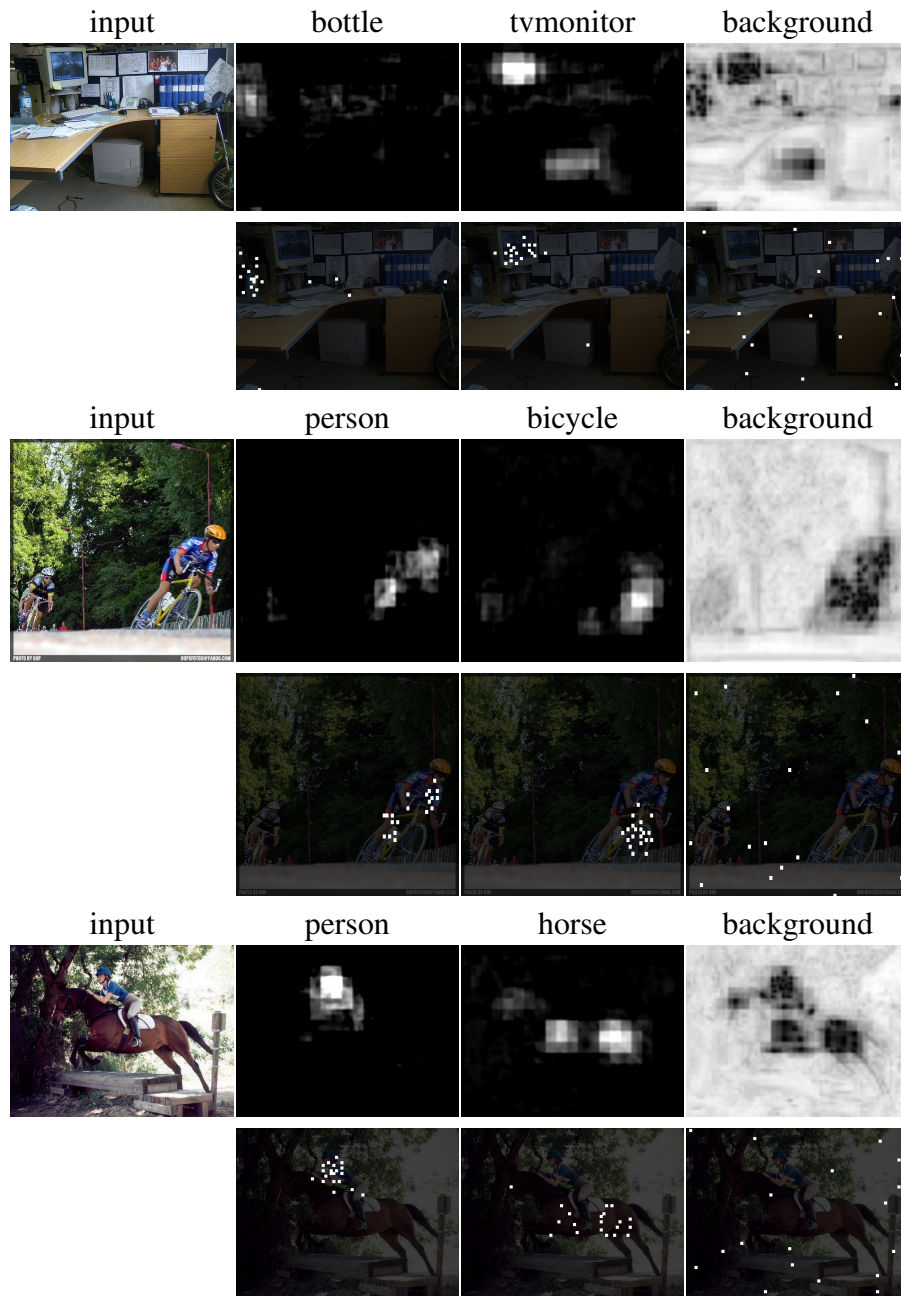


Figure 4.3: Examples of diverse sampling outputs. For each foreground class, we show the localization score map from global softmax model, and the selected 20 points. For background, the map shows the max over dot products with any selected foreground points.



Figure 4.4: Examples of segmentations learned through our weakly supervised approach. From left: input image, ground truth, thresholded localization score maps, segmentation learned with diverse $k = 20$ sampling, CRF post-processing.

Chapter 5

Label Embedding

In the first part of this chapter we introduce custom regularization functions for use in supervised training of deep neural networks. Our technique is applicable when the ground-truth labels themselves exhibit internal structure; we derive a regularizer by learning an autoencoder over the set of annotations. In the second part of this chapter, we explore how well we can predict depth maps directly from semantic segmentation maps and propose a two-part architecture for joint prediction of depth and semantic segmentation.

5.1 Introduction

The recent successes of supervised deep learning rely on the availability of large-scale datasets with associated annotations for training. In computer vision, annotation is a sufficiently precious resource that it is commonplace to pretrain systems on millions of labeled ImageNet [11] examples. These systems absorb a useful generic visual representation ability during pretraining, before being fine-tuned to perform more specific tasks using fewer labeled

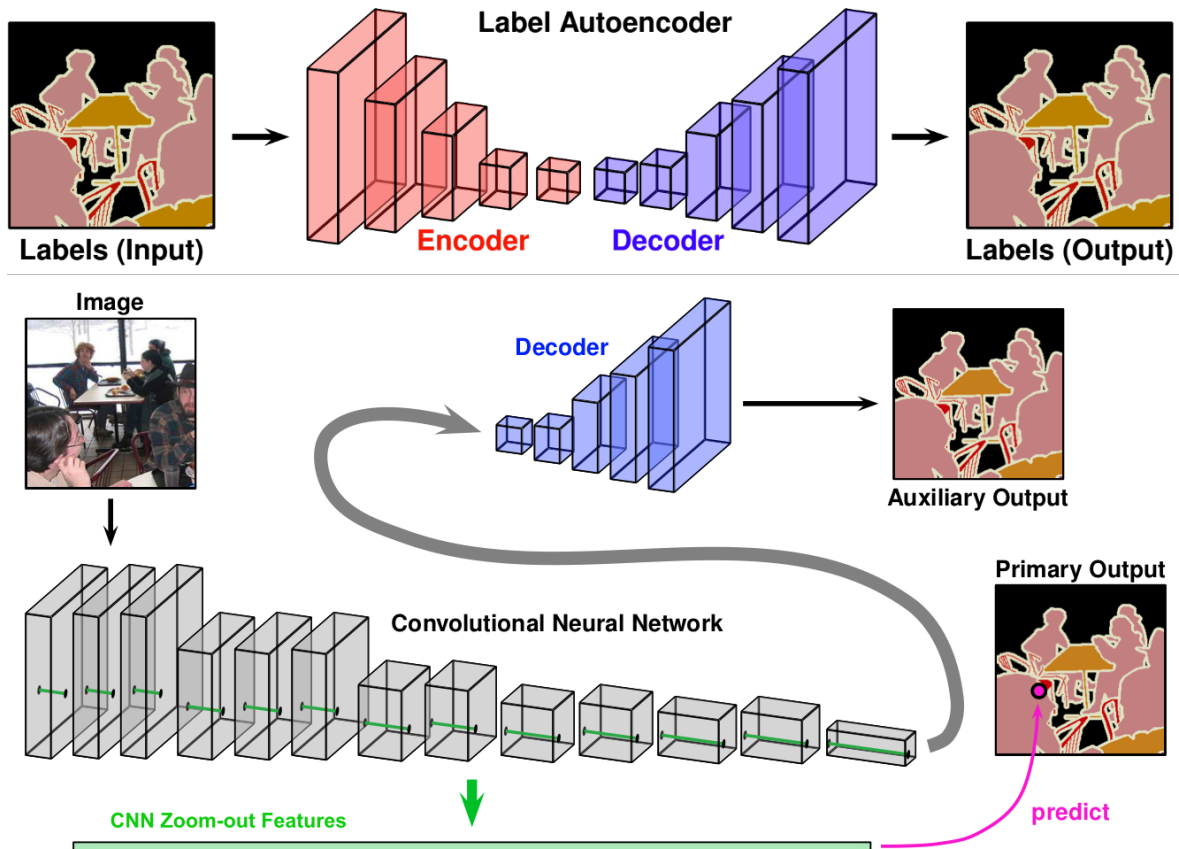


Figure 5.1: Exploiting label structure when training semantic segmentation. Top: An initial phase looks only at the ground-truth annotation of training examples, ignoring the actual images. We learn an autoencoder that approximates an identity function over segmentation label maps. It is constrained to compress and reconstitute labels by passing them through a bottleneck connecting an encoder (red) and decoder (blue). Bottom: The second phase trains a standard CNN for semantic segmentation using zoom-out features for per-pixel output. However, we attach an auxiliary branch (and loss) that also predicts segmentation by passing through the decoder learned in the first phase. After training, we discard this decoder branch, making the architecture appear standard.

examples.

Current state-of-the-art semantic segmentation methods [12, 13, 14] follow such a strategy. Its necessity is driven by the high relative cost of annotating ground-truth for spatially detailed segmentations [15, 16], and the accuracy gains achievable by combining different data sources and label modalities during training. A collection of many images, coarsely annotated with a

single label per image (ImageNet [11]), is still quite informative in comparison to a smaller collection with detailed per-pixel label maps for each image (PASCAL [15] or COCO [16]).

We show that detailed ground-truth annotation of this latter form contains additional information that existing schemes for training deep convolutional neural networks (CNNs) fail to exploit. By designing a new training procedure, we are able to capture some of this information, and as a result increase accuracy at test time.

Our method is orthogonal to recent efforts, discussed in Section 5.2, on learning from images in an unsupervised or self-supervised manner [108, 109, 110, 81, 111, 112, 113]. It is not dependent upon the ability to utilize an external pool of data. Rather, our focus on more efficiently utilizing provided labels makes our contribution complementary to these other learning techniques. Experiments show gains both when training from scratch, and in combination with pretraining on an external dataset.

Our innovation takes the form of a regularization function that is itself learned from the training set labels. This yields two distinct training phases. The first phase models the structure of the labels themselves by learning an autoencoder. The second phase follows the standard network training regime, but includes an auxiliary task of predicting the output via the decoder learned in the first phase. We view this auxiliary branch as a regularizer; it is only present during training. Figure 5.1 illustrates this scheme.

Section 5.3 further details our approach and the intuition behind it. Our regularizer can be viewed as a requirement that the system understand context, or equivalently, as a method for synthesizing context-derived labels at coarser spatial resolution. The auxiliary branch must predict this more abstract, context-sensitive representation in order to successfully interface with the decoder.

Experiments, covered in Section 5.4, focus on the PASCAL semantic segmentation task.

We take baseline CNN architectures, the established VGG [114] network and the state-of-the-art DenseNet [57], and report performance gains from enhancing them with our custom regularizer during training. Section 5.4 also provides ablation studies, explores an alternative regularizer implementation, and visualizes representations learned by the label autoencoder.

Results demonstrate performance gains under all settings in which we applied our regularization scheme: VGG or DenseNet, with or without data augmentation, and with or without ImageNet pretraining. Performance of a very deep DenseNet, with data augmentation and ImageNet pretraining, is still further improved with use of our regularizer during training. Together, these results indicate that we have discovered a new and generally applicable method for regularizing supervised training of deep networks. Moreover, our method has no cost at test time; it produces networks architecturally identical to baseline designs.

Section 5.6 discusses implications of our demonstration that it is possible to squeeze more benefit from detailed label maps when training deep networks. Our results open up a new area of inquiry on how best to build datasets and design training procedures to efficiently utilize annotation.

5.2 Related work

The abundance of data, but more limited availability of ground-truth supervision, has sparked a flurry of recent interest in developing unsupervised or weakly supervised methods for training deep neural networks. Here, the idea is to utilize a large reserve of unlabeled data in order to prime a deep network to encode generally useful visual representations. Subsequently, that network can be fine-tuned on a novel target task, using actual ground-truth supervision on a smaller dataset. Pretraining on ImageNet [11] currently yields such portable representations [115], but lacks the ability to scale without requiring additional

human annotation effort.

Recent research explores a diverse array of data sources and tasks for self-supervised learning. In the domain of images, proposed tasks include inpainting using context [108], solving jigsaw puzzles [109], colorization [110, 81, 111], cross-channel prediction [112], and learning a bidirectional variant [113] of generative adversarial networks (GANs) [116]. In the video domain, recent works harness temporal coherence [117, 118], co-occurrence [119], and ordering [120], as well as tracking [121], sequence modeling [122], and motion grouping [123]. Owens *et al.* [124] explore cross-modality self-supervision, connecting vision and sound. Agrawal *et al.* [125] and Nair *et al.* [126] examine settings in which a robot learns to predict the visual effects of its own actions.

Training a network to perform ImageNet classification or a self-supervised task, in addition to the task of interest, can be viewed as a kind of implicit regularization constraint. Zhang *et al.* [127] explore explicit auxiliary reconstruction tasks to regularize training. However, they focus on encoding and decoding image feature representations. Our approach differs entirely in the source of regularization.

Specifically, by autoencoding the structure of the target task labels, we utilize a different reserve of information than all of the above methods. We design a new task, but whereas self-supervision formulates the new task on external data, we derive the new task from the annotation. This separation of focus allows for possible synergistic combination of our method with pretraining of either the self-supervised or supervised (ImageNet) variety. Section 5.4 tests the latter.

Another important distinction from recent self-supervised work is that, as detailed in Section 5.3, we use a generic mechanism, based on an autoencoder, for deriving our auxiliary task. In contrast, the vast majority of effort in self-supervision has relied on using domain-

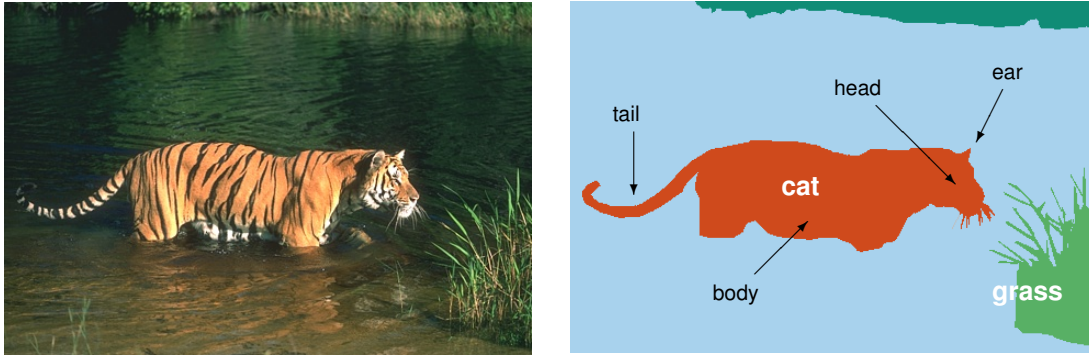


Figure 5.2: Informative structure in annotation. The shape of labeled semantic regions hints at unlabeled parts (black arrows). Object co-occurrence provides a prior on scene composition. specific knowledge to formulate appropriate tasks. Inpainting [108], jigsaw puzzles [109], and colorization [110, 81, 111] exemplify this mindset; BiGANs [113] are perhaps an exception, but to date their results compare less favorably [111].

The work of Xie *et al.* [128] focuses on learning a shallow corrective model that essentially denoises a predicted label map using center-surround filtering. In contrast, we build a deep model of label space. Also, unlike [128], our approach has no test-time cost, as we impose it only as a regularizer during training, rather than as an ever-present denoising layer.

Inspiration for our method traces back to the era of vision prior to the pervasive use of deep learning. It was once common to consider context as important [129], reason about object parts, co-occurrence, and interactions [130], and design graphical models to capture such relationships [131]. We refer to only a few sample papers as fully accounting for a decade of computer vision research is not possible here. In the following section, we open a pathway to pull such thinking about compositional scene priors into the modern era: simply learn, and employ, a deep model of label space.

5.3 Method

Figure 5.2 explains the intuition behind the regularization scheme outlined in Figure 5.1. Suppose we want to train a CNN to recognize and segment cats, but our limited training set consists only of tigers. It is conceivable that the CNN will learn an equivalence between black and orange striped texture and the cat category, as such association suffices to classify every pixel on a tiger. It thus overfits to the tiger subclass and fails when tested on images of house cats. This behavior could arise even if trained with detailed supervision of the form shown in Figure 5.2.

Yet, the semantic segmentation ground-truth suggests to any human that texture should not be the primary criterion. There are no stripes in the annotation. Over the entire training set, regions labeled as cat share a distinctive shape that deforms in a manner suggestive of unlabeled parts (e.g. head, body, tail, ear). The presence or absence of other objects in the scene may also provide contextual cues as to the chance of finding a cat. How can we force the CNN to notice this wealth of information during training?

We could consider treating the ground-truth label map as an image, and clustering local patches. The patch containing the skinny tail would fall in a different cluster than that containing the pointy ear. Adding the cluster identities as another semantic label, and requiring the CNN to predict them, would force the CNN to differentiate between the tail and ear by developing a representation of shape. This clustering approach is reminiscent of Poselets [132, 133].

Following this strategy, we would need to hand-craft another scheme for capturing object co-occurrence relations, perhaps by clustering descriptors spanning a larger spatial extent. We would prefer a general means of capturing features of the ground-truth annotations, and one not limited to a few hand-selected characteristics. Fortunately, deep networks are a suitable

general tool for building the kind of abstract feature hierarchy we desire.

| Layers | DenseNet-67 | DenseNet-121 |
|----------------------|--|--|
| Convolution | $\begin{bmatrix} 3 \times 3 \text{ conv, stride 2} \\ 3 \times 3 \text{ conv} \\ 3 \times 3 \text{ conv} \end{bmatrix} \times 1$ | $7 \times 7 \text{ conv, stride 2}$ |
| Pooling | $3 \times 3 \text{ max pool, stride 2}$ | |
| Dense Block (1) | $\begin{bmatrix} 1 \times 1 \text{ conv} \\ 3 \times 3 \text{ conv} \end{bmatrix} \times 6$ | $\begin{bmatrix} 1 \times 1 \text{ conv} \\ 3 \times 3 \text{ conv} \end{bmatrix} \times 6$ |
| Transition Layer (1) | $1 \times 1 \text{ conv}$ | |
| | $2 \times 2 \text{ average pool, stride 2}$ | |
| Dense Block (2) | $\begin{bmatrix} 1 \times 1 \text{ conv} \\ 3 \times 3 \text{ conv} \end{bmatrix} \times 8$ | $\begin{bmatrix} 1 \times 1 \text{ conv} \\ 3 \times 3 \text{ conv} \end{bmatrix} \times 12$ |
| Transition Layer (2) | $1 \times 1 \text{ conv}$ | |
| | $2 \times 2 \text{ average pool, stride 2}$ | |
| Dense Block (3) | $\begin{bmatrix} 1 \times 1 \text{ conv} \\ 3 \times 3 \text{ conv} \end{bmatrix} \times 8$ | $\begin{bmatrix} 1 \times 1 \text{ conv} \\ 3 \times 3 \text{ conv} \end{bmatrix} \times 24$ |
| Transition Layer (3) | $1 \times 1 \text{ conv}$ | |
| | $2 \times 2 \text{ average pool, stride 2}$ | |
| Dense Block (4) | $\begin{bmatrix} 1 \times 1 \text{ conv} \\ 3 \times 3 \text{ conv} \end{bmatrix} \times 8$ | $\begin{bmatrix} 1 \times 1 \text{ conv} \\ 3 \times 3 \text{ conv} \end{bmatrix} \times 16$ |

Figure 5.3: DenseNet architectural specifications.

5.3.1 Modeling labels

As shown in Figure 5.1, we train an autoencoder on the ground-truth label maps. This autoencoder consumes a semantic segmentation label map as input and attempts to reconstruct it as output. By being required to pass through a small bottleneck representation, the job of the autoencoder is nontrivial. It must compress the label map into the bottleneck representation.

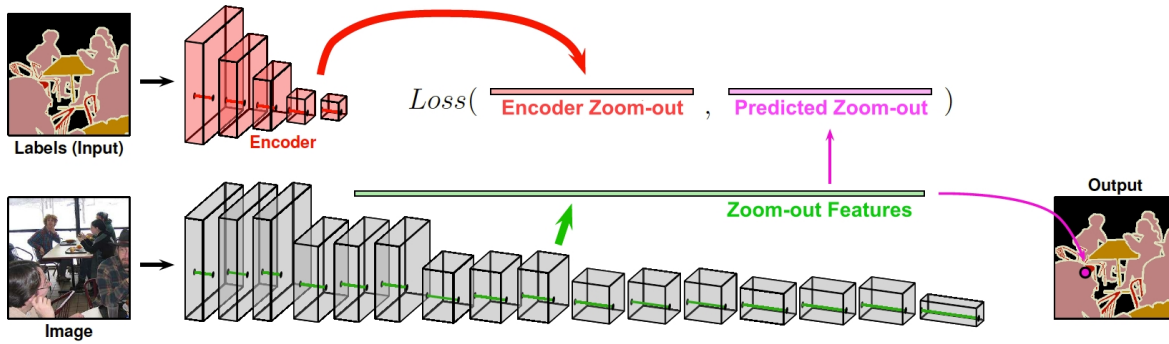


Figure 5.4: Alternative regularization scheme. Instead of predicting a representation to pass through the decoder, as in Figure 5.1, we can train with an auxiliary regression problem. We place a loss on directly predicting activations produced by the hidden layers of the encoder.

This compression constraint will (ideally) force the autoencoder to discover and implicitly encode parts and contextual relationships.

Ground-truth semantic segmentation label maps are simpler than real images, so this autoencoder need not have as high capacity as a network operating on natural images. We use a relatively simple autoencoder architecture, consisting of a mirrored encoder and decoder, with no skip connections. The encoder is a sequence of five 3×3 convolutional layers, with 2×2 max-pooling between them. The decoder uses 2x upsampling followed by 3×3 convolution. As a default, we set each layer to have 32 channels. We also experiment with some higher-capacity variants:

- conv1: 32-channels; conv2-5: 128 channels each
- conv1: 32; conv2-4: 128; conv5: 256 channels

These channel progressions are for the encoder; the decoder uses the same in reverse order. We refer to these three autoencoder variants by the number of channels in their respective bottleneck layers (32, 128, or 256).

5.3.2 Baseline CNN architectures

Convolutional neural networks for image classification gradually reduce spatial resolution with depth through a series of pooling layers [134, 114, 56, 57]. As the semantic segmentation task requires output at fine spatial resolution, some method of preserving or recovering spatial resolution must be introduced into the architecture. One option is to gradually re-expand spatial resolution via upsampling [135, 136]. Other approaches utilize some form of skip-connection to forward spatially resolved features from lower layers of the network to the final layer [43, 44, 137]. Dilated [67] or atrous convolutions [13] can also be mixed in. Alternatively, the basic CNN architecture can be reformulated in a multigrid setting [138].

Our goal is to examine the effects of a regularization scheme in isolation from major architectural design changes. Hence, we choose zoom-out CNN architectures as a primary basis for experimentation, as it is minimally separated from the established classification networks in design space. It also offers the added advantage of having readily available ImageNet pretrained models, easing experimentation in this setting.

We consider zoom-out variants of VGG-16 [114] and DenseNet [57]. Refer to Section 3.5 for architecture details. VGG-16 is widely used, while DenseNet [57] represents the latest high-performance evolution of ResNet [56]-like designs. We use 67-layer and 121-layer DenseNets with the architectural details specified in Figure 5.3. The 67-layer net uses a channel growth rate of 48, while the 121-layer network, the same as in [57], uses a growth rate of 32. We work with 256×256 input and output spatial resolutions in both CNNs and our label autoencoder.

5.3.3 Regularization via label modeling

As shown by the large gray arrow in Figure 5.1, we impose our regularizer by connecting a CNN (e.g., VGG or DenseNet) to the decoder portion of our learned label autoencoder. Importantly, the *decoder parameters are frozen during this training phase*. The CNN now has two tasks, each with an associated loss, to perform during training. As usual, it must predict semantic segmentation using zoom-out features. It must also predict the same semantic segmentation via an auxiliary path through the decoder. Backpropagation from losses along both paths influences CNN parameter updates. Though they participate in one of these paths, parameters internal to the decoder are never updated.

We connect VGG-16 or DenseNet to the decoder by predicting input for the decoder from the output of the penultimate CNN layer prior to global pooling. This is the second-to-last convolutional layer, and is selected because its spatial resolution matches that of the expected decoder input. The prediction itself is made via a new 1×1 convolutional layer, dedicated for that purpose.

If the label autoencoder learns useful abstractions, requiring the CNN to work through the decoder ensures that it learns to work with those abstractions. The zoom-out pathway allows the CNN to make direct predictions, while the decoder pathway ensures that the CNN has “good reasons” or a high-level abstract justification for its predictions.

Assuming autoencoder layers gradually buildup good abstractions, there exist alternative methods of connecting it as a regularizer. Figure 5.4 diagrams one such alternative. Here, we ask the CNN to directly predict the feature representation built by the label encoder. Encoder parameters are, of course, frozen here. An auxiliary layer attempts to predict the encoder zoom-out features from the CNN zoom-out features at the corresponding spatial location. The CNN must also still solve the original semantic segmentation task.

As Section 5.4 shows, this alternative scheme works well, but not quite as well as using the decoder pathway. Using the decoder is also appealing for more reasons than performance alone. Defining an auxiliary loss in terms of decoder semantic segmentation output is more interpretable than defining it in terms of mean square error (MSE) between two zoom-out features. Moreover, the decoder output is visually interpretable; we can see the semantic segmentation predicted by the CNN via the decoder.

5.4 Experiments

The PASCAL dataset [15] serves as our experimental testbed. We follow standard procedure for semantic segmentation, using the official PASCAL 2012 training set, and reporting performance in terms of mean intersection over union (mIoU) on the validation set (as validation ground-truth is publicly available). We explore both our decoder- and encoder-based regularization schemes in combination with multiple choices of base network, data augmentation, and pretraining. When applying the encoder as a regularizer, we task the CNN with predicting the concatenation of the encoder’s activations in its conv1 and conv3 layers.

5.4.1 Setup

All experiments are done in PyTorch [64], using the Adam [65] update rule when training networks. Models trained from scratch use a batch size of 12 and learning rate of 10^{-4} which after 80 epochs decreased to 10^{-5} for an additional 20 epochs. For the case of ImageNet pretrained models, we normalize zoom-out features such that they have zero mean and unit variance. We keep the deep network weights frozen and train the classifier for 10 epochs with learning rate of 10^{-4} . Then we decrease the learning rate to 10^{-5} and train end-to-end for

additional 40 epochs.

Data augmentation, when used, includes: a random horizontal flip and a crop of random size in the (0.08 to 1.0) of the original size and a random aspect ratio of 3/4 to 4/3 of the original aspect ratio, which is finally resized to create a 256×256 image. Pretrained models are based on the PyTorch torchvision library [66].

We use cross-entropy loss on auxiliary regularization branches, except where indicated by a superscript † in results tables. For these experiments, we use MSE loss.

| Architecture | Data-Aug? | Auxiliary Regularizer | mIoU |
|--------------------------|-----------------------|---|-------------|
| VGG-16 -zoom-out | no | none | 37.3 |
| | no | Encoder (conv1 & conv3) [†] | 41.1 |
| | no | Decoder (32 channel)[†] | 42.4 |
| | yes | none | 55.2 |
| | yes | Decoder (128 channel) | 57.1 |
| VGG-16-FCN8s | yes | none | 51.5 |
| | yes | Decoder (128 channel) | 54.1 |
| DenseNet-67 -zoom-out | no | none | 40.5 |
| | no | Encoder (conv1 & conv3) [†] | 44.0 |
| | no | Decoder (32 channel)[†] | 45.2 |
| | no | Decoder (128 channel) | 42.5 |
| | yes | none | 58.8 |
| | yes | Decoder (32 channel) | 59.4 |
| | yes | Decoder (128 channel) | 60.6 |
| yes | Decoder (256 channel) | 59.8 | |

Table 5.1: PASCAL mIoU without ImageNet pretraining. In each experimental setting (choice of architecture, and presence or absence of data augmentation), training with any of our regularizers improves performance over the baseline (shown in gray).

5.4.2 Semantic Segmentation Results

Tables 5.1, 5.3, and 5.4 summarize the performance benefits of training with our regularizer. In the absence of pretraining or data augmentation, we boost performance of both VGG-16

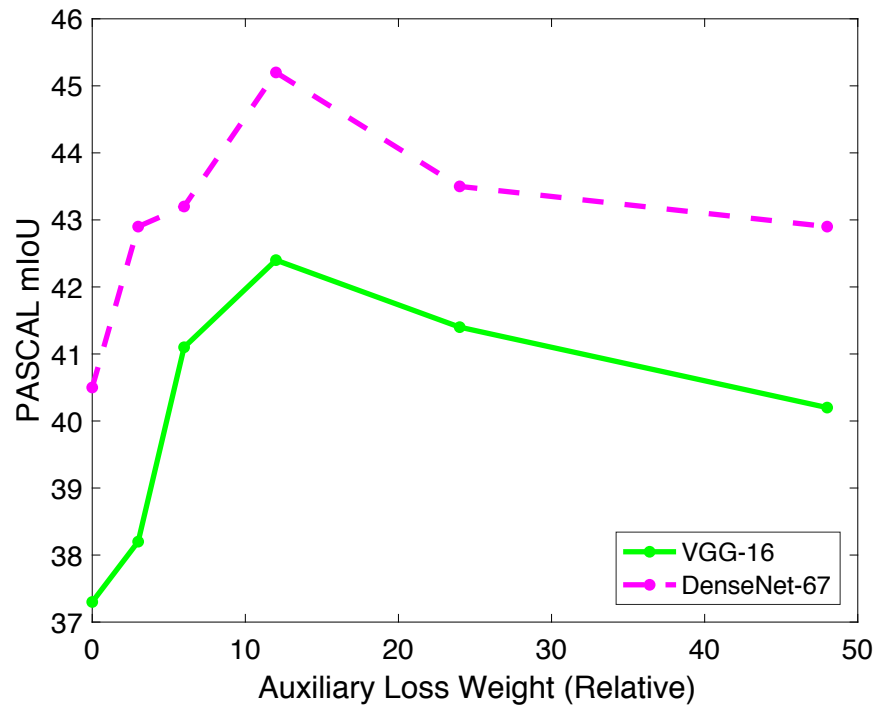


Figure 5.5: Auxiliary loss weighting. We plot validation performance as a function of the relative weight of the losses on the auxiliary vs primary output branches when training with the setup in Figure 5.1. Performance is mIoU on PASCAL, without ImageNet pretraining or data augmentation. Note that any nonzero weight on the auxiliary loss (any regularization) improves over the baseline.

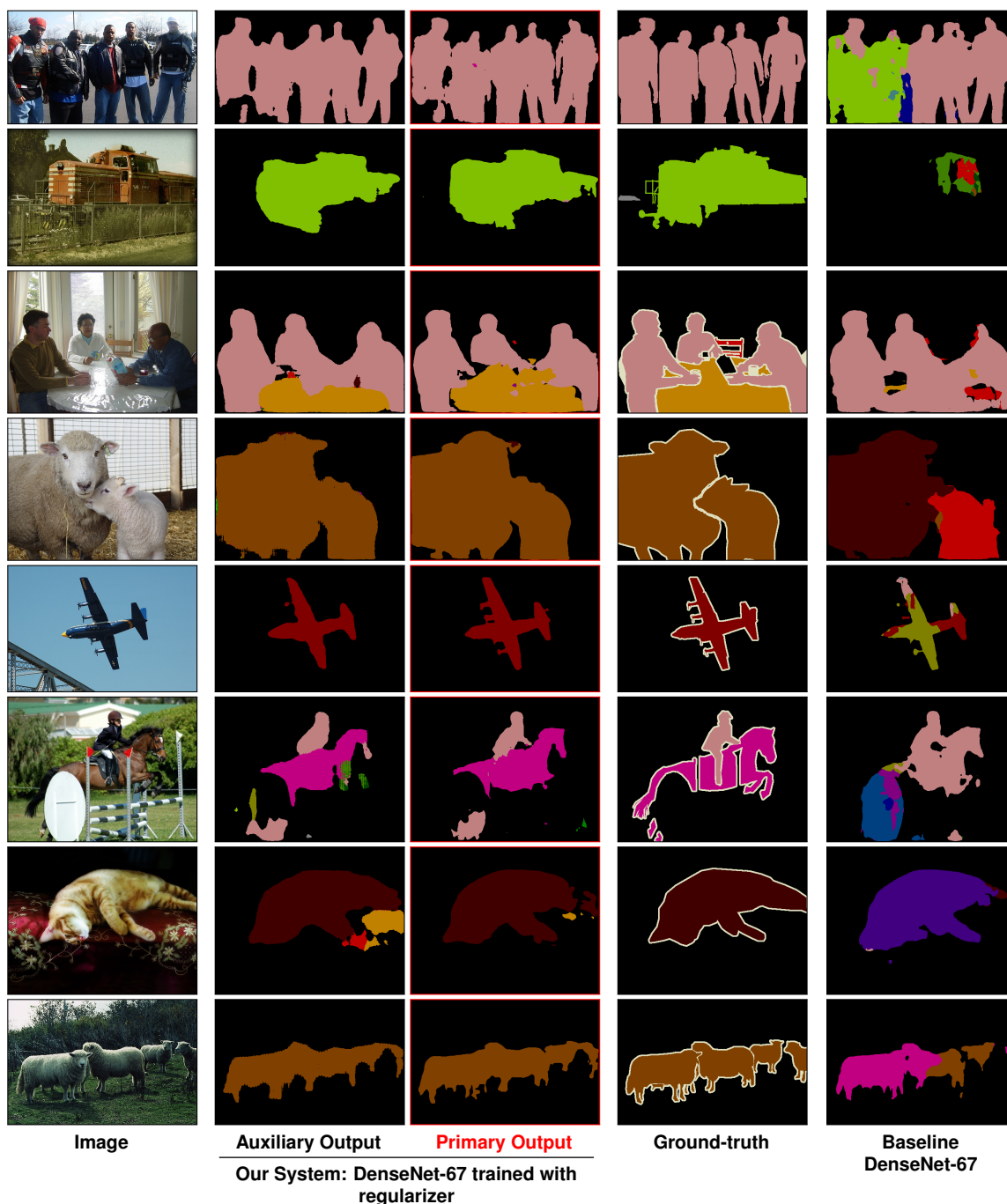


Figure 5.6: Semantic segmentation results on PASCAL. We show the output of a baseline 67-layer zoom-out DenseNet (rightmost column) compared to that of the same architecture trained with our auxiliary decoder branch as a regularizer (middle columns). All examples are from the validation set. While we can discard the auxiliary branch after training, we include its output here to display the decoder’s operation. Our network provides high-level signals to the decoder which, in turn, produces reasonable segmentations. To best illustrate the effect of regularization, all results shown are for networks trained from scratch, without ImageNet pretraining or data augmentation. This corresponds to the 40.5 to 45.2 jump in mIoU reported in Table 5.1, between the baseline and our primary output.

| Architecture | Data-Aug | Auxiliary Regularizer | mIoU |
|--------------------------|----------|------------------------------|-------------|
| DenseNet-67 -zoom-out | yes | none | 58.8 |
| | yes | Decoder (128 channel) | 60.6 |
| | yes | Unfrozen Decoder | 60.2 |
| | yes | Random Init. Decoder | 58.8 |

Table 5.2: Ablation study. PASCAL mIoU deteriorates if the decoder parameters are not held fixed while training the main CNN.

| Architecture | Data-Aug? | Auxiliary Regularizer | mIoU |
|---------------------------|-----------|------------------------------|-------------|
| VGG-16 -zoom-out | no | none | 67.1 |
| | no | Decoder (32 channel) | 68.8 |
| DenseNet-121 -zoom-out | yes | none | 71.6 |
| | yes | Decoder (128 channel) | 71.9 |
| ResNet-101 -PSPNet | yes | none | 75.4 |
| | yes | Decoder (128 channel) | 75.9 |

Table 5.3: PASCAL mIoU with ImageNet pretraining.

| Architecture | Data-Aug | Auxiliary Regularizer | mIoU |
|--------------------------|----------|------------------------------|-------------|
| DenseNet-67 -zoom-out | yes | none | 72.3 |
| | yes | Decoder (128 channel) | 73.6 |

Table 5.4: PASCAL mIoU with COCO pretraining.

and DenseNet-67 by 5.1 and 4.7 mIoU, respectively, which is more than a 10% relative boost. Regularization with our decoder still improves mIoU (from 58.8 to 60.6) of DenseNet-67 trained with data augmentation. To further show the robustness of our regularization scheme to the choice of architecture, we also experiment with an FCN [43] version of VGG-16, as included in Table 5.1.

Table 5.2 demonstrates the necessity of our two-phase training procedure. If we unfreeze the decoder and update its parameters in the second training phase, test performance of the primary output deteriorates. Likewise, if we skip the first phase, and train from scratch with an

unfrozen, randomly initialized decoder, the accuracy gain disappears. Thus, the regularization effect is due to a transfer of information from the learned label model, rather than stemming from an architectural design of dual output pathways.

Table 5.3 shows that our regularization scheme synergizes with ImageNet pretraining. It improves VGG-16 performance, and even provides some benefit to a very deep 121-layer DenseNet pretrained on ImageNet, while using data augmentation. A baseline 71.6 mIoU for DenseNet-121 is near state-of-the-art for networks that do not employ additional tricks (e.g. custom pooling layers [14], use of multiscale, or post-processing with CRFs [13]). Our improvement to 71.9 mIoU may be nontrivial. Expanding trials in combination with pretraining, our regularizer improves results when pretraining on COCO, as shown in Table 5.4.

We also combine our regularizer with the latest network design for semantic segmentation: dilated ResNet augmented with the pyramid pooling module of PSPNet [14]. We used the output of the pyramid pooling layer to predict input for the decoder and semantic segmentation. Table 5.3 shows gain over the corresponding PSPNet baseline.

Beyond autoencoder architecture choice, application of our regularizer involves one free parameter: the relative weight of the auxiliary branch loss with respect to the primary loss. Figure 5.5 shows how performance of the trained network varies with this parameter, when using our 32-channel bottleneck layer decoder with MSE loss on the auxiliary branch. Weighting is important, but the optimal balance appears consistent when changing architecture from VGG-16 to DenseNet-67.

We have also run similar experiments with cross-entropy loss on the auxiliary branch with the weight parameter in $[0, 6]$. Here, the weight parameter range is changed due to the difference in the dynamic range of values between MSE loss and cross-entropy loss. Behaving similarly to Figure 5.5, relative weighting of 0.5 achieves the highest accuracy. We use this

weight value across all of the experiments using our decoder with 128-channel bottleneck layer. While the regularizer always provides a benefit, placing a proper relative weight on the auxiliary loss is important.

Figure 5.6 visualizes the impact of training with our learned label decoder as a regularizer. Most notably, the network trained with regularization appears to correct some global or large-scale semantic errors in comparison to the baseline. Contrast such behavior to CRF-based post-processing, which typically achieves impact through fixing local mistakes. Also notable is that our auxiliary output itself is quite reasonable. This suggests that the autoencoder training phase is successful in creating encoders and decoders that model label structure.

5.4.3 Label Model Introspection

To further investigate what the autoencoder learns, we consider using the bottleneck representation produced by the encoder as defining features by which we can perform queries in label space. Specifically, we pick a region of a training image label and represent that region with features extracted from bottleneck layer. As the bottleneck layer is low-resolution, we are selecting features at coarse, but corresponding spatial location.

Next, we perform nearest neighbor search over all regions in the validation set and find the two closest regions to the query region. Figure 5.7 shows the results of this experiment. Returned regions not only have the same object class types as the query regions, but also share similar shapes to that of the query. This reveals that our label autoencoder has learned to capture object shape characteristics.

We also repeat this experiment, except with queries starting from images. Here the bottleneck representation is produced by a CNN, which was trained with both zoom-out and decoder prediction pathways; the latter yields the required features. As shown in the top right



Figure 5.7: Finding regions with similar representations. For each **query** image (green border) and region (green rectangle), the next two images to the right are those in the validation set containing the nearest regions to the query region. All query images are from the training set. For examples on red background, search is conducted not by looking at images, but via matching features produced by the **encoder** run on ground-truth label maps. The bottom-right shows failure cases, such as matching a cat’s arm to the car rear door. For examples on gray background, our **DenseNet-67 zoom-out CNN** is used to predict the label space search representations from images.

of Figure 5.7, returned regions have similar context and shape to the query.

5.5 Monocular depth and semantic segmentation

Monocular depth estimation is a crucial step towards scene geometry understanding from 2D images. The goal in monocular depth estimation is to predict the depth value of each pixel, given a single RGB image as input. In many practical applications such as autonomous driving or robotic surgery we require both semantic segmentation and depth predictions. Therefore, it is important to investigate how correlated these two tasks are. In this section first we explore how well we can predict depth maps directly from semantic segmentation maps, without using RGB images. We will show that it is possible to predict depth maps directly from semantic segmentation maps and surprisingly even with better accuracy comparing to predicting depth from RGB images. This indicates a strong correlation between these two tasks. Based on this observation, we propose an architecture in which we use segmentation as an intermediate representation for depth estimation.

Datasets like NYUv2 [139] have orders of magnitude more depth data than annotated segmentation maps. With the proposed architecture, we show that we are able to utilize additional depth data to gain noticeable boost in segmentation accuracy while maintaining depth prediction accuracy.

5.5.1 Semantic segmentation to depth

Given a semantic segmentation mask we want to estimate depth values for all pixels. There are many clues such as relative objects' sizes and occlusion boundaries that can be leveraged. Figure 5.8 shows an input semantic segmentation map and its corresponding depth map.

Previous and recent work on jointly predicting semantic segmentation and depth [140, 141, 142, 143] have shown that these two tasks can benefit from joint training. In contrast, we predict depth maps from semantic segmentation maps rather than predicting them jointly from RGB images. In [144] they predict depth maps from predicted segmentation maps. However, we predict depth maps from ground truth segmentation maps to evaluate how well we can predict depth maps from semantic segmentation maps. All of these methods assume that they have access to both ground truth semantic segmentation and depth for all of their training images. In contrast, we don't have such an assumption. In Section 5.5.2 we describe how we deal with unequal number of segmentation annotations and depth images.

We evaluate our models on NYUv2 dataset [139]. NYUv2 is a widely used dataset for monocular depth estimation in indoor environments. It contains 464 indoor scenes collected with a Kinect RGBD camera. To form our training set, we sub-sample 60,000 RGB images with their corresponding depth maps uniformly from the raw part of the dataset. The labeled part of dataset consists of 1449 RGB-D images provided with semantic segmentation annotations. We follow the standard evaluation approach and use 40 categories for semantic segmentation task.

For the following experiments, we train our models on the labeled part of the NYUv2. We follow the standard split of 795 training images and 654 test images. When we use segmentation as input, we have one binary mask channel for each object class. We use ResNet-50 with dilated convolution and apply pyramid pooling layer [14] to the features of last fully convolutional layer of ResNet. For further details regarding architecture design refer to Section 3.5. Training images are resized to 256×336 . For data augmentation we use random horizontal flip. We use the Adam [65] update rule with learning rate of 10^{-4} for 60 epochs.

In order to evaluate our depth estimations we report our results based on the commonly

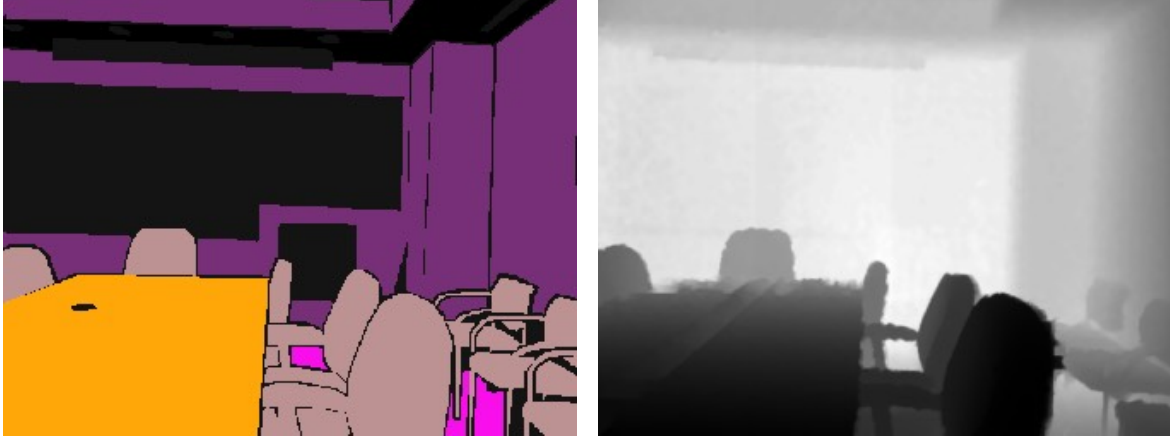


Figure 5.8: Left image shows semantic segmentation map and the right image is its corresponding depth map. Chairs that are occluded by table are farther from camera than the table. Also relative size of the chairs hints at their distance from the camera.

used measures:

- Root mean squared error (linear): $RMSE = \sqrt{\frac{1}{N} \sum_{i,j} |y_{ij} - \hat{y}_{ij}|^2}$
- Root mean squared error (log): $RMSE_{log} = \sqrt{\frac{1}{N} \sum_{i,j} |\log(y_{ij}) - \log(\hat{y}_{ij})|^2}$
- Squared relative difference: $srel = \frac{1}{N} \sum_{i,j} |y_{ij} - \hat{y}_{ij}|^2 / \hat{y}_{ij}$
- Absolute relative difference: $rel = \frac{1}{N} \sum_{i,j} |y_{ij} - \hat{y}_{ij}| / \hat{y}_{ij}$
- Thresholded accuracy: Percentage of predicted depth y such that $\max(y_i / \hat{y}_i, \hat{y}_i / y_i) < threshold$

Where \hat{y} is the predicted depth map and y is the ground truth depth map. Total number of pixels is N .

| Input | RMSE (lin.) | RMSE(log) | Abs Rel | Sqr Rel | $\delta < 1.25$ | $\delta < 1.25^2$ | $\delta < 1.25^3$ |
|---------|-------------|-----------|---------|---------|-----------------|-------------------|-------------------|
| RGB | 0.628 | 0.227 | 0.1967 | 0.1749 | 0.718 | 0.918 | 0.976 |
| Seg | 0.548 | 0.192 | 0.1557 | 0.1191 | 0.785 | 0.953 | 0.989 |
| Seg+RGB | 0.524 | 0.182 | 0.1446 | 0.1052 | 0.807 | 0.959 | 0.991 |

Table 5.5: Depth prediction results of models with different inputs on NYUv2 test set.

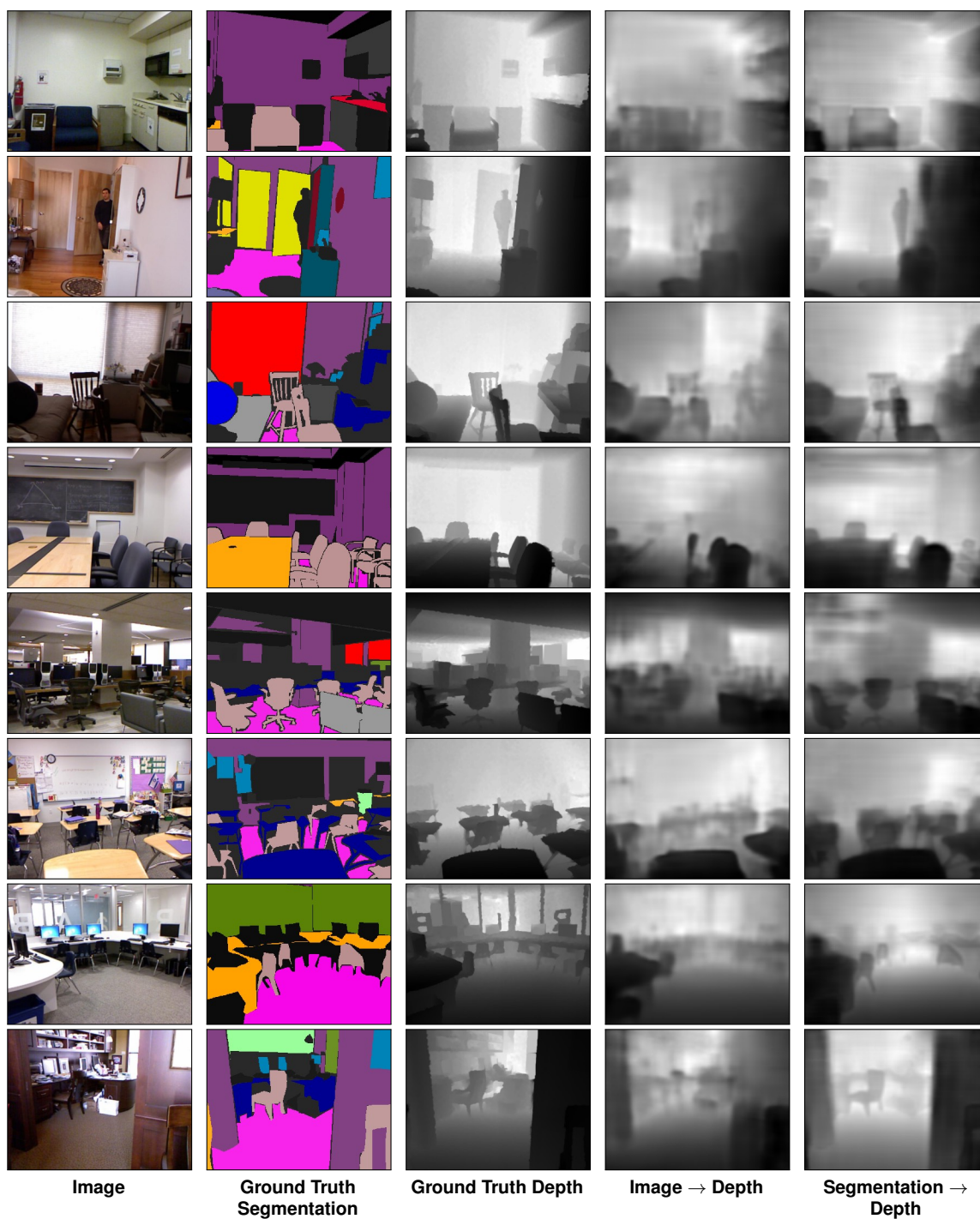


Figure 5.9: Depth predictions results on NYUv2. We show not only it is possible to predict depth maps from segmentation maps, but also these predicted depth maps are considerably sharper and more accurate than the predictions from RGB images.

Table 5.5 shows results of predicting depth maps from RGB and semantic segmentation inputs. Surprisingly, we get lower errors when using semantic segmentation as input. Since segmentation maps provide accurate object boundaries, depth predictions from segmentation maps in Figure 5.9 have sharper and more accurate boundaries around objects, while depth predictions from RGB images in some cases miss large part of objects. This observation indicates not only there is a strong correlation between semantic segmentation and monocular depth estimation, but also segmentation can be used as an effective intermediate representation for monocular depth estimation. The last row of Table 5.5 shows results further improve when segmentation masks are concatenated with RGB channels and given to the input of the model.

5.5.2 Unified architecture for predicting segmentation and depth

Results in Table 5.5 inspired us to use segmentation as an intermediate representation in our unified architecture for jointly predicting depth and segmentation. However, we used ground truth segmentation as an input to our model. Here we want to have a more practical approach and use predicted segmentation as an input. We break our depth and segmentation prediction model into two parts. The first part of the model takes an image as an input and predicts depth and segmentation. The second part of the model takes image, predicted depth and predicted segmentation as inputs and predicts depth and segmentation. In datasets like NYUv2 which offer both segmentation and depth ground truths, it is often the case that we don't have the same amount of annotations for both tasks. For example our training set has 60,000 images with depth ground truth but only 1449 images with both segmentation and depth ground truths. Given our unified model for depth and segmentation predictions the question is how do we deal with images where we do have depth maps but we don't have segmentation annotations. If we simply train the model on all training data, there are many training batches where we have no semantic segmentation supervision. This causes the model to focus less on semantic

segmentation and give a higher weight to depth estimation. Ideally we want to benefit both tasks from joint training. To deal with this issue, our solution is simple: we make sure in each training batch we have at least one image for which both segmentation and depth maps are available. For the images with only depth ground truth and no segmentation annotations, we freeze segmentation head and only backpropagate through the depth head and the shared model.

5.5.2.1 Architecture details and experimental results

We use zoom-out DenseNet-121 for the first part of the model. We set zoom-out spatial feature size to 1/4 of input image. For further details of zoom-out DenseNet architecture design refer to Section 3.5. Once zoom-out features are computed we pass them through segmentation head and depth head. Each head consists of 3-layer CNN with 1×1 convolutions with 1000 hidden units in each layer. First part takes RGB image as input and predicts depth and semantic segmentation. Similarly to first part we use zoom-out DenseNet-121 for the second part. However, second part takes the output of the first part which are predicted depth and segmentation plus RGB image and predicts depth and segmentation. For each part in our unified model we have two loss functions one for depth head and one for segmentation head. In total we have 4 losses. We use L1 loss which measures mean absolute error between the predicted depth and the ground truth depth. We use cross-entropy loss for segmentation. Final loss is weighted sum of 4 loss terms. The average loss value is computed over couple of epochs for each of the loss terms. Then loss terms are weighted such that each loss term contributes equally to the final loss. We train our models for 40 epochs on both raw and labeled parts of the training set with learning rate of 10^{-4} using Adam update rule. Then we reduce the learning rate to 10^{-5} and train for 20 epochs only on the labeled part of the training set.

Two-part architecture design allows us to predict depth and segmentation in unified model. Therefore, we utilize benefits of jointly training depth and segmentation. These benefits include a unified model with shared parameters between the two tasks and higher prediction accuracies comparing to having a separate model for each task. Furthermore, results in Table 5.6 shows that significant boost in segmentation accuracy can be achieved from the same amount of segmentation annotations, but extra training images with just depth ground truth. Table 5.6 shows the benefit of two-part model over the baseline.

Baseline and two-part models The difference between baseline model and two-part model is where we provide supervision. In two-part model we provide supervision for depth and segmentation predictions both at the end of the first part of the model and at the end of the second part of the model. The baseline model has the same architecture, but it has not been trained with extra supervision for the first step. Basically it is a single step model with the loss function at the very end of the network.

Baseline without segmentation/depth loss Same as baseline model except we only estimate depth maps and ignore semantic segmentation task or vice versa.

2x segmentation loss In this setting we use the baseline model except segmentation cross entropy loss contributed 2 times more than depth L1 loss to the final loss. This experiment is done to make sure that the segmentation gain achieved by two-part model is due to model design and not the weight of segmentation loss with respect to the depth loss.

Results in Table 5.6 show: a) both segmentation and depth predictions can benefit from joint training b) segmentation can gain significant boost from extra depth ground truth data.

| Model | Depth RMSE (lin.) | Seg mIoU |
|------------------------|-------------------|----------|
| Baseline | 0.45 | 38 |
| Baseline no seg loss | 0.49 | - |
| Baseline no depth loss | - | 36 |
| 2x seg loss | 0.46 | 38 |
| two-part model | 0.44 | 41 |

Table 5.6: Depth and semantic segmentation results of baseline and our two-part models based on zoom-out DenseNet-121 on NYUv2 test set.

5.6 Summary

Our novel label embedding-based regularization method, when applied to training deep networks for semantic segmentation, consistently improves their generalization performance. The intuition behind our work, that additional supervisory signal can be squeezed from highly detailed annotation, is supported by the types of errors this regularizer corrects, as well as our efforts at introspection into our learned label model.

We showed that it is possible to predict depth maps directly from semantic segmentation maps and proposed a two-part architecture for joint prediction of depth and semantic segmentation which uses semantic segmentation as an intermediate representation for depth estimation. Our two-part architecture improves results over the baselines for both depth and semantic segmentation predictions.

Chapter 6

Conclusion

In this thesis, we presented zoom-out architecture for learning and extracting rich representations for structured visual prediction tasks. Our effective and simple architecture can turn any modern CNN backbone such as such as DenseNet, ResNet and NASNet into near state-of-the-art image labeling model, without the need to use complicated methods both in network design and training methodology.

We proposed a modified zoom-out architecture tailored for classification tasks, to drive a weakly supervised process that automatically labels a sparse, diverse training set of points likely to belong to classes of interest. We obtained competitive results on the VOC 2012 segmentation benchmark by training our model on the set of automatically generated sparse labels.

Our novel label embedded-based regularization method improves generalization performance of image labeling networks. Our results indicate that one should now reevaluate the relative utility of different forms of annotation; our method makes detailed labeling more useful than previously believed. This observation may be especially important for applications

of computer vision, such as self-driving cars, that demand detailed scene understanding, and for which large-scale dataset construction is essential. Since they have access to large-scale detailed ground-truth labels, they can utilize our label embedding-based regularization technique to further improve the generalization performance of their deep models.

The success of our two-part model for joint training of segmentation and depth estimation suggests that when there is a strong correlation between two tasks, using the output of one task as an intermediate representation for the other task can lead to an improved performance in both tasks. A future work in this direction would be to extend this approach for more than two tasks, and have a unified architecture for multi-task learning.

Bibliography

- [1] Pushmeet Kohli, L'ubor Ladicky, and Philip H. S. Torr. Robust higher order potentials for enforcing label consistency. In *CVPR*, 2008. ISBN 978-1-4244-2242-5. doi: <http://doi.ieeecomputersociety.org/10.1109/CVPR.2008.4587417>.
- [2] J.D.J. Shotton, J. Winn, C. Rother, and A. Criminisi. Textonboost for image understanding: Multi-class object recognition and segmentation by jointly modeling texture, layout, and context. *IJCV*, 81(1), 2009.
- [3] Philipp Krähenbühl and Vladlen Koltun. Efficient inference in fully connected crfs with gaussian edge potentials. *Adv. Neural Inf. Process. Syst*, 2011.
- [4] L. Ladický, C. Russell, P. Kohli, and P. H. S. Torr. Associative hierarchical CRFs for object class image segmentation. *ICCV*, 2009.
- [5] Victor Lempitsky, Andrea Vedaldi, and Andrew Zisserman. Pylon model for semantic segmentation. In *NIPS*, pages 1485–1493, 2011.
- [6] Payman Yadollahpour, Dhruv Batra, and Gregory Shakhnarovich. Discriminative re-ranking of diverse segmentations. In *CVPR*, 2013.
- [7] Dhruv Batra, Payman Yadollahpour, Abner Guzman-Rivera, and Greg Shakhnarovich. Diverse M-Best Solutions in Markov Random Fields. In *ECCV*, 2012.

- [8] Xavier Boix, Josep M. Gonfaus, Joost van de Weijer, Andrew D. Bagdanov, Joan Serrat Gual, and Jordi González. Harmony potentials - fusing global and local scale for semantic image segmentation. *IJCV*, 96(1):83–102, 2012.
- [9] Mohammadreza Mostajabi and Iman Gholampour. A robust multilevel segment description for multi-class object recognition. *Machine Vision and Applications*, 2014.
- [10] Mohammadreza Mostajabi, Nicholas I. Kolkin, and Gregory Shakhnarovich. Diverse sampling for self-supervised learning of semantic segmentation. *arXiv preprint*, 2016.
- [11] Jia Deng, Wei Dong, Richard Socher, Li-Jia Li, Kai Li, and Li Fei-Fei. ImageNet: A large-scale hierarchical image database. *CVPR*, 2009.
- [12] Ziwei Liu, Xiao Xiao Li, Ping Luo, Chen Change Loy, and Xiaoou Tang. Semantic image segmentation via deep parsing network. *ICCV*, 2015.
- [13] Liang-Chieh Chen, George Papandreou, Iasonas Kokkinos, Kevin Murphy, and Alan L Yuille. Deeplab: Semantic image segmentation with deep convolutional nets, atrous convolution, and fully connected CRFs. In *arXiv:1606.00915* Chen et al. [68].
- [14] Hengshuang Zhao, Jianping Shi, Xiaojuan Qi, Xiaogang Wang, and Jiaya Jia. Pyramid scene parsing network. *CVPR*, 2017.
- [15] Mark Everingham, Luc van Gool, Chris Williams, John Winn, and Andrew Zisserman. The PASCAL Visual Object Classes (VOC) challenge. *IJCV*, 2010.
- [16] Tsung-Yi Lin, Michael Maire, Serge Belongie, James Hays, Pietro Perona, Deva Ramanan, Piotr Dollár, and C. Lawrence Zitnick. Microsoft COCO: Common objects in context. *ECCV*, 2014.
- [17] Mohammadreza Mostajabi, Michael Maire, and Gregory Shakhnarovich. Regularizing

- deep networks by modeling and predicting label structure. In *The IEEE Conference on Computer Vision and Pattern Recognition (CVPR)*, June 2018.
- [18] P. Arbelaez, M. Maire, C. Fowlkes, and J. Malik. Contour detection and hierarchical image segmentation. *IEEE Transactions on Pattern Analysis and Machine Intelligence*, 33(5):898–916, May 2011.
- [19] D. Martin, C. Fowlkes, D. Tal, and J. Malik. A database of human segmented natural images and its application to evaluating segmentation algorithms and measuring ecological statistics. In *Proc. 8th Int’l Conf. Computer Vision*, volume 2, pages 416–423, July 2001.
- [20] Radhakrishna Achanta, Appu Shaji, Kevin Smith, Aurelien Lucchi, Pascal Fua, and Sabine Susstrunk. Slic superpixels compared to state-of-the-art superpixel methods. *IEEE TPAMI*, 34(11), 2012.
- [21] D. Comaniciu and P. Meer. Mean shift: a robust approach toward feature space analysis. *PAMI*, 24(5):603–619, 2002.
- [22] J. Carreira and C. Sminchisescu. Constrained parametric min-cuts for automatic object segmentation. In *CVPR*, 2010. doi: 10.1109/CVPR.2010.5540063.
- [23] Jianbo Shi and Jitendra Malik. Normalized cuts and image segmentation. *PAMI*, 22(8): 888–905, 2000. ISSN 0162-8828. doi: <http://doi.ieeecomputersociety.org/10.1109/34.868688>.
- [24] W. Tu, M. Liu, V. Jampani, D. Sun, S. Chien, M. Yang, and J. Kautz. Learning superpixels with segmentation-aware affinity loss. In *2018 IEEE/CVF Conference on Computer Vision and Pattern Recognition*, pages 568–576, June 2018. doi: 10.1109/CVPR.2018.00066.

- [25] Xide Xia and Brian Kulis. W-net: A deep model for fully unsupervised image segmentation. *arXiv preprint*, abs/1711.08506, 2017. URL .
- [26] Alexander Kirillov, Kaiming He, Ross B. Girshick, Carsten Rother, and Piotr Dollár. Panoptic segmentation. *arXiv preprint*, abs/1801.00868, 2018.
- [27] Joao Carreira and Cristian Sminchisescu. Cpmc: Automatic object segmentation using constrained parametric min-cuts. *Pattern Analysis and Machine Intelligence, IEEE Transactions on*, 34(7), 2012.
- [28] J. R. R. Uijlings, K. E. A. van de Sande, T. Gevers, and A. W. M. Smeulders. Selective search for object recognition. *International Journal of Computer Vision*, 104(2), 2013.
- [29] P. Arbelaez, B. Hariharan, Chunhui Gu, S. Gupta, L. Bourdev, and J. Malik. Semantic segmentation using regions and parts. In *CVPR*, 2012.
- [30] João Carreira, Rui Caseiro, Jorge Batista, and Cristian Sminchisescu. Semantic segmentation with second-order pooling. In *Computer Vision–ECCV 2012*, pages 430–443. Springer, 2012.
- [31] Adrian Ion, Joao Carreira, and Cristian Sminchisescu. Probabilistic joint image segmentation and labeling. In *NIPS*, pages 1827–1835, 2011.
- [32] João Carreira, Fuxin Li, and Cristian Sminchisescu. Object recognition by sequential figure-ground ranking. *IJCV*, 98(3):243–262, 2012.
- [33] Z. Li, E. Gavves, K. E. A. van de Sande, C. G. M. Snoek, and A. W. M. Smeulders. Codemaps segment, classify and search objects locally. In *ICCV*, 2013.
- [34] Bharath Hariharan, Pablo Arbeláez, Ross Girshick, and Jitendra Malik. Simultaneous detection and segmentation. In *Computer Vision–ECCV 2014*, 2014.

- [35] Michael Cogswell, Xiao Lin, Senthil Purushwalkam, and Dhruv Batra. Combining the best of graphical models and convnets for semantic segmentation. *arXiv preprint*, abs/1412.4313, 2014. URL .
- [36] Brian Fulkerson, Andrea Vedaldi, and Stefano Soatto. Class segmentation and object localization with superpixel neighborhoods. In *CVPR*, 2009.
- [37] Joseph J Lim, Pablo Arbeláez, Chunhui Gu, and Jitendra Malik. Context by region ancestry. In *ICCV*, 2009.
- [38] Aurélien Lucchi, Yunpeng Li, Xavier Boix, Kevin Smith, and Pascal Fua. Are spatial and global constraints really necessary for segmentation? In *ICCV*, 2011.
- [39] Clément Farabet, Camille Couprie, Laurent Najman, and Yann LeCun. Learning hierarchical features for scene labeling. *IEEE TPAMI*, 35(8), 2013.
- [40] P. H. O. Pinheiro and R. Collobert. Recurrent convolutional neural networks for scene labeling. In *ICML*, 2014.
- [41] Richard Socher, Cliff C. Lin, Andrew Y. Ng, and Christopher D. Manning. Parsing Natural Scenes and Natural Language with Recursive Neural Networks. In *ICML*, 2011.
- [42] Gary B Huang and Viren Jain. Deep and wide multiscale recursive networks for robust image labeling. *arXiv preprint arXiv:1310.0354*, 2013.
- [43] Jonathan Long, Evan Shelhamer, and Trevor Darrell. Fully convolutional networks for semantic segmentation. *CVPR*, 2015.
- [44] Bharath Hariharan, Pablo Arbelaez, Ross Girshick, and Jitendra Malik. Hypercolumns for object segmentation and fine-grained localization. *CVPR*, 2015.

- [45] Radhakrishna Achanta, Appu Shaji, Kevin Smith, Aurelien Lucchi, Pascal Fua, and Sabine S¸sstrunk. Slic superpixels compared to state-of-the-art superpixel methods. *IEEE TPAMI*, 2012.
- [46] Mark Everingham, S.M.Ali Eslami, Luc Van Gool, ChristopherK.I. Williams, John Winn, and Andrew Zisserman. The pascal visual object classes challenge: A retrospective. *International Journal of Computer Vision*, 2014.
- [47] Olga Russakovsky, Jia Deng, Hao Su, Jonathan Krause, Sanjeev Satheesh, Sean Ma, Zhiheng Huang, Andrej Karpathy, Aditya Khosla, Michael Bernstein, et al. Imagenet large scale visual recognition challenge. *arXiv:1409.0575*, 2014.
- [48] Daniel Tarlow and Richard S Zemel. Structured output learning with high order loss functions. In *AISTATS*, 2012.
- [49] Daniel Kuettel, Matthieu Guillaumin, and Vittorio Ferrari. Segmentation propagation in imagenet. In *ECCV*, 2012.
- [50] Bharath Hariharan, Pablo Arbelaez, Lubomir Bourdev, Subhransu Maji, and Jitendra Malik. Semantic contours from inverse detectors. In *International Conference on Computer Vision (ICCV)*, 2011.
- [51] Jamie Shotton, John Winn, Carsten Rother, and Antonio Criminisi. Textonboost: Joint appearance, shape and context modeling for multi-class object recognition and segmentation. In *ECCV*, 2006. URL .
- [52] David G. Lowe. Distinctive image features from scale-invariant keypoints. *Int. J. Comput. Vision*, 60(2):91–110, November 2004. ISSN 0920-5691. doi: 10.1023/B:VISI.0000029664.99615.94.
- [53] K. Chatfield, K. Simonyan, A. Vedaldi, and A. Zisserman. Return of the devil in the details: Delving deep into convolutional nets. In *BMVC*, 2014.

- [54] K. Simonyan and A. Zisserman. Very deep convolutional networks for large-scale image recognition. *arXiv preprint* , 2014.
- [55] R. Girshick, J. Donohue, T. Darrell, and J. Malik. Rich feature hierarchies for accurate object detection and semantic segmentation. *arXiv preprint* , 2014.
- [56] Kaiming He, Xiangyu Zhang, Shaoqing Ren, and Jian Sun. Deep residual learning for image recognition. *CVPR*, 2016.
- [57] Gao Huang, Zhuang Liu, Laurens van der Maaten, and Kilian Q. Weinberger. Densely connected convolutional networks. *CVPR*, 2017.
- [58] Barret Zoph, Vijay Vasudevan, Jonathon Shlens, and Quoc V. Le. Learning transferable architectures for scalable image recognition. *arXiv preprint*, abs/1707.07012, 2017.
- [59] Yangqing Jia, Evan Shelhamer, Jeff Donahue, Sergey Karayev, Jonathan Long, Ross Girshick, Sergio Guadarrama, and Trevor Darrell. Caffe: Convolutional architecture for fast feature embedding. *arXiv preprint* , 2014.
- [60] N. Srivastava, G. Hinton, A. Krizhevsky, I. Sutskever, and R. Salakhutdinov. Dropout: A simple way to prevent neural networks from overfitting. *Journal of Machine Learning Research*, 15, 2014.
- [61] J. Long, E. Shelhamer, and T. Darrell. Fully convolutional networks for semantic segmentation. *arXiv preprint* , 2015.
- [62] B. Hariharan, P. Aberl ez an R. Girshick, and J. Malik. Hypercolumns for object segmentation and fine-grained localization. *arXiv preprint* , 2015.
- [63] Alex Krizhevsky, Ilya Sutskever, and Geoffrey E Hinton. Imagenet classification with deep convolutional neural networks. In *NIPS*, 2012.
- [64] PyTorch. <https://github.com/pytorch/pytorch>.

- [65] Diederik P. Kingma and Jimmy Ba. Adam: A method for stochastic optimization. *ICLR*, 2015.
- [66] PyTorch torchvision. <https://github.com/pytorch/vision>.
- [67] Fisher Yu and Vladlen Koltun. Multi-scale context aggregation by dilated convolutions. *ICLR*, 2016.
- [68] Liang-Chieh Chen, George Papandreou, Iasonas Kokkinos, Kevin Murphy, and Alan L Yuille. Deeplab: Semantic image segmentation with deep convolutional nets, atrous convolution, and fully connected CRFs. *arXiv:1606.00915*, 2016.
- [69] M. Holschneider, R. Kronland-Martinet, J. Morlet, and Ph. Tchamitchian. A real-time algorithm for signal analysis with the help of the wavelet transform. In Jean-Michel Combes, Alexander Grossmann, and Philippe Tchamitchian, editors, *Wavelets*, pages 286–297, Berlin, Heidelberg, 1990. Springer Berlin Heidelberg.
- [70] Bolei Zhou, Hang Zhao, Xavier Puig, Tete Xiao, Sanja Fidler, Adela Barriuso, and Antonio Torralba. Semantic understanding of scenes through the ade20k dataset. *International Journal on Computer Vision*, 2018.
- [71] Liang-Chieh Chen, George Papandreou, Florian Schroff, and Hartwig Adam. Re-thinking atrous convolution for semantic image segmentation. *arXiv preprint*, abs/1706.05587, 2017.
- [72] Liang-Chieh Chen, Yukun Zhu, George Papandreou, Florian Schroff, and Hartwig Adam. Encoder-decoder with atrous separable convolution for semantic image segmentation. *arXiv preprint*, abs/1802.02611, 2018.
- [73] Di Lin, Yuanfeng Ji, Dani Lischinski, Daniel Cohen-Or, and Hui Huang. Multi-scale context intertwining for semantic segmentation. In *The European Conference on Computer Vision (ECCV)*, September 2018.

- [74] M. Cordts, M. Omran, S. Ramos, T. Rehfeld, M. Enzweiler, R. Benenson, U. Franke, S. Roth, and B. Schiele. The cityscapes dataset for semantic urban scene understanding. In *2016 IEEE Conference on Computer Vision and Pattern Recognition (CVPR)*, pages 3213–3223, June 2016.
- [75] Ansheng You and Yunhai Tong. Torchcv: A pytorch-based framework for deep learning in computer vision. , 2019.
- [76] H. Shin, H. R. Roth, M. Gao, L. Lu, Z. Xu, I. Nogues, J. Yao, D. Mollura, and R. M. Summers. Deep convolutional neural networks for computer-aided detection: Cnn architectures, dataset characteristics and transfer learning. *IEEE Transactions on Medical Imaging*, 35(5):1285–1298, May 2016.
- [77] Holger R. Roth, Le Lu, Amal Farag, Hoo-Chang Shin, Jiamin Liu, Evrim B. Turkbey, and Ronald M. Summers. Deeporgan: Multi-level deep convolutional networks for automated pancreas segmentation. In Nassir Navab, Joachim Hornegger, William M. Wells, and Alejandro Frangi, editors, *Medical Image Computing and Computer-Assisted Intervention – MICCAI 2015*, pages 556–564, Cham, 2015. Springer International Publishing.
- [78] Amal Farag, Le Lu, Holger R. Roth, Jiamin Liu, Evrim Turkbey, and Ronald M. Summers. A bottom-up approach for pancreas segmentation using cascaded superpixels and (deep) image patch labeling. *Trans. Img. Proc.*, 26(1):386–399, January 2017. ISSN 1057-7149. doi: 10.1109/TIP.2016.2624198. URL .
- [79] Nicholas Kolkin, Eli Shechtman, and Gregory Shakhnarovich. Training deep networks to be spatially sensitive. In *The IEEE International Conference on Computer Vision (ICCV)*, Oct 2017.
- [80] W. Shimoda and K. Yanai. Weakly-supervised segmentation by combining cnn feature

- maps and object saliency maps. In *2016 23rd International Conference on Pattern Recognition (ICPR)*, pages 1935–1940, Dec 2016.
- [81] Gustav Larsson, Michael Maire, and Gregory Shakhnarovich. Learning representations for automatic colorization. *ECCV*, 2016.
- [82] T. M. H. C. Santana, K. Nogueira, A. M. C. Machado, and J. A. dos Santos. Deep contextual description of superpixels for aerial urban scenes classification. In *2017 IEEE International Geoscience and Remote Sensing Symposium (IGARSS)*, pages 3027–3031, July 2017.
- [83] A. M. El Amin, Q. Liu, and Y. Wang. Zoom out cnns features for optical remote sensing change detection. In *2017 2nd International Conference on Image, Vision and Computing (ICIVC)*, pages 812–817, June 2017.
- [84] Bolei Zhou, Agata Lapedriza, Jianxiong Xiao, Antonio Torralba, and Aude Oliva. Learning deep features for scene recognition using places database. In *NIPS*, 2014.
- [85] Mark Everingham, SM Ali Eslami, Luc Van Gool, Christopher KI Williams, John Winn, and Andrew Zisserman. The pascal visual object classes challenge: A retrospective. *IJCV*, 111(1), 2015.
- [86] Tsung-Yi Lin, Michael Maire, Serge Belongie, James Hays, Pietro Perona, Deva Ramanan, Piotr Dollár, and C Lawrence Zitnick. Microsoft coco: Common objects in context. In *ECCV*, 2014.
- [87] Bolei Zhou, Aditya Khosla, Agata Lapedriza, Aude Oliva, and Antonio Torralba. Object detectors emerge in deep scene cnns. In *ICLR*, 2015.
- [88] Maxime Oquab, Léon Bottou, Ivan Laptev, and Josef Sivic. Is object localization for free?-weakly-supervised learning with convolutional neural networks. In *CVPR*, 2015.

- [89] Olga Russakovsky, Amy L Bearman, Vittorio Ferrari, and Fei-Fei Li. What's the point: Semantic segmentation with point supervision. *arXiv:1506.02106*, 2015.
- [90] B. Hariharan, P. Aberláz an R. Girshick, and J. Malik. Hypercolumns for object segmentation and fine-grained localization. In *CVPR*, 2015.
- [91] M. Mostajabi, P. Yadollahpour, and G. Shakhnarovich. Feedforward semantic segmentation with zoom-out features. In *CVPR*, 2015.
- [92] George Papandreou, Liang-Chieh Chen, Kevin P Murphy, and Alan L Yuille. Weakly- and semi-supervised learning of a deep convolutional network for semantic image segmentation. In *ICCV*, 2015.
- [93] Jifeng Dai, Kaiming He, and Jian Sun. Boxsup: Exploiting bounding boxes to supervise convolutional networks for semantic segmentation. In *ICCV*, 2015.
- [94] Anna Khoreva, Rodrigo Benenson, Jan Hosang, Matthias Hein, and Bernt Schiele. Weakly supervised semantic labelling and instance segmentation. *arXiv:1603.07485*, 2016.
- [95] Deepak Pathak, Philipp Krahenbuhl, and Trevor Darrell. Constrained convolutional neural networks for weakly supervised segmentation. In *CVPR*, 2015.
- [96] Alessandro Bergamo, Loris Bazzani, Dragomir Anguelov, and Lorenzo Torresani. Self-taught object localization with deep networks. *arXiv:1409.3964*, 2014.
- [97] Ramazan Gokberk Cinbis, Jakob Verbeek, and Cordelia Schmid. Weakly supervised object localization with multi-fold multiple instance learning. *arXiv:1503.00949*, 2015.
- [98] Jia Xu, Alexander G. Schwing, and Raquel Urtasun. Learning to segment under various forms of weak supervision. In *CVPR*, 2015.

- [99] Deepak Pathak, Evan Shelhamer, Jonathan Long, and Trevor Darrell. Fully convolutional multi-class multiple instance learning. In *ICLR workshop*, 2015.
- [100] Pedro O Pinheiro and Ronan Collobert. From image-level to pixel-level labeling with convolutional networks. In *CVPR*, 2015.
- [101] Hyo-Eun Kim and Sangheum Hwang. Deconvolutional feature stacking for weakly-supervised semantic segmentation. *arXiv:1602.04984*, 2016.
- [102] Alexander Kolesnikov and Christoph H Lampert. Seed, expand and constrain: Three principles for weakly-supervised image segmentation. *arXiv:1603.06098*, 2016.
- [103] Dhruv Batra, Payman Yadollahpour, Abner Guzman-Rivera, and Greg Shakhnarovich. Diverse M-Best Solutions in Markov Random Fields. In *ECCV*, 2012.
- [104] Yunchao Wei, Xiaodan Liang, Yunpeng Chen, Xiaohui Shen, Ming-Ming Cheng, Yao Zhao, and Shuicheng Yan. Stc: A simple to complex framework for weakly-supervised semantic segmentation. *arXiv:1509.03150*, 2015.
- [105] Diederik Kingma and Jimmy Ba. Adam: A method for stochastic optimization. In *ICLR*, 2015.
- [106] Liang-Chieh Chen, George Papandreou, Iasonas Kokkinos, Kevin Murphy, and Alan L. Yuille. Semantic image segmentation with deep convolutional nets and fully connected CRFs. In *ICLR*, 2015.
- [107] Zifeng Wu, Chunhua Shen, and Anton van den Hengel. High-performance semantic segmentation using very deep fully convolutional networks. *arXiv:1604.04339*, 2016.
- [108] Deepak Pathak, Philipp Krähenbühl, Jeff Donahue, Trevor Darrell, and Alexei Efros. Context encoders: Feature learning by inpainting. *CVPR*, 2016.

- [109] Mehdi Noroozi and Paolo Favaro. Unsupervised learning of visual representations by solving jigsaw puzzles. *ECCV*, 2016.
- [110] Richard Zhang, Phillip Isola, and Alexei A Efros. Colorful image colorization. *ECCV*, 2016.
- [111] Gustav Larsson, Michael Maire, and Gregory Shakhnarovich. Colorization as a proxy task for visual understanding. *CVPR*, 2017.
- [112] Richard Zhang, Phillip Isola, and Alexei A Efros. Split-brain autoencoders: Unsupervised learning by cross-channel prediction. *CVPR*, 2017.
- [113] Jeff Donahue, Philipp Krähenbühl, and Trevor Darrell. Adversarial feature learning. *ICLR*, 2017.
- [114] Karen Simonyan and Andrew Zisserman. Very deep convolutional networks for large-scale image recognition. *ICLR*, 2015.
- [115] Jeff Donahue, Yangqing Jia, Oriol Vinyals, Judy Hoffman, Ning Zhang, Eric Tzeng, and Trevor Darrell. DeCAF: A deep convolutional activation feature for generic visual recognition. *ICML*, 2014.
- [116] Ian Goodfellow, Jean Pouget-Abadie, Mehdi Mirza, Bing Xu, David Warde-Farley, Sherjil Ozair, Aaron Courville, and Yoshua Bengio. Generative adversarial nets. *NIPS*, 2014.
- [117] Hossein Mobahi, Ronan Collobert, and Jason Weston. Deep learning from temporal coherence in video. *ICML*, 2009.
- [118] Dinesh Jayaraman and Kristen Grauman. Slow and steady feature analysis: Higher order temporal coherence in video. *CVPR*, 2016.

- [119] Phillip Isola, Daniel Zoran, Dilip Krishnan, and Edward H Adelson. Learning visual groups from co-occurrences in space and time. *ICLR, workshop paper*, 2016.
- [120] Ishan Misra, C Lawrence Zitnick, and Martial Hebert. Unsupervised learning using sequential verification for action recognition. *ECCV*, 2016.
- [121] Xiaolong Wang and Abhinav Gupta. Unsupervised learning of visual representations using videos. *ICCV*, 2015.
- [122] Nitish Srivastava, Elman Mansimov, and Ruslan Salakhutdinov. Unsupervised learning of video representations using LSTMs. *ICML*, 2015.
- [123] Deepak Pathak, Ross Girshick, Piotr Dollár, Trevor Darrell, and Bharath Hariharan. Learning features by watching objects move. *CVPR*, 2017.
- [124] Andrew Owens, Jiajun Wu, Josh H. McDermott, William T. Freeman, and Antonio Torralba. Ambient sound provides supervision for visual learning. *ECCV*, 2016.
- [125] Pulkit Agrawal, Ashvin Nair, Pieter Abbeel, Jitendra Malik, and Sergey Levine. Learning to poke by poking: Experiential learning of intuitive physics. *NIPS*, 2016.
- [126] Ashvin Nair, Dian Chen, Pulkit Agrawal, Phillip Isola, Pieter Abbeel, Jitendra Malik, and Sergey Levine. Combining self-supervised learning and imitation for vision-based rope manipulation. *ICRA*, 2017.
- [127] Yuting Zhang, Kibok Lee, and Honglak Lee. Augmenting supervised neural networks with unsupervised objectives for large-scale image classification. *ICML*, 2016.
- [128] Saining Xie, Xun Huang, and Zhuowen Tu. Top-down learning for structured labeling with convolutional pseudoprior. *ECCV*, 2016.
- [129] Antonio Torralba. Contextual priming for object detection. *IJCV*, 2003.

- [130] Chaitanya Desai, Deva Ramanan, and Charless Fowlkes. Discriminative models for multi-class object layout. *IJCV*, 2011.
- [131] Erik B. Sudderth, Antonio Torralba, William T. Freeman, and Alan S. Willsky. Learning hierarchical models of scenes, objects, and parts. *ICCV*, 2005.
- [132] Lubomir Bourdev and Jitendra Malik. Poselets: Body part detectors trained using 3d human pose annotations. *ICCV*, 2009.
- [133] Lubomir Bourdev, Subhransu Maji, Thomas Brox, and Jitendra Malik. Detecting people using mutually consistent poselet activations. *ECCV*, 2010.
- [134] Alex Krizhevsky, Ilya Sutskever, and Geoffrey E. Hinton. ImageNet classification with deep convolutional neural networks. *NIPS*, 2012.
- [135] Olaf Ronneberger, Philipp Fischer, and Thomas Brox. U-Net: Convolutional networks for biomedical image segmentation. *MICCAI*, 2015.
- [136] Vijay Badrinarayanan, Alex Kendall, and Roberto Cipolla. SegNet: A deep convolutional encoder-decoder architecture for image segmentation. *PAMI*, 2017.
- [137] Mohammadreza Mostajabi, Payman Yadollahpour, and Gregory Shakhnarovich. Feed-forward semantic segmentation with zoom-out features. *CVPR*, 2015.
- [138] Tsung-Wei Ke, Michael Maire, and Stella X. Yu. Multigrid neural architectures. *CVPR*, 2017.
- [139] Nathan Silberman, Derek Hoiem, Pushmeet Kohli, and Rob Fergus. Indoor segmentation and support inference from rgb-d images. In *Proceedings of the 12th European Conference on Computer Vision - Volume Part V*, ECCV'12, pages 746–760, Berlin, Heidelberg, 2012. ISBN 978-3-642-33714-7.

- [140] Peng Wang, Xiaohui Shen, Zhe Lin, S. Cohen, B. Price, and A. Yuille. Towards unified depth and semantic prediction from a single image. In *2015 IEEE Conference on Computer Vision and Pattern Recognition (CVPR)*, pages 2800–2809, June 2015.
- [141] Jianbo Jiao, Ying Cao, Yibing Song, and Rynson Lau. Look deeper into depth: Monocular depth estimation with semantic booster and attention-driven loss. In *The European Conference on Computer Vision (ECCV)*, September 2018.
- [142] Arsalan Mousavian, Hamed Pirsiavash, and Jana Kosecka. Joint semantic segmentation and depth estimation with deep convolutional networks. In *3DV*, 2016.
- [143] Xiao Lin, Dalila Sánchez-Escobedo, Josep R. Casas, and Montse Pardàs. Depth estimation and semantic segmentation from a single rgb image using a hybrid convolutional neural network. *Sensors*, 19(8), 2019. ISSN 1424-8220.
- [144] Amir R. Zamir, Alexander Sax, William Shen, Leonidas J. Guibas, Jitendra Malik, and Silvio Savarese. Taskonomy: Disentangling task transfer learning. In *The IEEE Conference on Computer Vision and Pattern Recognition (CVPR)*, June 2018.